

AD-A137 052

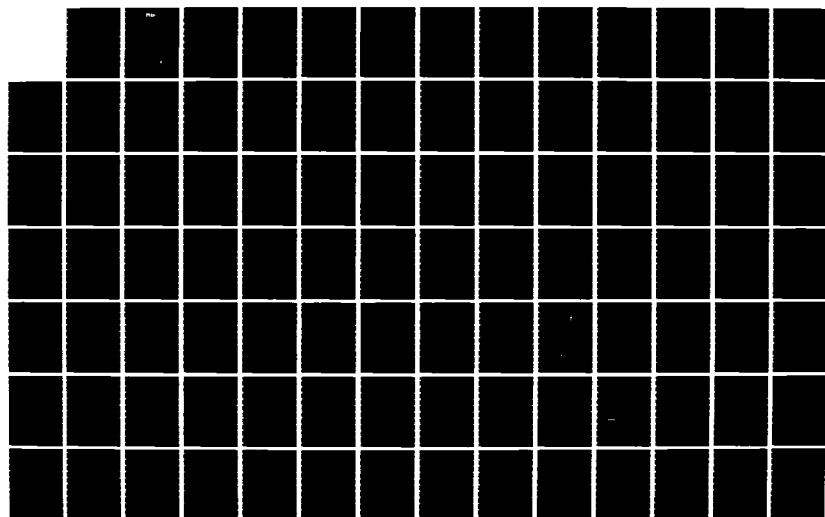
ANALYSIS OF TRANSONIC SHOCK INDUCED SEPARATED FLOW
INCLUDING NORMAL PRESS. (U) UNITED TECHNOLOGIES
RESEARCH CENTER EAST HARTFORD CT J E CARTER ET AL.

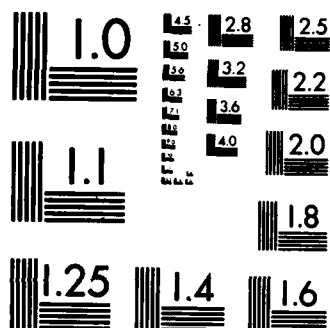
1/2

UNCLASSIFIED

OCT 83 UTRC/R83-915712-2 AFOSR-TR-83-1283 F/G 20/4

NL





MICROCOPY RESOLUTION TEST CHART
NATIONAL BUREAU OF STANDARDS-1963-A

AFOSR-TR- 83 - 1283



**UNITED
TECHNOLOGIES
RESEARCH
CENTER**

East Hartford, Connecticut 06108

AD A 137052

ANALYSIS OF TRANSONIC SHOCK INDUCED SEPARATED FLOW INCLUDING NORMAL PRESSURE GRADIENTS

J.E. Carter, D.E. Edwards, and M.M. Hafez

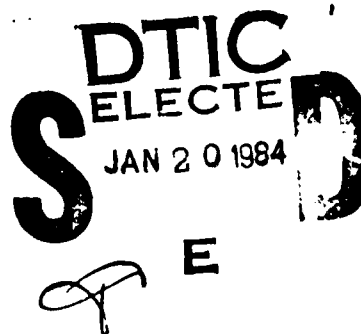
Final Report

Prepared Under Contract F49620-81-C-0041

for the

Air Force Office of Scientific Research
Bolling Air Force Base
Washington, DC 20332

October 1983



Approved for public release;

84 01 19 000
Distribution unlimited.

DTIC FILE COPY

UNCLASSIFIED

SECURITY CLASSIFICATION OF THIS PAGE (When Data Entered)

REPORT DOCUMENTATION PAGE		READ INSTRUCTIONS BEFORE COMPLETING FORM
1. REPORT NUMBER AFOSR-TR- 33 - 1288	2. GOVT ACCESSION NO. AD-A137052	3. RECIPIENT'S CATALOG NUMBER
4. TITLE (and Subtitle) Analysis of Transonic Shock Induced Separated Flow Including Normal Pressure Gradients		5. TYPE OF REPORT & PERIOD COVERED Final Report April 1982-31 August 1983
7. AUTHOR(s) J. E. Carter, D. E. Edwards, M. M. Hafez		6. PERFORMING ORG. REPORT NUMBER R83-915712-2
9. PERFORMING ORGANIZATION NAME AND ADDRESS United Technologies Research Center Silver Lane East Hartford, CT 06108		8. CONTRACT OR GRANT NUMBER(s) F49620-81-C-0041
11. CONTROLLING OFFICE NAME AND ADDRESS AFOSR/NA Bolling Air Force Base Washington, D.C. 20332		10. PROGRAM ELEMENT, PROJECT, TASK AREA & WORK UNIT NUMBERS 61102F 2307/A1
14. MONITORING AGENCY NAME & ADDRESS (if different from Controlling Office)		12. REPORT DATE October 1983
		13. NUMBER OF PAGES 105
		15. SECURITY CLASS. (of this report) Unclassified
		15a. DECLASSIFICATION/DOWNGRADING SCHEDULE
16. DISTRIBUTION STATEMENT (of this Report) Approved for public release; Distribution unlimited.		
17. DISTRIBUTION STATEMENT (of the abstract entered in Block 20, if different from Report)		
18. SUPPLEMENTARY NOTES		
19. KEY WORDS (Continue on reverse side if necessary and identify by block number) Transonic flow, shock-wave boundary-layer interaction, separated turbulent flow, inviscid rotational flow theory, viscous-inviscid interaction		
20. ABSTRACT (Continue on reverse side if necessary and identify by block number) An analysis based on a two-layer interaction model is presented for the prediction of transonic shock-wave, boundary-layer interaction with emphasis on turbulent separated flow. In this analysis finite difference techniques are used to solve the viscous layer equations, expressed in a defect form, and the stream function-vorticity representation of the inviscid flow. A global		

DD FORM 1 JAN 73 1473

EDITION OF 1 NOV 68 IS OBSOLETE
S/N 0102-014-6601

UNCLASSIFIED

SECURITY CLASSIFICATION OF THIS PAGE (When Data Entered)

~~UNCLASSIFIED~~

SECURITY CLASSIFICATION OF THIS PAGE (When Data Entered)

(Mach no. 1.4)
technique is used to iteratively solve these coupled sets of equations. Normal pressure gradients and imbedded shock effects are included in the analysis. There are two major conclusions which can be drawn from the present work: First, favorable comparisons which have been obtained with the separated data of Kooi ($M_\infty = 1.4$) demonstrate that the present analysis is capable of accurately resolving many of the details of transonic shock-wave, boundary-layer interaction. Second, these results show that, for transonic shock induced separation, the effect of displacement thickness interaction dominates over that produced by imbedded shock effects and normal pressure gradients. Calculations made with a modified algebraic turbulence model demonstrate that for separated cases the computed results are more sensitive to the turbulence model than to whether or not normal pressure gradients are included. Additional results are also presented for transonic shock-wave, boundary-layer interaction using the stream function-vorticity inviscid technique to implement the concepts of rotational inviscid flow theory for the representation of transonic interactions. Finally, a new three-layer interaction model is presented with computed results shown for low speed separated flow interactions.

~~UNCLASSIFIED~~

SECURITY CLASSIFICATION OF THIS PAGE (When Data Entered)

Analysis of Transonic Shock Induced Separated
Flow Including Normal Pressure Gradients

TABLE OF CONTENTS

	<u>Page</u>
SUMMARY	1
INTRODUCTION	2
SYMBOLS	6
VISCOUS-INVISCID INTERACTION FLOW MODEL	9
Inviscid Analysis	10
Governing Equations and Boundary Conditions	10
Numerical Technique	12
Viscous Layer Analysis	14
Governing Equations and Boundary Conditions	14
Transformed Viscous Formulation	18
Equivalent Inviscid Flow	22
Viscous-Inviscid Interaction Procedure	24
Inviscid Surface Boundary Condition	24
Global Iteration Technique	25
RESULTS AND DISCUSSION	27
Attached Flow Calculations	27
Inviscid Rotational Flow Analysis	27
Interacting Boundary Layer Theory	30
Separated Flow Calculations	31
Free Air Results	31
Inviscid Rotational Flow Analysis	32
Channel Results for IBLT with Normal Pressure Gradients	33
Comparison of IBLT With and Without Normal Pressure Gradients	38
CONCLUDING REMARKS	39
ACKNOWLEDGEMENTS	41
REFERENCES	42
FIGURES	45
APPENDIX A	A-1

AIR FORCE OFFICE OF SCIENTIFIC RESEARCH
NOTICE OF TRANSMITTAL TO DTIC
This technical report has been approved for public release and distribution is unlimited.
MATTHEW J. KEMPNER
Chief, Technical Information Division

SUMMARY

An analysis based on a two-layer interaction model is presented for the prediction of transonic shock-wave, boundary-layer interaction with emphasis on turbulent separated flow. In this analysis finite difference techniques are used to solve the viscous layer equations, expressed in a defect form, and the stream function-vorticity representation of the inviscid flow. A global technique is used to iteratively solve these coupled sets of equations. Normal pressure gradients and imbedded shock effects are included in this analysis. There are two major conclusions which can be drawn from the present work. First, favorable comparisons which have been obtained with the separated data of Kooi ($M_\infty = 1.4$) demonstrate that the present analysis is capable of accurately resolving many of the details of transonic shock-wave, boundary-layer interaction. Second, these results show that for transonic shock induced separation the effect of displacement thickness interaction dominates over that produced by imbedded shock effects and normal pressure gradients. Calculations made with a modified algebraic turbulence model demonstrate that for separated cases the computed results are more sensitive to the turbulence model than to whether or not normal pressure gradients are included. Additional results are also presented for transonic shock-wave, boundary-layer interaction using the stream function-vorticity inviscid technique to implement the concepts of rotational inviscid flow theory for the representation of transonic interactions. Finally, a new three-layer interaction model is presented with computed results shown for low speed separated flow interactions.

Accession For	
NTIS GRA&I	<input checked="" type="checkbox"/>
DTIC TAB	<input type="checkbox"/>
Unannounced	<input type="checkbox"/>
Justification	
By	
Distribution/	
Availability Codes	
Dist	Avail and/or Special
A-1	



INTRODUCTION

The prediction of the flow field in transonic shock-wave, boundary-layer interaction is an aerodynamic problem of immense practical importance in both external aerodynamics and turbomachinery applications since this flow phenomena has a large influence on the overall aerodynamic forces and often determines the upper limit in performance of each aerodynamic component. Examples of such components include airfoils in supercritical flow-both external and internal (turbomachinery applications), exhaust nozzles, and engine inlets. These interactions can lead to premature separation which can result in buffeting, large increases in drag, and reduced engine performance. In addition, it is difficult to predict full scale shock interaction phenomena from small scale wind tunnel data because of the current inability to match experimentally full scale Reynolds number flows. Hence, there is a strong need to develop analytical and computational techniques for the analysis of the problem of transonic shock wave boundary-layer interaction.

The intersection of a shock wave with a turbulent boundary layer in transonic flow results in a complex flow pattern. Figure 1 shows a schematic diagram of the flow structure which occurs for both attached and separated flow. In both cases, disturbances created by the impingement of the shock wave on the boundary layer propagate upstream in the subsonic portion of the boundary layer. This increase in thickness creates compression waves which intersect with the shock wave and cause it to bend forward. The increase in the pressure at the wall is a steep, but continuous distribution since it lies below the sonic line. Away from the wall discontinuities may occur in the viscous layer if the shock penetrates this region. If the upstream Mach number is not too high the flow remains attached with the flow pattern shown on the left side of Fig. 1. However, an increase in upstream Mach number to a value of 1.3 or greater will result in flow separation with a more complex pattern as shown on the right side of Fig. 1. Generally flow separation results in a bifurcation of the shock wave into a front and rear leg near the wall with a vortex sheet emanating from the triple point. A separation bubble of slow recirculating flow occurs at the foot of the shock wave in the lower portion of the viscous layer. In both the attached and separated flow cases the upstream influence of the shock wave is typically about 5 undisturbed boundary-layer thicknesses; the downstream extent of the interaction depends on the shock strength. The short streamwise length scale of the interaction region results in a rapid turning of the flow which is generally thought to induce large normal pressure gradients in the viscous layer. The overall objective in the present investigation has been to develop a reliable and accurate method for the prediction of the detailed properties of the flow which occur when a transonic normal shock wave, of sufficient strength to cause flow separation, impinges on a turbulent boundary layer. Only the flow in the immediate vicinity of the shock-wave, boundary-layer interaction has been considered since the focus of the present work was to use the analysis developed herein to give a better understanding of the relative importance of imbedded shock effects and normal pressure gradients in transonic shock induced separation. Before the details of this analysis

are given, a brief discussion is presented on previous approaches which have been developed for this problem.

The interaction of a shock wave and a turbulent boundary layer has been the subject of numerous experimental and theoretical investigations in the past forty years. Only a brief review of some of this work will be given here; for a more detailed account of past work the reader is referred to the recent review articles by Adamson and Messiter (Ref. 1), Melnik (Ref. 2), and Lock and Firmin (Ref. 3).

Among the experimental studies is the work of Seddon (Ref. 4), Kooi (Refs. 5 and 6), and the more recent work of Om (Refs. 7 and 8) in which detailed measurements were made of the flow properties in the immediate vicinity of a normal shock wave impinging on a flat plate turbulent boundary layer. In these studies the shock wave was of sufficient strength to separate the turbulent boundary layer. Seddon and Kooi's experiments were conducted in a planar configuration whereas Om's measurements were made in an axisymmetric tunnel to avoid the possible three-dimensional effects which can occur in planar channel experiments. Detailed data were obtained in these experimental studies for the pressure distributions, velocity profiles and associated integral properties, and the structure of the flow field. In all of these flow studies a lambda shock pattern was observed above the locally separated turbulent boundary layer. An important issue in the turbulent shock boundary-layer interaction problem is whether or not the shock wave penetrates the boundary layer, that is, do the compression waves which result when the shock strikes the rotational flow coalesce inside or outside of the viscous layer? In the experimental studies of Kooi on transonic shock wave boundary-layer interaction, it was observed that at a free stream Mach number of 1.40 compression wave coalescence occurs well outside the boundary layer to form the forward leg of the oblique shock. At a higher Mach number of 1.54 East (Ref. 9) observed that the "oblique shock was formed at the edge or probably even inside the boundary layer". Clearly the development of a theoretical method which allows for imbedded shock effects and normal pressure gradients would increase the current ability to quantitatively predict the influence of Mach and Reynolds number on transonic interactions.

Theoretical approaches to the problem of transonic shock-wave, boundary-layer interaction range from numerical solutions of the Reynolds averaged Navier-Stokes equations to the use of asymptotic methods which attempt to delineate the detailed mathematical structure of the flow field. Examples of the former approach are the computations made by Viegas and Horstman (Ref. 10) and Shea (Ref. 11). This work as well as similar efforts of others has shown that this approach can predict the general features of the interaction region but to date a preferred technique has failed to emerge from these numerical studies. Part of the difficulty is that with a full numerical approach the grid must be carefully chosen in order to capture the flow phenomena which occurs at different length scales in the interaction problem. It is well recognized that if the Reynolds number is sufficiently high, as it generally is for most aerodynamic problems of interest, the flow field can be divided into viscous and inviscid regions even if flow separation is present. Analytical approaches

which split the flow field into several regions will clearly provide the best overall resolution provided that the proper formulation and matching conditions can be established for each of these regions. This is the goal of asymptotic methods which are described next for the application to transonic shock-wave, boundary-layer interaction.

In recent years large Reynolds number asymptotic expansions have been used to develop local solutions for weak shock waves interacting with turbulent boundary layers. Among these efforts is the work of Melnik and Grossman (Ref. 12), Adamson and Feo (Ref. 13), and Messiter (Ref. 14) in which they have shown that, in the absence of flow separation, the interaction of a normal shock wave with a turbulent boundary layer can be represented by the interaction between the outer part of the turbulent boundary layer, treated as an inviscid rotational flow, and the incident shock wave. For weak shock waves, they have concluded that the thin viscous sublayer near the wall plays a passive role in the overall interaction process. These asymptotic theories have evolved from the pioneering work of Lighthill (Ref. 15); Melnik (Ref. 2) provides an excellent discussion of the ensuing work between Lighthill's paper and the present-day work in asymptotic analysis of transonic interactions.

Melnik and Grossman (Ref. 12) obtained numerical solutions to the inviscid nonlinear governing equations which resulted from their asymptotic analysis. Their solutions demonstrate that the mechanism which causes the shock to bend forward and blend smoothly into the sonic line is contained entirely in the interaction between the inviscid rotational flow and externally imposed shock wave. Later Melnik and Grossman (Ref. 16) showed favorable comparison with the wall pressure determined experimentally by Gadd (Ref. 17) which demonstrated the accuracy of their asymptotic method for describing the flow in a case where flow separation does not occur. If flow separation does occur, which is the subject of the present report, further work is needed in the development of asymptotic methods in order to provide a rational theory for shock induced turbulent separated flow.

The approach taken in the present investigation is an outgrowth of interacting boundary layer theory (IBLT) which is now briefly reviewed. In recent years significant progress has been made in the development of methods for the iterative solution of the viscous and inviscid equations through displacement thickness coupling. In the initial development period of IBLT, work was principally focused on establishing inverse boundary layer methods, beginning with the work of Catherall and Mangler (Ref. 18) to eliminate the classical singularity that occurs at the separation point when the boundary-layer equations are solved subject to a prescribed pressure distribution. Numerous inverse boundary-layer methods, discussed in Appendix A, have been developed since this earlier work. Following this period, work was directed toward the development of procedures which permit inverse boundary-layer and inviscid solution techniques to be iteratively linked together. Two methods which have received wide use are the semi-inverse schemes of LeBalleur (Ref. 19) and Carter (Ref. 20). These schemes have been successfully used in a number of applications of IBLT for the prediction of laminar, transitional, and turbulent separated flow.

Current efforts in the development of IBLT began several years ago with the work of LeBalleur (Ref. 21) in which he described a generalized viscous layer approach where the governing equations are expressed as the difference (or defect) between the viscous and inviscid flow equations. This treatment permits the inclusion of normal pressure gradients and embedded shock effects in the solution of shock-wave, boundary-layer interactions. LeBalleur (Ref. 21), East (Ref. 22), and Lock and Firmin (Ref. 3) have utilized these concepts to develop generalized integral boundary layer approaches which include these effects.

The present work is based on a viscous-inviscid interaction flow model which is described in detail in the next section of this report. This model principally consists of a differential treatment of the defect formulation laid out by LeBalleur (Ref. 21) utilizing a generalization of the inverse boundary-layer method of Carter (Ref. 23) coupled to the stream function-vorticity inviscid method of Hafez and Lovell (Ref. 24). Application of this generalized IBLT formulation to several problems of transonic shock-wave, boundary-layer interaction are presented in the section on Results and Discussion. The experimental data of Kooi (Ref. 5) is used to evaluate this approach. Numerous conclusions are drawn from the present study; the principal one is that displacement thickness coupling is the dominant effect which must be included in the prediction of separated transonic shock-wave, boundary-layer interaction.

SYMBOLS

c_v	Coefficient of specific heat at constant volume
\tilde{f}	Viscous perturbation stream function
F	Velocity ratio
g	Total enthalpy ratio
h	Displacement thickness divided by boundary layer thickness
H	Total enthalpy
$\bar{\kappa}$	Approximate viscous layer streamline curvature
m	Perturbation mass flow
M	Mach number
p	Static pressure
Δp	Difference between pressure in real viscous flow and equivalent inviscid flow
p_t	Total pressure
Pr	Prandtl number
Re	Reynolds number
R	Gas constant
s	Entropy
T	Static temperature
\bar{T}	Static temperature ratio
u	Velocity component in x-direction
v	Velocity component in y-direction
x	Coordinate measured along flat plate
y	Coordinate measured perpendicular to flat plate
β	Inviscid velocity gradient parameter
γ	Ratio of coefficients of specific heat

ρ	Density
$\bar{\rho}$	Density ratio
ψ	Stream function
ψ_{Δ}	Inviscid perturbation stream function
ω	Vorticity
$\bar{\omega}$	Relaxation factor in global iteration scheme
μ	Molecular viscosity coefficient
ϵ	Eddy viscosity coefficient
δ	Boundary layer thickness
θ	Momentum thickness
δ^*	Displacement thickness
ξ	Transformed x-coordinate
η	y-Coordinate divided by δ^*
$\hat{\eta}$	y-Coordinate divided by δ

Subscripts

∞	Free stream conditions
o	Conditions at upstream boundary
ir	Inviscid quantity at reference surface
δ^*	Inviscid quantity at the displacement surface
w	Inviscid quantity at the wall
i	Quantity in equivalent inviscid flow
e	Edge of boundary layer
I	Inviscid prediction in global iteration technique
V	Viscous prediction in global iteration technique
inc	Incompressible

Superscripts

- * Dimensional quantity
- i Global iteration counter

VISCOUS-INVISCID INTERACTION FLOW MODEL

In contrast with the asymptotic theory developed by Melnik and Grossman (Ref. 12) and others for shock-wave, turbulent boundary-layer interaction for attached transonic flow, a rational theory has yet to be developed for the strong interaction case in which the shock wave is of sufficient strength to separate the boundary layer. In the absence of such a formal theory, the present study has been directed toward the development of two viscous-inviscid interaction flow models for strongly interacting flows with separation. These models are considered reasonable since their construction is a natural outgrowth of the knowledge which does exist on the multiple layer structure of laminar and turbulent interacting flows.

These models are shown schematically in Fig. 2. In both models the Reynolds number is assumed to be large and therefore the viscous effects are confined to a relatively thin layer near the surface. The main difference in these two models is the treatment of the viscous layer. In the two-layer model the boundary-layer equations, including an approximate treatment of normal pressure gradients, are solved across the entire viscous layer; exterior to this region the inviscid equations are solved. In this model the inviscid flow may be rotational due to an upstream nonuniformity or the vorticity produced by a curved shock. Matching conditions are imposed which result in a smooth merging of the viscous and inviscid layers. In the absence of normal pressure gradients this model reduces to that of classical displacement thickness interaction. The three layer model consists of an outer inviscid region, which is coupled to a rotational inviscid layer to represent the outer portion of the upstream turbulent profile, and a viscous sublayer near the wall to accommodate the imposition of the no slip conditions. In this model, as in the two-layer model, rotational effects may occur in the outer inviscid region; however in this model there is an additional thin vortical layer near the surface whose thickness is of the order of the upstream boundary-layer thickness. In the Melnik-Grossman (Ref. 12) asymptotic analysis for attached flows the viscous sublayer plays a passive role in the overall interaction process and thus does not have to be computed unless the skin friction distribution is desired. For separated flows, this viscous sublayer plays an active role and therefore its effect must be included in order to properly displace the outer vortical layer.

The bulk of this report is directed toward the development and verification, through experimental comparisons, of the two-layer model. The three-layer model is presented in Appendix A along with computed examples for incompressible separated flow which demonstrate this method. In both of these models the inviscid flow has to be capable of treating rotational flow due to an upstream nonuniformity, curved shock wave, or the vorticity contained in the outer portion of an upstream turbulent boundary layer. In the next section of this report an inviscid analysis based on the stream function-vorticity approach, is presented for the computation of rotational transonic flow. Next the viscous region analysis, used in the two-layer model, is presented followed by a discussion of the viscous-inviscid

interaction procedure which is used to couple the inviscid and viscous flow analyses.

Inviscid Analysis

The governing equations, boundary conditions, and numerical technique of the inviscid analysis used in the present study on transonic shock wave boundary layer interaction are described here. This method is based on the compressible stream function method of Hafez and Lovell (Ref. 24) which they have developed for the analysis of transonic inviscid flow. Prior to their work difficulties had been encountered in the use of the stream function approach in the transonic speed range since the density is a double valued function of the mass flux (there is a subsonic and supersonic branch). Hafez and Lovell presented a method which overcomes this difficulty thereby allowing solutions to the stream function equation to be obtained for transonic flows. This approach has a major advantage over that based on the potential flow approximation since it is equivalent to a solution of the Euler equations provided the entropy and vorticity produced by a curved shock or an upstream nonuniformity are taken into account. A second advantage of the stream function approach is that, in conservation form, it closely resembles the form of the full potential equation for which numerous computational techniques have been developed during the past ten years.

Governing Equations and Boundary Conditions

Since the present work is focused on the problem of a two-dimensional normal shock wave impinging on a flat plate turbulent boundary layer, the presentation of the inviscid equations will be made in terms of the Cartesian coordinates x and y , and the respective velocities, u and v . Introduction of a stream function ψ defined by

$$\rho u = \frac{\partial \psi}{\partial y}, \quad \rho v = - \frac{\partial \psi}{\partial x} \quad (1)$$

automatically satisfies the continuity equation

$$\frac{\partial \rho u}{\partial x} + \frac{\partial \rho v}{\partial y} = 0 \quad (2)$$

A second-order equation is determined for the stream function by the substitution of Eq. (1) into the definition of vorticity ω given by

$$-\omega = \frac{\partial u}{\partial y} - \frac{\partial v}{\partial x} \quad (3)$$

which leads to

$$\frac{\partial}{\partial x} \left(\frac{1}{\rho} \frac{\partial \psi}{\partial x} \right) + \frac{\partial}{\partial y} \left(\frac{1}{\rho} \frac{\partial \psi}{\partial y} \right) = -\omega \quad (4)$$

The inviscid formulation is completed by the definition of the total enthalpy, assumed constant in the present study,

$$H = \frac{\gamma p}{(\gamma-1)\rho} + \frac{u^2 + v^2}{2} = \frac{1}{(\gamma-1)M_\infty^2} + \frac{1}{2} \quad (5)$$

the equation of state written in the form

$$\rho = \frac{1}{\gamma M_\infty^2} \rho^\gamma e^{s/c_v} \quad (6)$$

and the Crocco relation

$$\frac{\omega}{\rho} = \frac{ds/R}{d\psi} \quad (7)$$

Equation (7) shows that the ratio of vorticity to pressure is constant along a streamline since $s = s(\psi)$ only.

The definitions given in Eq. (1) and Eqs. (3)-(7) constitute seven equations for the seven unknowns ψ , ω , s , p , ρ , u , and v . These equations have been expressed in nondimensional form in which the x - and y -coordinates have been nondimensionalized by the incoming boundary-layer thickness, δ_0^* , shown schematically in Fig. 3, the velocities by the free stream value, u_∞^* , the density by ρ_∞^* , and the pressure by $\rho_\infty^* u_\infty^{*2}$ where an asterisk is used here to denote dimensional quantities.

The boundary conditions imposed for the solution of these equations are shown schematically in Fig. 3 for the analysis of a normal shock wave impinging on a flat plate boundary layer. At the upstream boundary all dependent variables are prescribed from the incoming free stream flow with a rotational layer near the wall to represent the outer portion of the turbulent boundary layer. At the outer boundary a normal shock wave is imposed by setting the values of ρ and u from the Rankine-Hugoniot normal shock wave conditions. In the "free air" calculations, with the outer boundary placed sufficiently far from the wall so that the flow is undisturbed at $y = y_{\max}$, the values of ρ , u , and ψ are held constant along this boundary. In calculations which were made to compare the present method with experimental data, it was found necessary to impose conditions along this outer boundary to represent the blockage effect which occurs when a shock-wave, boundary-layer interaction occurs in

a channel. In this case the outer boundary is not a streamline but rather the condition

$$\frac{\partial \psi}{\partial y} = \rho u \quad (8)$$

is imposed where ρu is prescribed from the experimental measurements.

At the wall the presence of the viscous flow is represented in the inviscid analysis as a Dirichlet condition on the stream function, $\psi(x,0) = \psi_w(x)$. The relationship between $\psi_w(x)$ and the viscous solution will be discussed in detail in the section on the Viscous-Inviscid Interaction Procedure. At the downstream or outflow boundary ψ_{xx} is set to zero; calculations were also made with $\psi_x = 0$ at this boundary with only small changes in the results.

Numerical Technique

In this section the numerical technique used to solve the inviscid formulation is presented. This technique closely follows that presented previously by Hafez and Lovell (Ref. 24) for the computation of transonic flow with the stream function-vorticity approach.

Coordinate stretchings, $X = g(x)$ and $Y = f(y)$, have been introduced to place fine grids near the shock wave and the wall to resolve the large gradients which occur in these regions. The transformed stream function-vorticity equation is

$$g' \frac{\partial}{\partial X} \left(\frac{g'}{\tilde{\rho}} \frac{\partial \psi}{\partial X} \right) + f' \frac{\partial}{\partial Y} \left(\frac{f'}{\tilde{\rho}} \frac{\partial \psi}{\partial Y} \right) = -\omega \quad (9)$$

where a prime is used to denote differentiation. Equation (9) is represented with central difference approximations which results in

$$\begin{aligned} & \frac{g'_{m,n}}{\Delta X^2} \left[\left(\frac{g'}{\tilde{\rho}} \right)_{m+\frac{1}{2},n} (\psi_{m+1,n} - \psi_{m,n}) - \left(\frac{g'}{\tilde{\rho}} \right)_{m-\frac{1}{2},n} (\psi_{m,n} - \psi_{m-1,n}) \right] \\ & + \frac{f'_{m,n}}{\Delta Y^2} \left[\left(\frac{f'}{\tilde{\rho}} \right)_{m,n+\frac{1}{2}} (\psi_{m,n+1} - \psi_{m,n}) - \left(\frac{f'}{\tilde{\rho}} \right)_{m,n-\frac{1}{2}} (\psi_{m,n} - \psi_{m,n-1}) \right] \quad (10) \\ & = -\omega_{m,n} \end{aligned}$$

for the computational molecule shown in Fig. 4. With $\tilde{\rho}$ and ω assumed known, Eq. (10) is solved with the zebroid scheme (Ref. 25) which utilizes line relaxation along alternating black and white horizontal lines. A finite difference approximation to a ψ_{xt} term has been explicitly added to this equation to guarantee convergence in the supersonic zone (Ref. 26).

After the stream function is computed the u-component of velocity is deduced by the integration of Eq. (3) from the outer boundary $Y = 1$ where u is prescribed. This results in

$$u(x, Y) = u(x, 1) - \frac{1}{f'} \int_{Y=1}^Y \left(-\omega + g' \frac{\partial v}{\partial x} \right) dY \quad (11)$$

With ω and v assumed known, Eq. (11) is integrated with the trapezoidal rule to yield u at the segment centers denoted by an x in Fig. 4. The v -component of velocity is then calculated at the cell centers, denoted by a $+$ in Fig. 4, with the finite difference representation of

$$v = - \frac{g'(\partial\psi/\partial x)}{f'(\partial\psi/\partial Y)} u \quad (12)$$

In Eq. (12) the value of u at the cell center is obtained by averaging the segment center values.

The density is then updated at the cell centers using a combined form of the total enthalpy and state equations which gives

$$\rho = \left[1 + \frac{\gamma-1}{2} M_x^2 (1 - u^2 - v^2) \right]^{\frac{1}{\gamma-1}} e^{-s/R} \quad (13)$$

The values at the segment centers are computed by averaging the cell center values. It is well known that in order to maintain numerical stability in transonic flow computations it is necessary to add an artificial viscosity term in the supersonic region. In the present calculations the retarded density method of Hafez, et al. (Ref. 26) has been used to add artificial viscosity using a modified density

$$\tilde{\rho} = \rho - \mu \Delta x \frac{\partial \rho}{\partial x} \quad (14)$$

with

$$\mu = \max \left[0, c \left(1 - \frac{1}{M^2} \right) \right] \quad (15)$$

where c is an assigned constant and M is the local Mach number. The term is computed with an upwind finite difference approximation. The use of artificial viscosity in the inviscid analysis causes the shock wave to be spread over several grid points; calculations will be presented in the Results and Discussion section which show that this shock smearing is significantly smaller than that which results due to the real viscous effects.

The steps in this numerical procedure are completed by using the Crocco relation, Eq. (7), to update the vorticity after every 10 sweeps of the inviscid flow equation. In the present calculations the entropy rise at the shock has been neglected; hence the entropy and vorticity distribution is due solely to that specified at the upstream boundary to represent the outer portion of the incoming turbulent boundary layer. Since this distribution is known a priori an analytical curve fit is used to represent $s = s(\psi)$. In the numerical calculations, with the latest values of ψ and ρ assumed known at each grid point, s and $ds/d\psi$ are computed analytically from this curve fit and the value of ω is updated at each point by the substitution of Eq. (6) for the pressure into the Crocco relation, Eq. (7).

Neglect of the entropy rise at the shock wave does not result in a serious error in the present calculation since the Rankine-Hugoniot relations have been used to specify the correct shock jump conditions for ρ and u at the outer computational boundary. Free air calculations at $M_\infty = 1.4$ have shown that the value of the pressure behind the normal shock wave is overpredicted by only about 5 percent. However, as will be discussed in greater detail in the Results and Discussion section, this approximation does prevent the formation of a lambda shock in the calculation which generally occurs when the shock wave is of sufficient strength to separate the boundary layer.

Viscous Analysis

In this section the formulation and solution technique is given for the viscous region, which is contained in the two-layer viscous-inviscid interaction flow model discussed previously. This analysis is an extension of the first-order inverse boundary-layer analysis (Ref. 23) to now include normal pressure gradients and asymptotic merging with the outer inviscid flow at the viscous layer edge.

Governing Equations and Boundary Conditions

The governing equations for the viscous flow analysis are written as follows in terms of Cartesian coordinates and the corresponding velocity components, u and v , as shown in Fig. 5:

$$\frac{\partial \rho u}{\partial x} + \frac{\partial \rho v}{\partial y} = 0 \quad (16)$$

$$\rho u \frac{\partial u}{\partial x} + \rho v \frac{\partial u}{\partial y} = -\frac{\partial p}{\partial x} + \frac{1}{\text{Re}_\infty} \frac{\partial}{\partial y} \left(\mu \frac{\partial u}{\partial y} \right) - \frac{\partial}{\partial y} (\rho u'v') \quad (17)$$

$$\frac{\partial p}{\partial y} = \bar{\kappa} \rho u^2 \quad (18)$$

$$\rho u \frac{\partial H}{\partial x} + \rho v \frac{\partial H}{\partial y} = \frac{1}{Re_\infty} \frac{\partial}{\partial y} \left[\mu \left(1 - \frac{1}{Pr} \right) u \frac{\partial u}{\partial y} + \frac{\mu}{Pr} \frac{\partial H}{\partial y} \right] - \frac{\partial}{\partial y} (\rho \overline{H'v'}) \quad (19)$$

Equations (16), (17) and (19) are the usual continuity equations and boundary-layer forms of the x-momentum and total enthalpy equations, respectively. Equation (18) is an approximate form of the normal momentum equation, suggested by LeBalleur (Ref. 21) and Lock and Firmin (Ref. 3), in which it has been assumed that the viscous terms are negligible and the convection terms can be approximated by $\bar{\kappa} \rho u^2$ where $\bar{\kappa}(x)$ is an average viscous layer curvature.

Additional equations are needed to complete the specification of the viscous layer formulation. The molecular viscosity coefficient is given by the Sutherland relation which for air is written in nondimensional form as

$$\mu = \frac{1 + \frac{198.6^\circ R}{T_\infty^*}}{\frac{T}{T_\infty} + \frac{198.6^\circ R}{T_\infty^*}} \left(\frac{T}{T_\infty} \right)^{3/2} \quad (20)$$

where T_∞^* and T_∞ denote the dimensional (expressed in degrees Rankine) and nondimensional reference temperatures of the free stream, respectively. The equation of state is written as

$$\rho = \frac{\gamma - 1}{\gamma} \rho T \quad (21)$$

where the temperature is deduced from the total enthalpy definition

$$H = T + \frac{u^2 + v^2}{2} \quad (22)$$

Equations (16)–(22) constitute a set of seven equations in the seven unknowns, u , v , p , ρ , μ , H and T , provided that the average curvature is known and that the Reynolds stresses are related to the mean flow through a turbulence model. In this investigation the Reynolds stresses have been related to the mean flow by an eddy viscosity representation given by

$$-\rho \overline{u'v'} = \frac{\epsilon}{Re_\infty} \frac{\partial u}{\partial y} \quad (23)$$

$$-\rho \overline{H'v'} = \frac{\epsilon_H}{Re_\infty} \frac{\partial H}{\partial y} \quad (24)$$

In the present formulation a constant turbulent Prandtl number Pr_t is assumed, which is defined in the same manner as Cebeci and Smith (Ref. 27)

$$Pr_t = \frac{\epsilon}{\epsilon_H} \quad (25)$$

thereby giving

$$-\rho \overline{H'v'} = \frac{\epsilon}{Re_\infty Pr_t} \frac{\partial H}{\partial y} \quad (26)$$

The turbulence models used in the present calculations will be discussed later.

The variables in Eqs. (16)-(26) are expressed in nondimensional form with lengths scaled by the upstream boundary-layer thickness δ_0^* as shown in Fig. 5, velocities by the free stream value, u_∞^* , pressure by twice the free stream dynamic pressure, $\rho_\infty^* u_\infty^{*2}$, temperature by u_∞^{*2}/c_p^* , total enthalpy by u_∞^{*2} , density by ρ_∞^* , and viscosity coefficients (μ and ϵ) by μ_∞^* . An asterisk is used here and in Fig. 5 to denote dimensional quantities. The Reynolds number which appears in Eqs. (17) and (19) is

$$Re_\infty = \frac{\rho_\infty^* u_\infty^* \delta_0^*}{\mu_\infty^*} \quad (27)$$

The equations presented above describe the flow in the viscous layer adjacent to the wall, $y = 0$. As stated previously, it is assumed that the Reynolds number is sufficiently high so that the overall flow field can be divided into a viscous layer near the surface and an inviscid region outside of the viscous layer. Hence, at a sufficiently large distance from the surface, the viscous solution is required to merge smoothly into that for the inviscid flow. Therefore, it is convenient to write the viscous layer equations as the difference between the real viscous flow (RVF) and the equivalent inviscid flow (EIF) where the latter results when the inviscid flow is solved in the interior of the viscous region. LeBalleur (Ref. 21) pioneered this idea of writing the viscous equations in this defect form; Lock and Firmin (Ref. 3) have further explored this idea and introduced the concepts of RVF and EIF mentioned above.

The defect form of the viscous-layer equations used in the present study are written as follows in which the i -subscript is used to denote the variables in the EIF:

$$\frac{\partial(\psi - \psi_i)}{\partial y} = \rho u - \rho_i u_i \quad (28)$$

$$\begin{aligned} \rho u \frac{\partial u}{\partial x} - \rho_i u_i \frac{\partial u_i}{\partial x} - \frac{\partial \psi}{\partial x} \frac{\partial u}{\partial y} + \frac{\partial \psi_i}{\partial x} \frac{\partial u_i}{\partial y} = - \frac{\partial \hat{p}}{\partial x} \\ + \frac{1}{Re_\infty} \left[\frac{\partial}{\partial y} (\mu + \epsilon) \frac{\partial u}{\partial y} \right] \end{aligned} \quad (29)$$

$$\frac{\partial \hat{p}}{\partial y} = \kappa (\rho u^2 - \rho_i u_i^2) \quad (30)$$

$$\begin{aligned} \rho u \frac{\partial H}{\partial x} - \rho_i u_i \frac{\partial H_i}{\partial x} - \frac{\partial \psi}{\partial x} \frac{\partial H}{\partial y} + \frac{\partial \psi_i}{\partial x} \frac{\partial H_i}{\partial y} = \\ \frac{1}{Re_\infty} \frac{\partial}{\partial y} \left[\mu \left(1 - \frac{1}{Pr} \right) u \frac{\partial u}{\partial y} + \left(\frac{\mu}{Pr} + \frac{\epsilon}{Pr_i} \right) \frac{\partial H}{\partial y} \right] \end{aligned} \quad (31)$$

It has been found convenient in the viscous layer analysis to replace the v-component of velocity with the stream function using the relation

$$\frac{\partial \psi}{\partial x} = -\rho v \quad (32)$$

with the continuity equation, Eq. (16), now replaced by Eq. (28). The difference between the viscous and inviscid pressures is denoted by $\hat{p} = p - p_i$ in Eqs. (29) and (30). It is observed that the EIF in Eqs. (28)-(31) has been expressed in terms of the Euler equations instead of the conservative form of the stream function-vorticity equation discussed in the section of the inviscid flow analysis. This step is taken, including the use of the approximate form of the inviscid normal momentum equation, to insure that as the edge of the viscous layer is approached the imposition of the boundary conditions

$$u \rightarrow u_i \quad \psi \rightarrow \psi_i \quad H \rightarrow H_i \quad \hat{p} \rightarrow 0 \quad (33)$$

results in a smooth merging of the viscous and inviscid solutions as shown in Fig. 6 for the u-component of velocity.

At the surface $y = 0$ the usual viscous boundary conditions

$$u = \psi = 0 \quad H = H_w(x) \quad \text{or} \quad \frac{\partial H}{\partial y} = \dot{q}_w(x) \quad (34)$$

are imposed, where $\dot{q}_w(x)$ denotes the nondimensional form of the specified surface heat transfer.

Transformed Viscous Formulation

Based on previous work in the analysis of separated boundary-layer flows, the finite difference solution of the governing equations is facilitated by the use of a modified form of the Levy-Lees transformation which is given by:

$$\xi = \int_0^x \rho_{ir} u_{ir} \mu_{ir} dx \quad \eta = \frac{y}{\delta^*} h(x) = \eta h(x) \quad (35)$$

In Eq. (35) the ir -subscripted quantities denote the inviscid solution at a reference surface such as the wall or the displacement body. These quantities depend only on x ; further discussion on their treatment in the present study will be presented in the section on the Equivalent Inviscid Flow. Equation (35) shows that the normal coordinate has been scaled by the displacement thickness. Numerical difficulties which were encountered in using this transformation in the present computations of transonic shock induced separated flow were overcome by rescaling the normal coordinate by the boundary-layer thickness, δ and therefore in Eq. (35), $h(x) = \delta^*/\delta$. Further discussion on this point will also be presented in the section on the Equivalent Inviscid Flow.

In the present analysis the inviscid flow is permitted to vary over the viscous layer thickness due to the strong viscous-inviscid interaction which occurs when a transonic shock wave impinges on a turbulent boundary layer. It is therefore necessary to account for this inviscid variation by generalizing the displacement definition to

$$\int_{\delta^*}^{\infty} \rho_i u_i dy = \int_0^{\infty} \rho u dy \quad (36)$$

which states that the mass flow in the equivalent inviscid flow is equal to that in the real viscous flow. In the present investigation it has been found convenient to use an alternative displacement thickness definition given by

$$\delta^* = \frac{1}{\rho_{ir} u_{ir}} \int_0^{\infty} (\rho_i u_i - \rho u) dy \quad (37)$$

Lock (Ref. 28) has explored the difference in these two definitions of δ^* and has concluded that they differ less from each other than they do from the classical definition obtained by setting $\rho_i u_i = \rho_e u_e$ in Eqs. (36) and (37) which leads to

$$\delta^* = \int_0^{\infty} \left(1 - \frac{\rho u}{\rho_e u_e} \right) dy \quad (38)$$

where $\rho_e u_e$ is constant across the boundary layer.

In the viscous layer it is convenient to use a perturbation stream function to represent the difference between the viscous and inviscid stream functions written as

$$\psi - \psi_i = m (1 - \tilde{f}) \quad (39)$$

As $y \rightarrow \infty$ $\tilde{f} \rightarrow 1$ so that the viscous stream function merges smoothly with that of the inviscid solution. At the surface, $y = 0$, the usual boundary condition $\psi = 0$ is imposed by setting $\tilde{f} = 0$ since at the wall the inviscid stream function is set to

$$\psi_i(x, 0) = -m \quad (40)$$

where m is the perturbation mass flow given by

$$m = \rho_{ir} u_{ir} \delta^* \quad (41)$$

The boundary condition given in Eq. (40), which is the representation of the viscous effects in the inviscid flow, will be derived later in the section on the Viscous-Inviscid Interaction Procedure. In first order theory, where the inviscid flow velocity is invariant on the scale of the boundary layer, the inviscid stream function varies linearly in the viscous region. Hence a second perturbation stream function, ψ_{Δ} , is introduced which denotes the deviation of the inviscid stream function from its first order linear variation. This function is given by

$$\psi_{\Delta} = \psi_i - m (\eta - 1) \quad (42)$$

which when combined with Eq. (39) yields the following form for the viscous stream function

$$\psi = m (\eta - \tilde{f}) + \psi_{\Delta} \quad (43)$$

Figure 7 shows the two perturbation stream functions, ψ_{Δ} and \tilde{f} , and the merging of the inviscid and viscous stream functions at the edge of the viscous layer.

The defect form of the viscous layer equations given in Eqs. (28)-(31) are transformed with the independent variables given in Eq. (35) and the dependent variables, other than the stream function, scaled as follows by the inviscid solution at the reference surface:

$$\begin{aligned} F &= \frac{U}{U_{ir}} & F_i &= \frac{U_i}{U_{ir}} & \bar{\rho} &= \frac{\rho}{\rho_{ir}} & \bar{\rho}_i &= \frac{\rho_i}{\rho_{ir}} \\ \bar{\mu} &= \frac{\mu}{\mu_{ir}} & \bar{\epsilon} &= \frac{\epsilon}{\mu_{ir}} & \bar{T} &= \frac{T}{T_{ir}} & \bar{T}_i &= \frac{T_i}{T_{ir}} & g &= \frac{H}{H_{ir}} & g_i &= \frac{H_i}{H_{ir}} \end{aligned} \quad (44)$$

The transformed equations become

$$\frac{\partial \tilde{f}}{\partial \hat{\eta}} = \frac{1}{h} (1 - \bar{\rho} F) + \frac{1}{m} \frac{\partial \psi_{\Delta}}{\partial \hat{\eta}} \quad (45)$$

$$\begin{aligned} m^2 \bar{\rho} F \frac{\partial F}{\partial \xi} - mh \frac{\partial}{\partial \xi} \left[m \left(\frac{\hat{\eta}}{h} - \tilde{f} \right) + \psi_{\Delta} \right] \frac{\partial F}{\partial \hat{\eta}} &= m^2 \bar{\rho}_i F_i \frac{\partial F_i}{\partial \xi} \\ &- mh \frac{\partial}{\partial \xi} \left[m \left(\frac{\hat{\eta}}{h} - 1 \right) + \psi_{\Delta} \right] \frac{\partial F_i}{\partial \hat{\eta}} + m^2 \beta (\bar{\rho}_i F_i^2 - \bar{\rho} F^2) \\ &- \rho_{ir} \delta^{*2} \left[\frac{\partial \hat{\rho}}{\partial \xi} + \hat{\eta} \left(\frac{h'}{h} - \frac{\delta^{*'}}{\delta^*} \right) \frac{\partial \hat{\rho}}{\partial \hat{\eta}} \right] + h^2 \frac{\partial}{\partial \hat{\eta}} \left[(\bar{\mu} + \bar{\epsilon}) \frac{\partial F}{\partial \hat{\eta}} \right] \end{aligned} \quad (46)$$

$$\frac{\partial \hat{\rho}}{\partial \hat{\eta}} = \frac{\bar{\kappa} m U_{ir}}{h} (\bar{\rho} F^2 - \bar{\rho}_i F_i^2) \quad (47)$$

$$\begin{aligned} m^2 \bar{\rho} F \frac{\partial g}{\partial \xi} - mh \frac{\partial}{\partial \xi} \left[m \left(\frac{\hat{\eta}}{h} - \tilde{f} \right) + \psi_{\Delta} \right] \frac{\partial g}{\partial \hat{\eta}} &= m^2 \bar{\rho}_i F_i \frac{\partial g_i}{\partial \xi} \\ &- mh \frac{\partial}{\partial \xi} \left[m \left(\frac{\hat{\eta}}{h} - 1 \right) + \psi_{\Delta} \right] \frac{\partial g_i}{\partial \hat{\eta}} + \frac{h^2}{Pr} \frac{\partial}{\partial \hat{\eta}} \left[\left(\bar{\mu} + \bar{\epsilon} \frac{Pr}{Pr_t} \right) \frac{\partial g}{\partial \hat{\eta}} \right] \\ &+ \frac{h^2 U_{ir}^2}{H_{ir}} \frac{\partial}{\partial \hat{\eta}} \left[\bar{\mu} \left(1 - \frac{1}{Pr} \right) F \frac{\partial F}{\partial \hat{\eta}} \right] \end{aligned} \quad (48)$$

The normalized state equation becomes

$$\frac{\hat{p}}{p_i} = \frac{\bar{p} \bar{T}}{\bar{p}_i \bar{T}_i} - 1 \quad (49)$$

and the temperature is deduced from the total enthalpy definition, Eq. (22), which is now written as

$$\bar{T} = g \left(1 + \frac{\gamma-1}{2} M_{ir}^2 \right) - \frac{u_{ir}^2}{2T_{ir}} \left(F^2 + \frac{v^2}{u_{ir}^2} \right) \quad (50)$$

The v-component of velocity is deduced from the transformation of Eq. (32) given by

$$\frac{v}{u_{ir}} = - \frac{\mu_{ir}}{\bar{p}} \left\{ \frac{\partial}{\partial \xi} \left[m \left(\frac{\hat{\eta}}{h} - \tilde{f} \right) + \psi_{\Delta} \right] + \frac{\hat{\eta} m}{h} \left(\frac{h'}{h} - \frac{\delta^{*'}}{\delta^*} \right) (\bar{p} F - 1) \right\} \quad (51)$$

The Mach number is given by

$$M_{ir} = \sqrt{\frac{u_{ir}^2 + v_{ir}^2}{(\gamma-1) T_{ir}}} \quad (52)$$

The boundary conditions which are imposed on the viscous formulation are given by

$$\hat{\eta} = 0 \quad F = \tilde{f} = 0, \quad g = g_w(\xi) \quad \text{or} \quad \frac{\partial g}{\partial \hat{\eta}} = g'_w(\xi) \quad (53)$$

$$\hat{\eta} \rightarrow \infty \quad F \rightarrow F_i \quad \tilde{f} \rightarrow 1 \quad g \rightarrow g_i \quad \hat{p} \rightarrow 0 \quad (54)$$

where $g'_w(\xi)$ is a prescribed wall heat flux distribution. An important feature of this formulation is that as the boundary-layer edge is approached and the viscous shear and heat conduction terms vanish, the viscous flow solution is required to merge asymptotically with the inviscid solution. Hence the boundary conditions given in Eq. (54) can be imposed at any value $\hat{\eta}_i > 1$. Numerical tests were conducted on a model problem and reported earlier in Ref. 29 to verify this asymptotic behavior.

Equations (45)-(50) along with the Sutherland molecular viscosity law constitute seven equations in the seven unknowns F , \bar{f} , p , g , $\bar{\rho}$, \bar{T} , and $\bar{\mu}$, with the inviscid solution for the equivalent inviscid flow assumed known. The eddy viscosity coefficient $\bar{\epsilon}$ is related to these flow variables through the use of the Cebeci-Smith (Ref. 27) algebraic turbulence model. It was found, as will be presented in the section on the RESULTS and DISCUSSION that a modification to the outer length scale in this model improved the agreement of the predicted results with transonic flow measurements. The imposition of an outer boundary condition on the stream function permits these equations to be solved in the inverse form, that is, the unknown pressure gradient parameter $\beta = (1/u_{iF})/(du_{iF}/d\xi)$ is deduced along with the viscous solution for a prescribed distribution of the perturbation mass flow, m . This approach allows the present generalized viscous formulation to be incorporated into the interaction iteration procedure which has been successfully used in numerous studies (Ref. 30) on first-order viscous-inviscid interaction. It is observed that the present analysis is easily reverted back to a first-order formulation in which the pressure is constant across the boundary layer by setting $F_i = \bar{\rho}_i = \bar{T}_i = 1$, $\psi_\Delta = 0$, and $\hat{p} = 0$. In this case the equivalent inviscid flow is invariant on the scale of the boundary layer and hence $u_i = u_e$, $\rho_i = \rho_e$, $p_i = p_e$ where the edge quantities, denoted by the e-subscript, are constant at each x-station along the surface.

In the present study several approximations have been made to simplify Eqs. (45)-(50). As a first step in the inclusion of normal pressure gradients in an interacting boundary-layer analysis the viscous pressure has been set equal to that of the inviscid flow thereby resulting in $\hat{p} = 0$ with Eq. (47) eliminated from the formulation. This step is thought to be a reasonable approximation since the variation of the pressure across the viscous layer, if it occurs, will exist primarily in the outer region as sketched in Fig. 8. In this region normal pressure gradients are induced in the inviscid flow due to the rapid turning which principally occurs in the present problem at the foot of the shock wave. Hence we allow this inviscid variation of pressure to be imposed on the viscous solution by setting $p(x,y) = p_i(x,y)$ which, as pointed out by LeBalleur (Ref. 21), is less restrictive than the first boundary-layer approximation, $p(x) = p_i(x,0)$. The implementation of the present treatment of the normal pressure gradient will be discussed in detail in the next section on the Equivalent Inviscid Flow. In the future, this generalized or higher-order viscous-inviscid interaction flow model should be further developed by solving Eq. (47) simultaneously with the other viscous layer equations. This step should be straightforward with the present inverse solution procedure since the mean streamline curvature, $\bar{\kappa}$, if it is set equal to that of the displacement surface as recommended by LeBalleur (Ref. 21) and Lock and Firmin (Ref. 3), will be known on each streamwise calculation of these equations.

In addition to this approximate treatment of the normal pressure gradient, the present work has been focused on adiabatic flows with the Prandtl number Pr set equal to unity. This approximation allows us to set $g = g_i = 1$ and therefore eliminate the total enthalpy equation, Eq. (48) from the present analysis. This approximation should have a minimum effect

on the computed results since in adiabatic flows the total enthalpy ratio g only varies by about 5 percent across the viscous layer. The inclusion of the total enthalpy form of the energy equation to study the effect of heat transfer on flows with strong viscous-inviscid interaction is straightforward.

Equivalent Inviscid Flow

The inviscid flow solution in the interior of the viscous layer, which is referred to as the equivalent inviscid flow (EIF), is required for two purposes in the present viscous layer formulation. First it is needed since the viscous equations have been written as the difference (defect form) between the EIF and the real viscous flow (RVF), and second, in the present calculations the viscous streamwise pressure gradient has been approximated as the inviscid streamwise pressure gradient expressed in generalized Levy-Lees variables as

$$\begin{aligned} \frac{\partial p}{\partial x}(x, y) = \frac{\partial p_i}{\partial x}(x, y) = -\frac{\mu_{ir} u_{ir}}{\delta^{*2}} \left\{ \bar{\rho}_i F_i \frac{\partial F_i}{\partial \xi} - m h \frac{\partial}{\partial \xi} \left[m \left(\frac{\hat{\eta}}{h} - 1 \right) \right. \right. \\ \left. \left. + \psi_{\Delta} \right] \frac{\partial F_i}{\partial \hat{\eta}} + m^2 \bar{\rho}_i F_i^2 \beta \right\} \end{aligned} \quad (55)$$

Eq. (55) has been used to approximate the y -variation of the x -pressure gradient only for $y > \delta^*$ or $\eta > 1$. Below $y = \delta^*$ this equation has been replaced with the assumption that the pressure gradient is now independent of y and equal to that of the EIF at the displacement thickness. Hence for $y < \delta^*$

$$\frac{\partial p}{\partial x}(x) = \frac{\partial p_i}{\partial x}(x, \delta^*) \quad (56)$$

which is shown schematically in Fig. 8. Equation (56) should be a reasonable approximation for $y < \delta^*$ since it is known that the normal pressure gradient in the RVF is zero at the wall as shown in Fig. 8.

In order to accommodate this treatment of the pressure gradient, the inviscid reference surface, about which the viscous formulation is normalized, has been chosen as the displacement surface at $\eta = 1$. Hence the ir -subscripted quantities have been taken as the inviscid solution at $y = \delta^*$. In the global viscous-inviscid interaction procedure, just before the viscous solution is updated, the required input from the EIF is computed. Using the current value of δ^* linear interpolation in the y -direction is performed at each x -station to determine the inviscid u -component of velocity and the density at $y = \delta^*$. Denoting these values as $u_{ir} = u_{\delta^*}$ and $\rho_{ir} = \rho_{\delta^*}$, respectively, we now compute the $\hat{\eta}$ -distribution of

$$F_i = \frac{u_i}{u_{\delta^*}}, \quad \bar{\rho}_i = \frac{\rho_i}{\rho_{\delta^*}} \quad (57)$$

and the perturbation inviscid stream function, ψ_{Δ} , from

$$\psi_{\Delta} = \frac{m}{h} \int_0^{\hat{\eta}} (\bar{\rho}_i F_i - 1) d\hat{\eta} \quad (58)$$

using the trapezoid rule of integration. Below the displacement thickness $F_i = \rho_i = 1$ and thus $\psi_{\Delta} = 0$ in this region so that the y-dependence of the streamwise pressure gradient is eliminated. Thus in this region Eqs. (55) and (56) yield

$$\frac{\partial p}{\partial x} = - \frac{\mu \delta^* u_{\delta^*}}{\delta^{*2}} m^2 \beta \quad (59)$$

which is the same as that which would be imposed across the entire viscous layer in a first-order analysis.

It was mentioned in the previous section that it was found necessary to rescale the y-coordinate with the local boundary-layer thickness instead of the displacement thickness which was successfully used in previous first-order analyses of viscous-inviscid interaction (Ref. 30). This modification was needed since some caution was required as to the lateral extent to which the viscous layer equations could be solved. This results because the viscous layer equations have been written in nonconservative form; numerical difficulties were encountered when the viscous solution was extended too far outside of the viscous layer edge due to the nearly discontinuous behavior in the flow field variables in that region. Rescaling by δ eliminated this problem and no numerical difficulties were encountered with the outer boundary in the viscous solution located at $y/\delta = \hat{\eta} = 1.4$.

The viscous layer equations with the imposed EIF are solved with an implicit finite-difference which is first-order accurate in the ξ -coordinate and second-order accurate in the $\hat{\eta}$ -coordinate. The finite difference representation of the EIF terms is treated identically to the corresponding viscous flow convection terms thereby insuring that these terms are in balance as the edge of the viscous layer is approached. Other than the inclusion of the EIF terms the numerical treatment is identical with that used in the first-order viscous analysis which is presented in Ref. 23.

Viscous-Inviscid Interaction Procedure

The viscous induced displacement thickness is represented in the inviscid formulation as a Dirichlet condition for the stream function as

shown in Fig. 3. This boundary condition is discussed in this section along with the global iteration procedure used to numerically link the inviscid stream function analysis to the generalized viscous formulation.

Inviscid Surface Boundary Condition

The defect form of the continuity equation is written as

$$\frac{\partial(\rho_i u_i - \rho u)}{\partial x} + \frac{\partial(\rho_i v_i - \rho v)}{\partial y} = 0 \quad (60)$$

Integration of Eq. (60) from $y = 0$ to $y = \infty$ with the imposition of the boundary conditions

$$y = 0 \quad \rho v = 0 \quad (61)$$

$$y \rightarrow \infty \quad \begin{cases} \rho v \rightarrow \rho_i v_i \\ \rho u \rightarrow \rho_i u_i \end{cases} \quad (62)$$

yields

$$\rho_i(x,0) v_i(x,0) = \frac{d}{dx} \int_0^{\infty} (\rho_i u_i - \rho u) dy \quad (63)$$

Introduction of the stream function from Eq. (1) where the i -subscript is used here to denote the inviscid value, leads to

$$\frac{\partial \psi_i}{\partial x}(x,0) = \frac{d}{dx} \int_0^{\infty} (\rho_i u_i - \rho u) dy \quad (64)$$

This equation is integrated from $x = x_0$ to x to give

$$\psi_i(x,0) - \psi_i(x_0,0) = -m(x) + m(x_0) \quad (65)$$

where m is the perturbation mass flow previously defined as

$$m(x) = \int_0^{\infty} (\rho_i u_i - \rho u) dy \quad (66)$$

It is convenient to choose the constant of integration as $\psi_i(x_0,0) = -m(x_0)$ which leads to the final result

$$\psi_i(x,0) = -m(x) \quad (67)$$

as the inviscid surface boundary condition.

Global Iteration Technique

The iteration procedure shown in Fig. 9 is used to couple the transonic stream function analysis to the viscous formulation described in this report. This iteration technique is a generalization of a procedure (Ref. 20) which has been successfully used in numerous computations of first-order viscous-inviscid interaction. Since the viscous equations are now written in a defect form the viscous and inviscid equations are much more strongly coupled than in a first-order computation where the pressure is assumed constant across the boundary layer. Nonetheless the simple fixed point iteration formula shown in Fig. 9 has been successfully used in the present study to obtain converged interaction solutions. In Fig. 9, the update formula is shown with the relaxation factor, $\bar{\omega}$, set to unity; in general it has been found necessary in the present calculations to use underrelaxation and thus

$$m^{i+1} = m^i \left[1 + \bar{\omega} \left(\frac{u_{\delta_v}^*}{u_{\delta_I}^*} - 1 \right) \right] \quad (68)$$

In Eq. (68) $u_{\delta_v}^*$ and $u_{\delta_I}^*$ denote the viscous and inviscid predictions, respectively, of the inviscid velocity along the displacement surface. In the computed results to be presented in the next section, the quantity, $u_{\delta_I}^*$ has been approximated as the inviscid velocity at the wall, u_{w_I} . This approximation was made to eliminate minor oscillations which resulted when $u_{\delta_I}^*$ was used in the update expression. These oscillations are probably due to the interpolation which is required in the inviscid calculation to find $u_{\delta_I}^*$ since the grid is aligned to the wall and not to the displacement surface. This approximation has a relatively small effect on the results since the inviscid flow changes only slightly between the wall and the displacement thickness.

RESULTS AND DISCUSSION

In this section results are presented using the previously discussed two-layer model (IBLT) for both attached and separated transonic normal shock-wave, boundary-layer interaction including the effects of normal pressure gradients. In addition calculations are presented for these same cases utilizing an inviscid rotational flow model to represent the outer portion of a turbulent boundary layer interacting with an incident normal shock wave. Comparisons made between these two approaches delineate the effect of ignoring the viscous sublayer in the rotational inviscid flow analysis. Assessment is made of these results through comparisons with previous analyses and experimental data. A brief discussion is presented of an improved turbulence model which was applied during this investigation and has been found to give improved agreement of theory and experiment for some quantities for transonic shock induced separated flow. Finally, calculations are shown from the present IBLT which assess the relative importance of boundary-layer displacement effects and normal pressure gradients for transonic shock induced separated flow.

Attached Flow Calculations

A number of investigators (Ref. 2) have demonstrated that an inviscid rotational flow analysis of attached shock-wave boundary-layer interactions gives wall pressure distributions which agree well with experimental data for turbulent flows. In this section calculations are presented using the present stream function-vorticity approach and comparisons are made with the asymptotic theory results of Melnik and Grossman (Ref. 12). In addition some observations are presented on the occurrence of flow separation in the application of inviscid rotational flow theory. Finally it is demonstrated that for attached flow, calculations using IBLT give comparable wall pressure distributions to that obtained from inviscid rotational flow theory.

Inviscid Rotational Flow Analysis

In the application of inviscid rotational flow theory the upstream velocity profile, $u(y)$, is chosen so as to represent the outer portion of a turbulent boundary layer profile. The inner or wall layer is ignored. A critical step in the selection of this profile is the choice of magnitude of the wall slip velocity since it is well known that the results downstream depend on this value. In the present calculations, with the stream function-vorticity approach, it was found that for a given problem a minimum value of the slip velocity exists. If the slip velocity is specified below this value then inviscid separation results with the computed wall pressure distribution found to depart significantly from that observed experimentally. This result is easily explained by a consideration of the total and static pressure distributions as shown schematically in Fig. 10. Here it is seen that upstream of a compressive disturbance, the details of which can be ignored, the total pressure distribution p_t which corresponds to the profile, u_0 , has a minimum at the wall. This value of total pressure remains constant along the wall streamline unless a shock wave extends through the rotational layer and impacts the surface and further reduces the wall total pressure. If the disturbance is of sufficient

strength for a given level of inflow total pressure, then the wall pressure, as shown in Fig. 10, will increase until it is equal to the wall total pressure level thereby resulting in a stagnation point on the wall. This point is also a separation point with the streamline pattern shown in Fig. 10. Downstream the wall pressure decreases due to the finite reversed flow velocity and the requirement that the total pressure remain constant on the wall streamline. This expansion is probably not physically meaningful and is a reflection of the unrealistic assumption of using an inviscid flow theory in a separated flow region. A numerical example of separated inviscid rotational flow is found in the work of Taulbee and Robertson* (Ref. 31). They solved the incompressible form of the stream function-vorticity equation for the inviscid rotational flow over a forward facing step on a flat surface. Their rotational flow model and computed results for two cases are shown in Fig. 11. In Case B the inviscid flow remains attached with a monotonic rise of the wall pressure along the plate ahead of the step; in Case A inviscid separation occurs near the corner with a dip in the static pressure in that region.

In the present rotational inviscid flow analysis of transonic normal shock-wave boundary-layer interaction, inviscid separation was avoided by prescribing the inflow wall slip velocity sufficiently large so that the associated total pressure was greater than the known static pressure downstream of the shock wave. Avoidance of inviscid separation only yields a minimum value for the inflow slip velocity; in actuality a more specific criterion is needed for subsonic and transonic flows similar to that established by Rosen, Roshko, and Pavish (Ref. 32) for supersonic flows over compression corners.

With this minimum slip velocity criterion established, the discussion now turns to a comparison of the results obtained with the present analysis with those computed by Melnik and Grossman (Ref. 12) from a solution of the transonic small disturbance equation which they derived from an asymptotic analysis of rotational flow interacting with a normal shock wave. Figure 12 shows the upstream profile for the u-component of velocity which was used for the rotational inviscid flow analysis of a normal shock-wave, boundary-layer interaction for a free stream Mach number, $M_\infty = 1.12$. In this case the wall slip velocity was equal to 0.68, which is slightly higher than the minimum value of 0.64 required to avoid flow separation. Figure 12 shows the velocity profile computed with the present analysis at the downstream boundary, $x = 15$; it is observed that a large decrease occurs in u in the wall region which would lead to separation if the inflow slip velocity was specified below the minimum value. The upstream profile used by Melnik and Grossman, which is also shown in Fig. 12, extends to the wall without regard to the minimum slip velocity criterion discussed above. In their small disturbance theory the static pressure rises monotonically to the imposed downstream level independent of the occurrence of flow reversal and total pressure considerations since the pressure increase is assumed to be proportional to the velocity decrease, that is, $\Delta p \approx -\Delta u$.

The present computations were made in the region $-15 < x < 15$ and $0 < y < 8$ with the normal shock imposed at $x = 0$. Recall that all lengths are

*The authors express their gratitude to Dr. R. E. Melnik of the Grumman Aerospace Corporation for this reference.

nondimensionalized by the upstream boundary-layer thickness. In order to facilitate the comparison of the present results with those of Melnik and Grossman the approximate shock jump condition which they imposed was used in the present calculation. This condition gives a velocity decrease of $\Delta u = -0.212$ and a corresponding pressure increase $\Delta p = 0.212$, in contrast to the exact Rankine-Hugoniot values of $\Delta u = -0.169$ and $\Delta p = 0.169$ for $M_\infty = 1.12$. The present results were obtained with the zebroid line relaxation scheme which was repeated until the maximum difference equation residual was less than 10^{-5} . The vorticity and entropy were updated after every 10 sweeps of the flow field. In these calculations 81 grid points were evenly distributed in the x-direction which resulted in a streamwise step size of $\Delta x = 0.375$. In the y-direction 21 grid points were distributed nonuniformly with a coordinate stretching used to concentrate 10 of these grid points in the boundary layer, $0 < y < 1$. These grid distributions differ from that used by Melnik and Grossman as they solved in the infinite half-plane, $-\infty < x < \infty$, $0 < y < \infty$ with coordinate stretchings used in both the x and y directions to concentrate the mesh (78 by 57) in the boundary layer and near the shock wave. Melnik and Grossman reported that various studies were made on the effect of the mesh on the accuracy of the method; a similar study should be made in the future with the present calculations to determine the sensitivity of the results to the mesh size and distribution. One test that was performed in the present study was to move the outer computational boundary from $y = 8$ to $y = 16$. Only a small difference was observed in the computed wall pressure distribution.

Figure 13 shows a comparison of the wall pressure obtained from the present formulation of inviscid rotational flow in comparison with that predicted by the asymptotic small disturbance theory of Melnik and Grossman. The good agreement observed between these results is encouraging as there are substantial differences in the two approaches. Later after Melnik and Grossman first presented this result, they included the effect of boundary layer blockage in an axisymmetric channel so that they could compare their predicted wall pressure with the experimental pressure distribution measured by Gadd (Ref. 17) for this $M_\infty = 1.12$ case. They obtained good agreement with the data thereby verifying the accuracy of inviscid rotational flow theory for attached transonic normal shock-wave, boundary-layer interaction.

Before ending this section, it is pointed out that it was found imperative in the present stream function-vorticity method to precisely satisfy the Crocco relation, Eq. 7. Initially, calculations were made using the parallel flow approximation in which the vorticity to pressure ratio and the entropy were assumed constant along lines of $y = \text{constant}$ instead of along streamlines. Although in this case the streamlines only depart slightly from constant y-lines, nonetheless a slight error in the entropy s is exponentially amplified in the computation of the pressure in Eq. 6 which led to spurious pressure variations across the boundary layer in the present calculations. These problems were eliminated by exactly satisfying the Crocco equation with a curve fit of the entropy-stream function distribution at the initial station and the use of analytical differentiation to obtain the vorticity to pressure ratio at any desired point in the flow field.

Interacting Boundary Layer Theory (IBLT)

The discussion in the previous section demonstrates that a continuous pressure rise is produced at the wall if the outer layer of a turbulent boundary layer is modeled as an inviscid rotational layer which interacts with a normal shock wave. A question which has been briefly addressed in the present study is whether or not IBLT is capable of capturing the proper interaction scales of an attached transonic shock-wave, boundary-layer interaction. Only a first-order analysis has been made for this case of $M_\infty = 1.12$ since it was found, as will be discussed later, that inclusion of normal pressure gradients in the viscous layer for a much stronger shock wave with $M_\infty = 1.4$ had only a minor impact on the wall pressure, displacement thickness, and skin friction distributions.

In the IBLT calculation, the inviscid computation was made on the same grid discussed previously. Uniform inviscid inflow was now assumed at the upstream boundary which results in irrotational inviscid flow throughout the computational region since the entropy rise at the shock wave was neglected in the present investigation. The viscous analysis, which is a first-order inverse boundary-layer calculation, was computed on the same streamwise mesh as the inviscid analysis with 100 grid points distributed nonuniformly across the boundary layer. The upstream profile was the same as that used in the inviscid rotational flow calculation only now modified near the wall to satisfy the no slip condition. The IBLT calculation was made with a relaxation factor of $\bar{\omega} = .75$ in the update formula in Eq. (68); 30 global iterations were required to reduce the difference between the viscous and inviscid predictions for the edge velocity down to 10^{-3} .

Figure 13 shows the computed wall pressure from IBLT in comparison with the inviscid rotational flow results obtained by Melnik and Grossman and the present theory. The smooth pressure distribution obtained with IBLT demonstrates that displacement thickness interaction results in an interaction length consistent with that obtained from inviscid rotational flow theory for a transonic normal shock wave impinging on a turbulent boundary layer. Figure 14 shows the computed displacement thickness and skin friction distribution obtained for this case from IBLT. As expected the flow remains attached in this case as separation generally is thought to occur for Mach numbers greater than about 1.3. Nonetheless the present results show that even in this case the boundary-layer response is not trivial as the skin friction coefficient is reduced in half and the displacement thickness doubles in the small streamwise length of this interaction.

It is observed in Fig. 13 that the streamwise length scale of the overall wall pressure rise is only about 10 upstream boundary-layer thicknesses. Since the shock wave in the inviscid flow is computed with a shock capturing technique, there was initial concern that the thickness of the shock transition region induced by the numerical technique could be comparable to that caused by the actual boundary layer. Figure 15 shows the wall pressure obtained from a numerical experiment which was performed to assess the numerical smearing of the shock wave. In this calculation the effect of the boundary layer was removed and only a uniform, irrotational inviscid flow subject to a discontinuity at the outer computational boundary was computed. The wall pressure in Fig. 15 shows that although the shock is slightly smeared at the wall the streamwise length scale of

this pressure rise is significantly less than that induced by the actual boundary layer. Similar tests to this were performed throughout the present investigation which verified that the artificial viscosity used in the inviscid scheme had a minimum impact on the overall results.

Separated Flow Calculations

Attention is now focused on the analysis of transonic normal shock-wave, turbulent boundary-layer interactions in which the shock wave is of sufficient strength to separate the boundary layer. The detailed experimental data of Kooi (Refs. 5 and 6) has been extensively used in this investigation to evaluate the present IBLT calculations with and without the inclusion of normal pressure gradients. In this section both free air and bounded channel calculations are presented for the Kooi data. Also, inviscid rotational flow calculations are compared with Kooi's wall pressure distribution for a case in which flow separation occurs.

Free Air Results

Kooi performed a detailed experimental investigation of transonic shock-wave, boundary-layer interaction in the channel shown schematically in Fig. 16. A normal shock wave was established in this passage by placing a "choking wedge" on the lower flat plate; the choking wedge was positioned in the stream direction such that a normal shock wave emanated from the leading edge of the upper flat plate. This shock wave impinged on the lower flat plate boundary layer which was tripped to turbulent near the leading edge as shown in Fig. 16. For $M_\infty = 1.4$, which is the case computed in the present investigation, Kooi experimentally deduced that the boundary-layer thickness δ_o^* on the lower surface, just upstream of interaction region, is 6.6 mm. This value of δ_o^* has been used to nondimensionalize all lengths in the present results and in the presentation of the experimental measurements of Kooi. We have used Kooi's data exclusively from Ref. 5; later he investigated the effects of higher Mach numbers by testing at $M_\infty = 1.44$ and 1.46.

An attempt was made to compute the Kooi $M_\infty = 1.4$ case with the outer computational boundary treated as a "free air" boundary as shown in Fig. 3. This "free air" boundary was placed at the location of the upper wall shown in Fig. 16 which is at $y = 12.1$ (80 mm). Along this boundary ψ was set equal to a constant with ρ and u set equal to 1 ahead of the shock wave and at the respective Rankine-Hugoniot values downstream of the shock. The x-coordinate has been redefined as $x = (x - x_o^*)/\delta_o^*$ where x_o^* is the x-location of the start of interaction. A value of $x_o^* = 426$ mm has been inferred from Kooi's measurements (Ref. 5) and has been used to scale the x-coordinate both in the theoretical and experimental results.

The free air IBLT calculation of the Kooi $M_\infty = 1.4$ case was made in the computational region, $-4 < x < 26$ and $0 < y < 12$. In the inviscid calculation 100 grid points were evenly spaced in the x-direction with $\Delta x = .30$; in the y-direction a coordinate transformation was used to establish a nonuniform grid distribution with the smallest spacing of $\Delta y = .1025$ placed at the wall. In the viscous calculation the streamwise grid was the same as that used in the inviscid calculation; in the y-direction 100 grid points were nonuniformly distributed across the boundary layer with the

smallest spacing placed near the wall. The viscous grid was extended with a constant 9 percent stretching from the wall to a maximum η of 22. In this calculation the effects of normal pressure gradients have not been included and hence $\hat{\eta} = \eta$ with $h = 1$. A total of 40 global viscous-inviscid iterations were made to obtain a converged solution.

Figure 17 shows the present IBLT calculation for the wall pressure, displacement thickness, and skin friction in comparison with the experimental measurements of Kooi (Ref. 5). The Reynolds number for this flow is 2.97×10^5 based on the free stream quantities and the boundary-layer thickness, $\delta_0^* = 6.6$ mm, upstream of the interaction. Figure 17 shows significant differences between the theoretical and experimental results; these differences are primarily due to the boundary-layer blockage effects which existed in the experiment that prevented the experimental wall pressure from rising downstream to the Rankine-Hugoniot normal shock value. In the experiment the large boundary-layer growth produced by the shock wave accelerates the subsonic channel flow downstream of the shock wave and therefore has a significant effect on the interaction flow field results as shown in Fig. 17. In contrast the IBLT calculation shows that, if the pressure rises to the Rankine-Hugoniot level, then the overall growth of the displacement thickness and the streamwise extent of the separated flow region is much larger than that measured experimentally. Fortunately we were able to account for the blockage effect in this experiment by imposing in the IBLT calculation the static pressure distribution measured by Kooi along the line $y^* = 45$ mm or $y = 6.8$ above the lower flat plate. This computational region located in the interior of the Kooi channel is shown in Fig. 16 and will be utilized in the calculations to be discussed in the remainder of this report. Before the IBLT results are presented a brief examination is made of the use of inviscid rotational flow theory for the prediction of separated transonic shock-wave, boundary-layer interaction.

Inviscid Rotational Flow Analysis

Figure 18 shows the inflow profiles of velocity and the corresponding entropy-stream function distribution used in the inviscid rotational flow analysis of the Kooi $M_\infty = 1.4$ case. The velocity profile was prescribed so that it matches the experimental data over most of the boundary layer; however due to the minimum slip velocity constraint, which was previously discussed, the prescribed inflow velocity deviates from the experiment near the wall as shown in Fig. 18. Also shown in Fig. 18 is a prediction of this initial boundary layer profile using the first-order direct version of the present boundary-layer analysis subject to a zero pressure gradient. This calculation was started at the leading edge of the flat plate with instantaneous transition from laminar to turbulent flow assumed to occur at the location of the experimental trip strip, shown in Fig. 16. Excellent agreement is shown here between the predicted and measured results.

Figure 19 shows the computational mesh used in this inviscid rotational flow analysis. The mesh consists of 81 evenly distributed x-grid points with $\Delta x = .30$ and 21 y-grid points distributed as shown in Fig. 19. Approximately 8 points were placed in the boundary layer with the minimum $\Delta y = .0883$ located at the wall.

A comparison of the wall pressure computed from inviscid rotational flow theory with Kooi's experimental measurements is shown in Fig. 20. In contrast with the inviscid rotational theory result shown in Fig. 13 for $M_\infty = 1.12$, the present calculation at $M_\infty = 1.4$ shows a nearly discontinuous rise in the wall pressure at the imposed shock location of $x = 3.6$. The lack of upstream influence is expected in the $M_\infty = 1.4$ case since the entire upstream inviscid flow was supersonic with the minimum Mach number, $M = 1.13$, occurring at the wall. In the $M_\infty = 1.12$ case the sonic line of the entering profile was located at $y = .4$ with a subsonic slip Mach number of $M = .72$. It should be noted that the lack of upstream influence does not prevent inviscid rotational flow theory from being successfully used to describe supersonic interacting flow fields. For example, Roshko and Thompke (Ref. 33) showed very good agreement between theory and experiment for the $M_\infty = 3.93$ flow over a 15 deg compression corner. In this case the flow remained attached with a discontinuous rise in the wall pressure at the corner followed downstream by a continuous compression to the wedge pressure level.

The poor agreement shown in Fig. 20 demonstrates the inadequacy of inviscid rotational flow theory for the prediction of the wall pressure distribution when the shock wave is of sufficient strength to separate the boundary layer. In contrast with the attached flow case where the viscous wall layer is passive and hence can be ignored the increase in shock strength now results in such a large increase in pressure that the wall layer grows significantly thereby displacing the outer portion of the boundary layer. Therefore the wall layer must be actively included in the interaction calculation. In the two-layer IBLT technique, for which separated flow results are presented in the next section, the viscous layer is treated in its entirety without a breakdown into an outer inviscid rotational layer and a viscous wall layer. This latter viscous-inviscid interaction flow model has been designated as a three-layer model as shown in Fig. 2 and is presented in Appendix A.

Channel Results for IBLT with Normal Pressure Gradients

In this section comparisons are presented between the present computations of IBLT with normal pressure gradients and the transonic shock induced separation data of Kooi (Ref. 5). First the details of the numerical calculation will be given and then a brief discussion of a modification to the Cebeci-Smith algebraic turbulence model which was found to improve the agreement of the theoretical prediction with the data.

The IBLT calculations were performed in the "channel" computational region shown in Fig. 16 with the experimental pressure distribution (shown in Fig. 23) imposed along the outer boundary ($y = 6.8$) to account for the boundary-layer blockage effect which was previously discussed. The inviscid grid distribution that was used is the same as that shown in Fig. 19 which was used in the rotational inviscid calculation. The inclusion of normal pressure gradients in the IBLT calculation requires a fine grid to be used in the inviscid analysis near the surface to provide an accurate description of the equivalent inviscid flow (EIF) quantities which are input to the viscous layer analysis. The viscous calculation used the same streamwise mesh as the inviscid analysis to avoid interpolation which has been found in previous interaction calculations (Ref. 30) to cause oscillations. In the normal direction, 101 grid points were nonuniformly

distributed from the wall across the viscous layer to $\hat{n} = 1.45$. The iteration between the viscous and inviscid analyses were performed with the global technique shown in Fig. 9. In the present calculations a converged solution was obtained first for first-order IBLT in which the pressure was assumed constant across the boundary layer. This calculation in which $\bar{\omega} = .4$, required 50 global iterations to reduce the difference between the viscous and inviscid prediction for u_e to 10^{-3} . These results were then used to initialize the IBLT calculation with normal pressure gradients. In the latter calculation it was found necessary to reduce $\bar{\omega}$ to .2 to obtain convergence which was achieved in typically 20 global iterations. The reduction of the global relaxation factor is not surprising since the coupling between the viscous and inviscid flows is significantly greater with the inclusion of the numerical results for the equivalent inviscid flow in the viscous defect equations.

It is well known that use of the Cebeci-Smith algebraic turbulence model generally results in an overprediction of the pressure and an underprediction of the displacement thickness in the analysis of separated turbulent flow. In the past it has been found that some improvement in the predicted results could be obtained by a reduction in the local values of the eddy viscosity coefficient predicted by this model. One example of this type of modification is the Shang-Hankey (Ref. 34) relaxation model which has been used by a number of investigators for the computation of separated turbulent flow. In this model both the inner and outer layer eddy viscosity levels are constrained to depart by only a specified amount from an upstream equilibrium boundary layer level. More recently a simple numerical experiment by Carter (Ref. 35) demonstrated that a reduction in the outer region length scale, which Clauser (Ref. 36) deduced as the incompressible displacement thickness for mild pressure gradient flows, resulted in similar improvements to the separated flow predictions as demonstrated by others with the Shang-Hankey model. In a recent study conducted by Edwards (Ref. 37), the incompressible turbulent separated flow data of Simpson, et al. (Ref. 38) was examined to determine if a modified outer length scale could be inferred from their detailed measurements for the streamwise velocity profiles and the Reynolds stress distributions. It was found that if the outer eddy viscosity coefficient was based on the incompressible momentum thickness instead of the incompressible displacement thickness then a significant improvement was found in the correlation of the maximum Reynolds shear stress with the local gradient of the mean velocity profile. With this modification the outer region eddy viscosity coefficient is expressed as

$$\frac{\epsilon}{\mu} = 0.0168 H_F \frac{\rho}{\mu} u_e \theta_{inc} \quad (69)$$

where the quantity H_F is the flat plate incompressible shape factor $\delta_{inc}^*/\theta_{inc}$ equal to 9/7, and the quantity θ_{inc} is the incompressible momentum thickness. For flat plate flows this model is identical to Clauser's model. As will be seen in this section this modified Cebeci-Smith (CS) turbulence model has improved the present predictions for transonic shock wave, boundary-layer interaction.

Figure 21 shows a comparison of the present computations from IBLT with the experimental data of Kooi (Ref. 5) for the wall pressure,

displacement thickness, skin friction coefficient, momentum thickness and shape factor for $M_\infty = 1.4$. Kooi used the same generalized definitions of the displacement thickness and the momentum thickness in presenting his experimental results as has been used in the present theoretical study. The skin friction coefficient is based on the flow properties at the boundary-layer edge which in the calculations has been defined where $F = .995F_1$ and in the experiment as the point where the pitot pressure became constant. The computed results are shown for both the CS and the modified CS turbulence model discussed above. The position of the imposed normal shock wave is indicated in Fig. 21. Figures 21(a) and (b) show that good agreement is obtained with the data with the present IBLT using the modified CS turbulence model. The agreement shown for the wall pressure is substantially better than that shown earlier for the free air IBLT calculation and that predicted by the inviscid rotational flow analysis. Comparison of Figs. 21(a) and (b) show that the turbulence model modification simultaneously improves the agreement for the wall pressure and the displacement thickness which substantiates the use of the displacement body concept in separated flows. The distributions of the skin friction coefficient in Fig. 21(c) compare the extent of the separated region in the present calculations with that deduced by Kooi from his measured velocity profiles. Both of the results obtained with the CS and modified CS turbulence model show good agreement with the data in the approach to the separation point which occurs just upstream of the location of the imposed normal shock wave. However, downstream the modified model underpredicts the experimental skin friction and therefore predicts a much larger separated flow region than that found experimentally or in the present calculation using the unmodified CS turbulence model. Modification to the outer region of the CS turbulence model has resulted in an improved prediction of the wall pressure and displacement thickness; the lack of agreement for the skin friction indicates that further work is required to correspondingly improve the accuracy of the IBLT with the modified CS turbulence model in the near wall region. A similar trend is observed in Fig. 21(d) for the momentum thickness comparisons in which it is seen that the modified model underpredicts the measured θ distribution. This result is not surprising since the momentum thickness, as well as the skin friction, is strongly influenced by the near wall solution. Finally, the distributions of the shape factor, $H = \delta^*/\theta$, are shown in Fig. 21(e) in which it is seen that neither model accurately predicts the experimental distribution.

Figure 22 shows a comparison of the computed and the experimental profiles for the u-component of velocity at 7 streamwise locations upstream and downstream of the normal shock wave. The insert in Fig. 22 shows the x-location of these profiles; the corresponding station number used by Kooi (Ref. 5) to label these profiles has also been included. Linear streamwise interpolation was used in the calculations to obtain the computed profiles at the same x-location as that of the experimental measurements. The edge velocity, u_e , used to normalize the u-profile was determined by the same criterion mentioned earlier for the respective theoretical and experimental boundary-layer thicknesses.

The velocity profiles shown in Fig. 22 illustrate the rapid changes which occur in a turbulent boundary-layer profile due to an incident normal shock wave. For example, comparison of the experimental profile at $x = .4$ with that just downstream of the shock wave at $x = 3.8$ shows the enormous change which occurs in only 3 upstream boundary-layer thicknesses. The velocity profiles in Fig. 22 show that the IBLT results obtained with the modified CS turbulence model are in overall better agreement with the experimental data than those results obtained without this modification. The agreement is particularly good in the outer region of the turbulent boundary layer where this modification was made. Downstream of the shock wave the modified model underpredicts the velocity recovery in the near wall region as was expected from the skin friction and momentum thickness comparisons shown in Fig. 21. The results obtained with the unmodified model show a higher velocity in the wall region at each location than the modified model which is consistent with the skin friction difference shown in Fig. 21. Despite the complexity of this flow, it is observed in Fig. 22 that the overall growth of the viscous layer, which appears to have distinct edge, is well predicted by the present IBLT with the modified CS turbulence model. The details of the flow at the edge of the viscous layer where the real viscous flow (RVF) and the equivalent inviscid flow (EIF) merge will be discussed later.

Figure 23 shows a comparison of the computed and measured static pressure distributions at various y -levels in the flow field. The IBLT results which are shown are those obtained with the modified CS turbulence model. As mentioned previously, the static pressure distribution at $y = 6.8$, which is the location of the outer inviscid computational boundary, was set equal to that measured by Kooi in order to account for the effect of boundary layer blockage. At the other y -locations shown in Fig. 23 the agreement of the IBLT result with the experiment is good except just downstream of the shock wave where the pressure is overpredicted. Further work is needed to eliminate this pressure overshoot. Figure 23 shows that the static pressure varies between the wall and $y = 2.3$. Later in this section the detailed pressure variation across the viscous layer will be presented.

Figure 24 shows the flow structure deduced from the present calculation with the modified CS turbulence model in comparison with that deduced by Kooi from his measurements and Schlieren photographs. Outside of the immediate shock wave regions, the theoretical and experimental Mach contours in the inviscid flow region show the same pattern, particularly downstream of the shock wave. Overall the agreement between the predicted and measured flow structure is considered reasonable. Further research is needed to determine why the triple or lambda shock structure observed in the experiment is not present in the theoretical flow pattern. It is possible that this difference is due to the neglect of the entropy rise or total pressure decrease across the shock in the IBLT calculation.

The variation of the pressure across the boundary layer from the equivalent inviscid flow (EIF) is shown in Fig. 25 for selected streamwise stations both upstream and downstream of the shock wave which is located at $x = 3.6$. The x -location of each of these normalized pressure profiles is

shown in a scaled drawing inserted into Fig. 25. Since the variation in the static pressure across the viscous layer was insensitive to the turbulence model only the IBLT results with the modified CS turbulence model are shown in Fig. 25. The arrows on each of the profiles are the edge of the viscous layer. The kink in the profiles near the wall is at the displacement thickness since, as was discussed earlier, the pressure was assumed constant from δ^* to the wall. Figure 25 shows the anticipated trend in the static pressure variation in that in the immediate vicinity of the shock wave the pressure decreases with increasing y upstream of the shock wave and increases with increasing y downstream of the shock wave. The variation of the static pressure across the viscous layer reaches a maximum of about 10 percent in the immediate vicinity of the impinging shock wave; as expected, this variation vanishes upstream and downstream of this region as the flow returns to that of a conventional constant pressure boundary layer.

Figures 26 shows the u -velocity component functions from the real viscous flow (RVF) and equivalent inviscid flow (EIF) at the same streamwise stations both upstream and downstream of the shock wave as were shown for the viscous layer pressure in Fig. 25. The EIF and RVF stream functions are shown in Fig. 27 at several streamwise locations. As discussed previously for the static pressure, the EIF for the u -velocity and density were assumed constant for $0 < y < \delta^*$ in the present calculations. Hence the stream function varies linearly in this region. Figures 26 and 27 show the smooth merging between the RVF and EIF as the edge of the viscous layer is approached. No numerical difficulties were encountered in the implementation of these outer boundary conditions. Examination of the velocity profiles show the same trends as that observed for the static pressure, that is, upstream of the shock wave the decrease in the pressure from the wall to the edge the viscous layer results in a corresponding velocity increase as shown for the EIF at $x = 2.0, 2.9$ and 3.5 . Downstream of the shock wave the opposite trend occurs as evidenced by the decrease in velocity across the viscous layer in the EIF for $x > 3.6$. Then further downstream as seen in Fig. 26(c) the velocity from the EIF varies much less across the boundary layer as the strong interaction between the viscous and inviscid flows subsides. These results demonstrate the present capability to account for the variation of the inviscid flow on the scale of the boundary layer; however the variation of the EIF in the viscous layer is small as seen in the small changes in the pressure, velocity and the linearity of the stream function in this region. This suggests that the inclusion of normal pressure gradients play a secondary role in the present calculations. This topic is addressed in further detail in the last section of this report.

The viscous streamline pattern computed for this $M_\infty = 1.4$ case is shown in Fig. 28. The vertical scale has been enlarged in order to display the details of the separation bubble. Only the streamlines below the displacement thickness are shown. It is observed in Fig. 28 that separation occurs just upstream of the normal shock wave with a rapid turn in the viscous streamlines propagating across the viscous layer. Downstream of the shock wave the streamline pattern is smoother. The height of the

separation bubble increases to about 0.1 of the upstream undisturbed boundary-layer thickness.

Comparison of IBLT With and Without Normal Pressure Gradient

One of the advantages of the present approach is that IBLT computations can be made with and without normal pressure gradients in order to assess the relative importance of including pressure variations across the viscous layer. With the pressure assumed constant across the viscous layer the present analysis reverts back to a first-order inverse boundary layer scheme interacting with the outer inviscid flow through displacement thickness coupling. Figure 29 shows a comparison of the wall pressure, displacement thickness, and skin friction computed from IBLT with and without normal pressure gradients. These calculations were made with the modified CS turbulence model. Comparison of these results shows that the effect of including normal pressure gradients is relatively minor and has less of an impact on the results than the change in the turbulence model discussed previously. A similar conclusion is reached by examining the velocity profiles. Typical results are shown in Fig. 30 for the flow just upstream and downstream of the shock wave in which only minor changes occur in the velocity profile when the normal pressure gradient is deleted from the analysis. Although the present treatment of normal pressure gradients is an approximate one, it appears from these calculations that the dominant viscous effect in the prediction of separated transonic shock-wave, boundary-layer interaction is the inclusion of displacement thickness interaction. The solutions shown in Figs. 29 and 30 demonstrate that meaningful results can be obtained with IBLT without the inclusion of normal pressure gradients. In the future work should be directed toward additional data comparisons over a range of transonic shock strengths to further substantiate this conclusion.

CONCLUDING REMARKS

In this report a technique based on a two-layer model has been presented for the analysis of transonic shock-wave, boundary-layer interaction with particular emphasis on turbulent separated flow. In this technique, which is referred to as Interacting Boundary Layer Theory (IBLT), a finite difference solution of the viscous layer equations, expressed in a defect form, is iteratively solved with the finite difference form of the inviscid stream function-vorticity equation. Normal pressure gradients and embedded shock effects have been included in the viscous layer analysis by assuming that the pressure in this region is the same as that of the inviscid flow above the displacement thickness. A number of IBLT calculations for both attached and separated flow along with detailed comparisons with experimental data lead to the conclusions presented below. In addition the rotational inviscid flow model of shock, boundary-layer interaction has been implemented through the use of the present inviscid stream function-vorticity method. Conclusions are also drawn from calculations made with this inviscid interaction approach.

The major conclusion which is drawn from the present work is that displacement thickness interaction is the dominant effect which must be included in a viscous-inviscid interaction scheme for the prediction of transonic shock-wave, boundary-layer interaction where the shock is of sufficient strength to separate the turbulent boundary layer. Comparisons with the $M_\infty = 1.4$ case measured by Kooi indicate that for this separated flow, the computed results shows greater sensitivity to the turbulence model than to whether or not normal pressure gradients are included in the analysis. In this case the pressure was found to vary only by about 10 percent across the viscous layer; hence it is not surprising that the IBLT calculations proved to be relatively insensitive to whether or not this effect was included. In the future additional data comparisons should be made, particularly as the shock strength is increased, to further substantiate this conclusion. Unfortunately, most of the data for transonic shock-wave, boundary-layer interaction has been taken in small wind tunnels where it is necessary, as was found in the present analysis of Kooi's data, to include the effect of boundary layer blockage.

Favorable comparisons have been obtained with the present IBLT for Kooi's data for the pressure, displacement thickness, and velocity profiles in which a modified Cebeci-Smith turbulence model has been used. This modification which is a straightforward change in the length scale in the outer region, provides encouragement that a simple eddy viscosity model may be adequate for the prediction of many of the flow properties in a turbulent separated flow. However the skin friction and momentum thickness comparisons indicate that further work is needed to improve this model in the inner or wall region.

The present calculations demonstrate that IBLT can produce meaningful overall results for this complex flow field. However, the details of the lambda shock pattern, generally observed when the flow separates, are not present in the IBLT calculation. Resolution of this flow structure would

require inclusion of the exact shock jump conditions and the use of an extremely fine computational mesh in order to delineate the details of the triple shock point and the entropy and total pressure jump which occur across the shear layer emanating from this point.

Favorable comparisons which have been made with the asymptotic theory of Melnik and Grossman indicate that the present transonic stream function-vorticity approach can be used as an inviscid rotational flow model of shock interaction if the flow remains attached. Calculations are also included which show that this model, as expected, is completely inadequate if the flow separates. In this case, viscous effects, as demonstrated by the sensitivity of the present results to the displacement thickness and the turbulence model, must be included in the interaction analysis.

A favorable comparison was also obtained with the attached flow results of Melnik and Grossman with the present IBLT, without the inclusion of normal pressure gradients. The advantage of this approach over the rotational inviscid flow theory is that the entire boundary layer is solved at once without breaking it into numerous layers which require several solutions to obtain the entire solution.

ACKNOWLEDGEMENTS

The authors acknowledge the interest and technical guidance that Dr. M. J. Werle of UTRC has provided for the work presented in this report. In addition the authors acknowledge the benefit of numerous technical discussions with Dr. V. N. Vatsa of UTRC during the course of this work.

REFERENCES

1. Adamson, T. C., Jr. and A. F. Messiter: Analysis of Two-Dimensional Interactions Between Shock Waves and Boundary Layers, *Ann. Rev. Fluid Mech.*, pp. 103-138, 1980.
2. Melnik, R. E.: Turbulent Interactions on Airfoils at Transonic Speeds - Recent Developments, AGARD Conference on Viscous-Inviscid Interactions, AGARD Conference Proceedings No. 291, 1981.
3. Lock, R. C. and M. C. P. Firmin: Survey of Techniques for Estimating Viscous Effects in External Aerodynamics, RAE Technical Memorandum Aero 1900, April 1981.
4. Seddon, J.: The Flow Produced by Interaction of a Turbulent Boundary Layer with a Normal Shock Wave of Strength Sufficient to Cause Separation, British ARC R&M No. 3502, 1967.
5. Kooi, J. W.: Experiment on Transonic Shock-Wave Boundary Layer Interaction, AGARD CP-168, 1975.
6. Kooi, J. W.: Influence of Free-Stream Mach Number on Transonic Shock Wave Boundary Layer Interaction, NLR MP 78013 U, National Aerospace Laboratory, Netherlands, 1978.
7. Om, D., M. E. Childs and J. R. Viegas: An Experimental Investigation and a Numerical Prediction of a Transonic Normal Shock Wave/Turbulent Boundary Layer Interaction, AIAA Paper 82-0990, June 1982.
8. Om, D. and M. E. Childs: An Experimental Investigation of Transonic Multiple Shock/Turbulent Boundary Layer Interactions in Circular Duct, AIAA Paper No. 83-1744, July 1983.
9. East, L. F.: The Application of a Laser Anemometer to the Investigation Shock Wave Boundary Layer Interactions, AGARD-CP-193, 1976.
10. Viegas, J. R. and C. C. Horstman: Comparison of Multiequation Turbulence Models for Several Shock Boundary-Layer Interaction Flows, AIAA J., Vol. 17, pp. 811-820, August 1979.
11. Shea, J. R., III: A Numerical Study of Transonic Normal Shock - Turbulent Boundary Layer Interactions, AIAA Paper No. 78-1170, 1978.
12. Melnik, R. E. and B. Grossman: Analysis of the Interaction of a Weak Normal Shock Wave with a Turbulent Boundary Layer, AIAA Paper No. 74-598, 1974.
13. Adamson, T. C., Jr. and A. Feo: Interaction Between a Shock Wave and a Turbulent Boundary Layer in Transonic Flow, *SIAM J. Appl. Math.*, Vol. 29, pp. 121-145, 1975.

14. Messiter, A. F.: Interaction Between a Normal Shock Wave and Turbulent Boundary Layer at High Transonic Speeds, Pt. I: Pressure Distribution, NASA CR-3194, 1979.
15. Lighthill, M. J.: On Boundary Layers and Upstream Influence, II, Supersonic Flows without Separation, Proc. Roy. Soc., Series A, Vol. 217, 1953.
16. Melnik, R. E. and B. Grossman: Further Developments in an Analysis of the Interaction of a Weak Normal Shock Wave with a Turbulent Boundary Layer, Symposium Transsonicum II, Springer-Verlag, New York, pp. 262-272, 1975.
17. Gadd, G. E.: Interactions Between Normal Shock Waves and Turbulent Boundary Layers, British A.R.C. 22559, R&M 3262, 1962.
18. Catherall, D. and K. W. Mangler: The Integration of the Two-Dimensional Laminar Boundary-Layer Equations Past the Point of Vanishing Skin Friction, J. Fluid Mech., Vol. 26, Pt. 1, September 1966.
19. LeBalleur, J. C.: Couplage Visqueux-non Visqueux: Methode Numerique et Applications Aux Ecoulements Bidimensionnels Transsoniques et Supersoniques, La Recherche Aerospatiale, No. 1978-2, pp. 65-76, 1978.
20. Carter, J. E.: A New Boundary-Layer Inviscid Iteration Technique for Separated Flow, AIAA Paper No. 79-1450, AIAA 4th Computational Fluid Dynamics Conference, Williamsburg, VA, July 23-24, 1979.
21. LeBalleur, J. C.: Strong Matching Method for Computing Transonic Viscous Flows Including Wakes and Separations, Lifting Airfoils, La Recherche Aerospatiale, No. 1981-3, English Edition, 1981.
22. East, L. F.: A Representation of Second-Order Boundary Layer Effects in the Momentum Integral Equation and in Viscous-Inviscid Interactions, RAE Technical Report 81002, 1981.
23. Carter, J. E.: Inverse Boundary Layer Theory and Comparison with Experiment, NASA TP-1208, September 1978.
24. Hafez, M. M. and D. Lovell: Numerical Solution of the Transonic Stream Function Equation, AIAA J., Vol. 21, No. 3, March 1983.
25. Hafez, M. M. and J. C. South: Vectorization of Relaxation Methods for Solving Transonic Full Potential Equation, Numerical Methods for the Computation of Inviscid Transonic Flow with Shock Waves, GAMM Workshop, Sweden, 1979.
26. Hafez, M. M., J. C. South and E. M. Murman: Artificial Compressibility Methods for Numerical Solution of Transonic Full-Potential Equation, AIAA Paper No. 78-1148, July 1978.
27. Cebeci, T. and A. M. O. Smith: Analysis of Turbulent Boundary Layers, Academic Press, 1974.

28. Lock, R. C.: A Review of Methods for Predicting Viscous Effects on Aerofoils and Wings at Transonic Speeds, AGARD Conference on Viscous-Inviscid Interactions, AGARD Conference Proceedings No. 291, 1981.
29. Carter, J. E. and M. M. Hafez: Analysis of Imbedded Transonic Shock Wave Influence on Turbulent Boundary Layer Separation, Annual Report on AFOSR Contract F49620-81-C-0041, UTRC Report No. R82-915712-1, 1982.
30. Carter, J. E. and V. N. Vatsa: Analysis of Separated Boundary Layer Flows, Presented at the Eighth International Conference on Numerical Methods in Fluid Dynamics, Aachen, West Germany, June 28 - July 2, 1982.
31. Taulbee, D. B. and J. M. Robertson: Turbulent Separation Analysis Ahead of a Step, ASME Journal of Basic Engineering, pp. 544-550, September 1972.
32. Rosen, R., A. Roshko and D. L. Pavish: A Two Layer Calculation for the Initial Interaction Region of the Unseparated Supersonic Turbulent Boundary Layer with a Ramp, AIAA Paper No. 80-0135, 1980.
33. Roshko, A. and G. J. Thomke: Supersonic, Turbulent Boundary Layer Interaction with a Compression Corner at Very High Reynolds Numbers, Proc. of the Symposium on Viscous Interaction Phenomena in Supersonic Hypersonic Flow, USAF Aerospace Research Laboratories, Wright Patterson AFB, OH, University of Dayton Press, May 1969.
34. Shang, J. S. and W. L. Hankey, Jr.: Numerical Solution for Supersonic Turbulent Flow Over a Compression Ramp, AIAA J., Vol. 13, pp. 1368-1374, 1975.
35. Carter, J. E.: Viscous-Inviscid Interaction Analysis of Transonic Turbulent Separated Flow, AIAA Paper No. 81-1241, June 1981.
36. Clauser, F. H.: The Turbulent Boundary Layer, Advances in Applied Mechanics, Vol. 4, pp. 1-51, 1956.
37. Edwards, D. E.: Analytical Study of Turbulent Separated Flow, UTRC report to be published, 1984.
38. Simpson, R. L., T. T. Chew and B. G. Shivaparsad: The Structure of a Separating Turbulent Boundary Layer, Part 1, Mean Flow and Reynolds Stresses, J. Fluid Mechanics, Vol. 113, pp. 23-51, 1981.

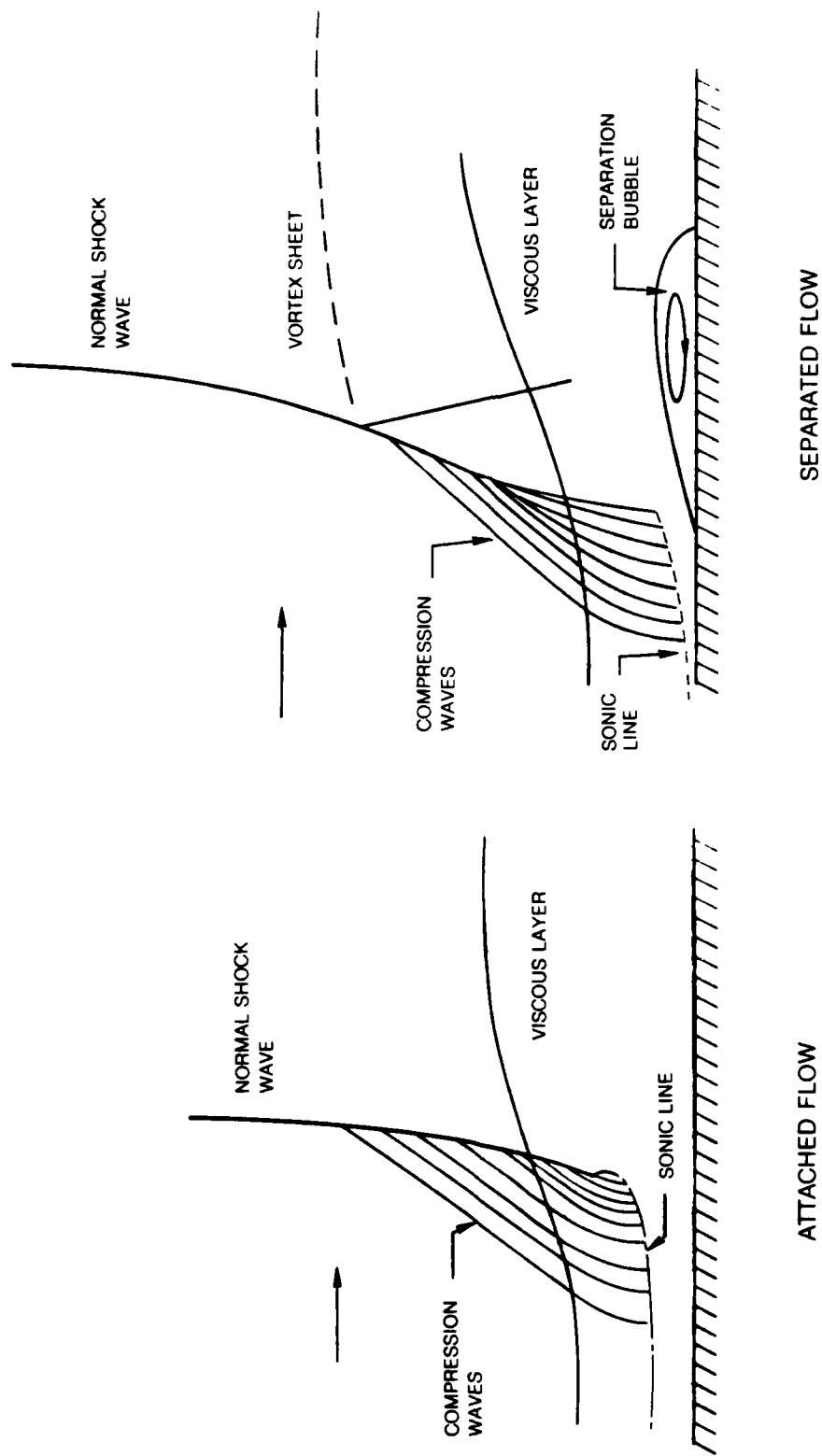


Fig. 1 Normal shock wave impinging on a turbulent boundary layer

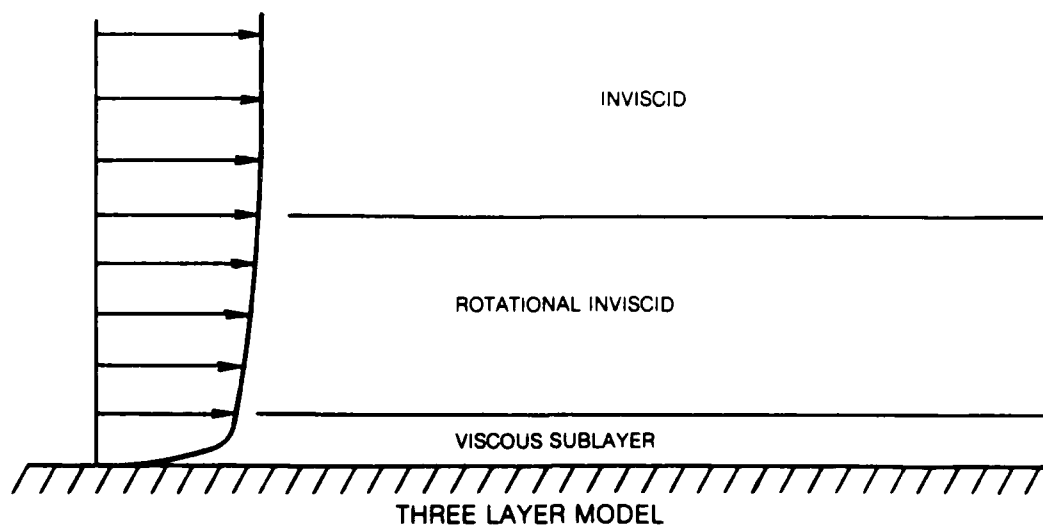
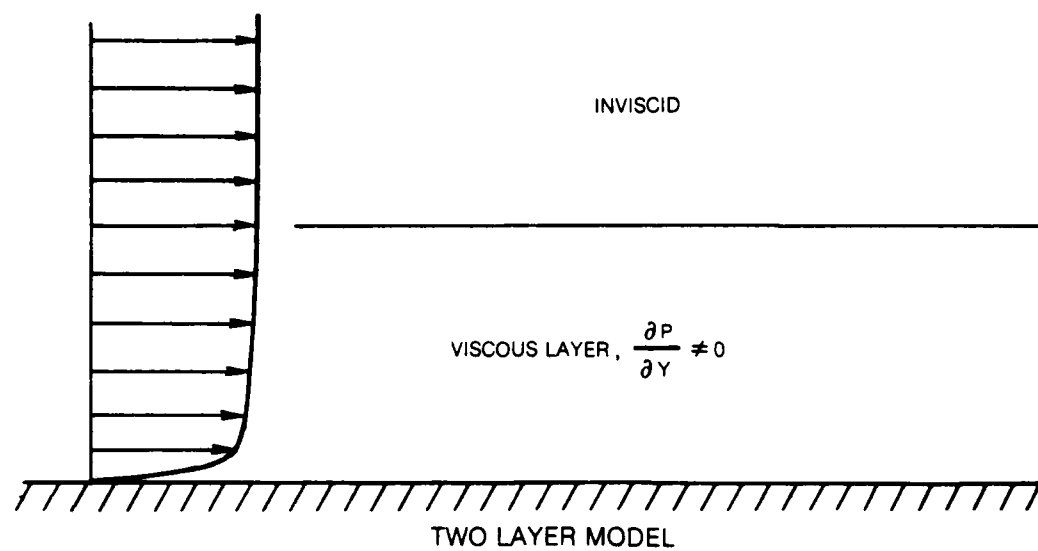


Fig. 2 Viscous — Inviscid interaction flow models

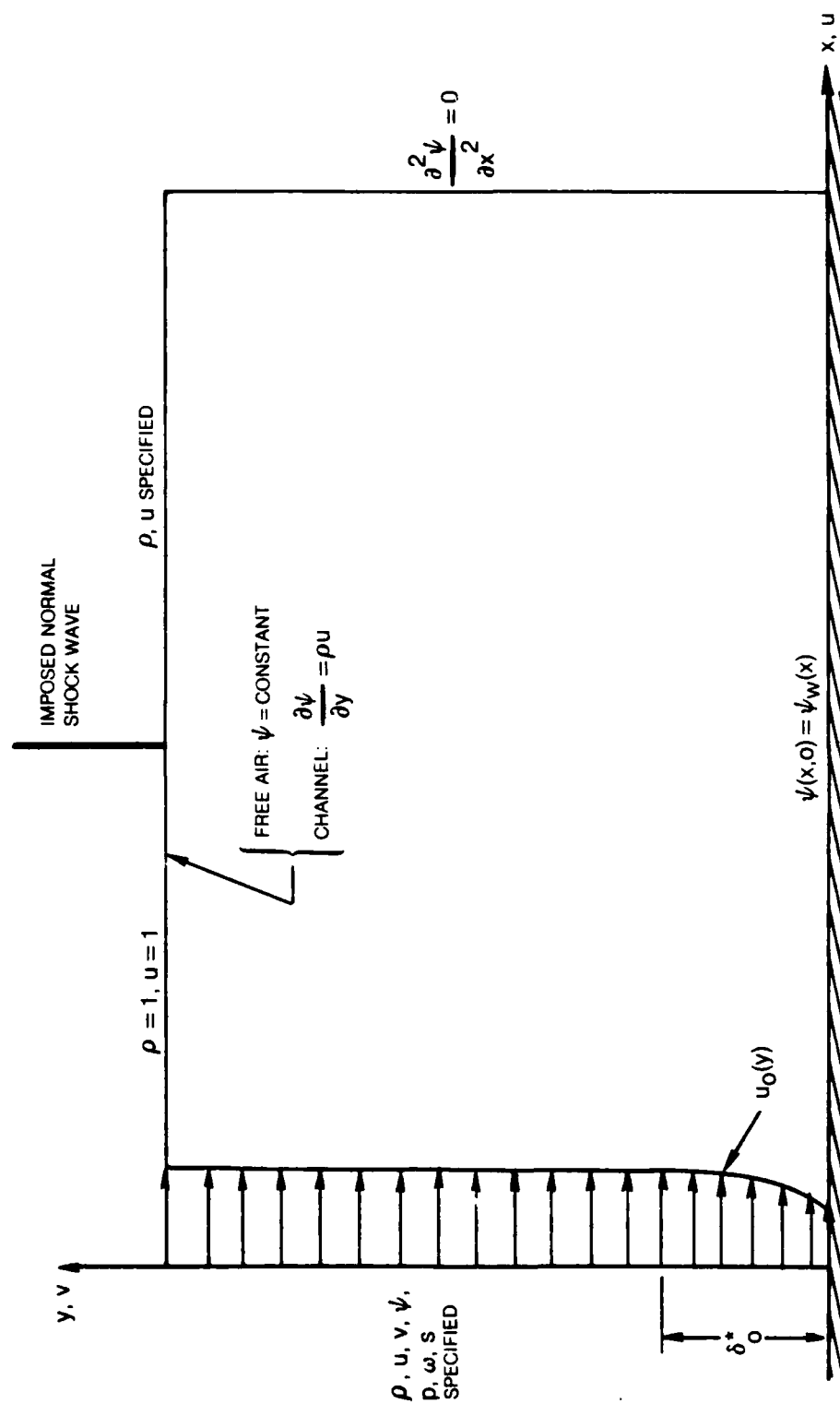


Fig. 3 Inviscid computational region and boundary conditions

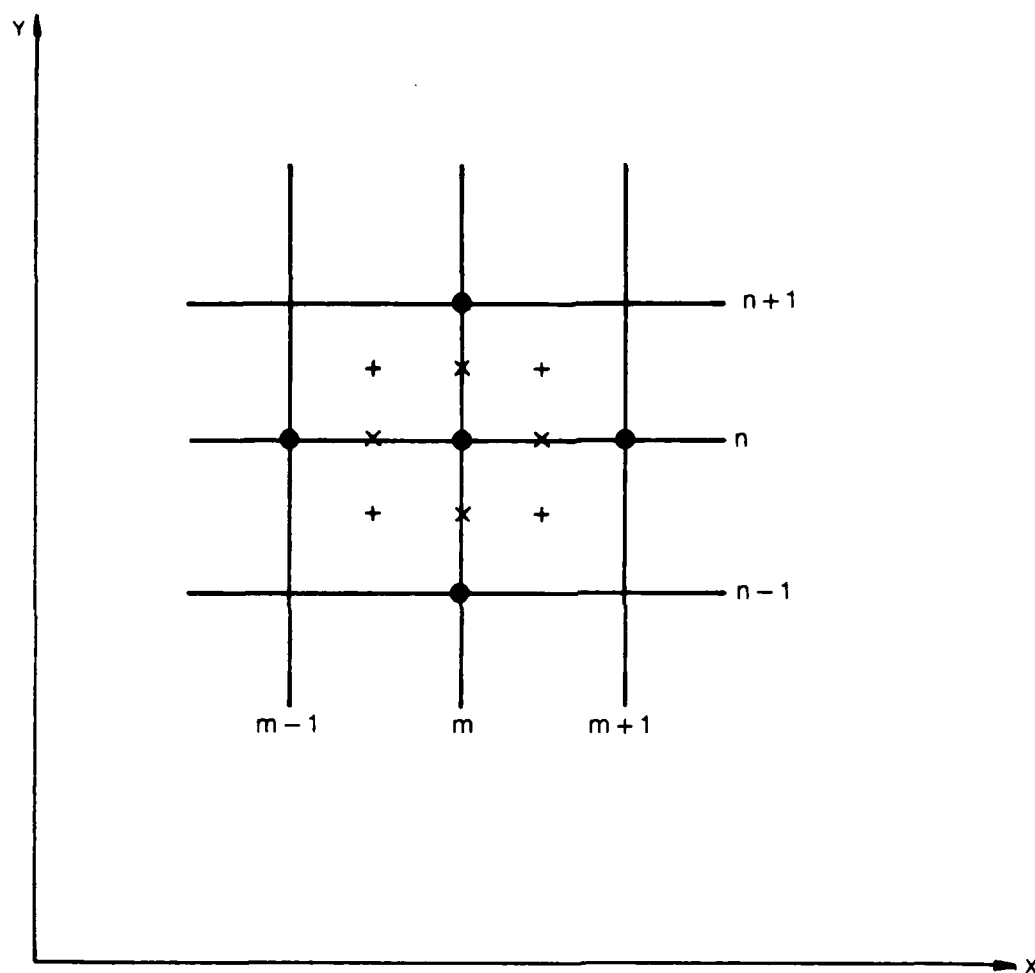


Fig. 4 Computational molecule in inviscid analysis

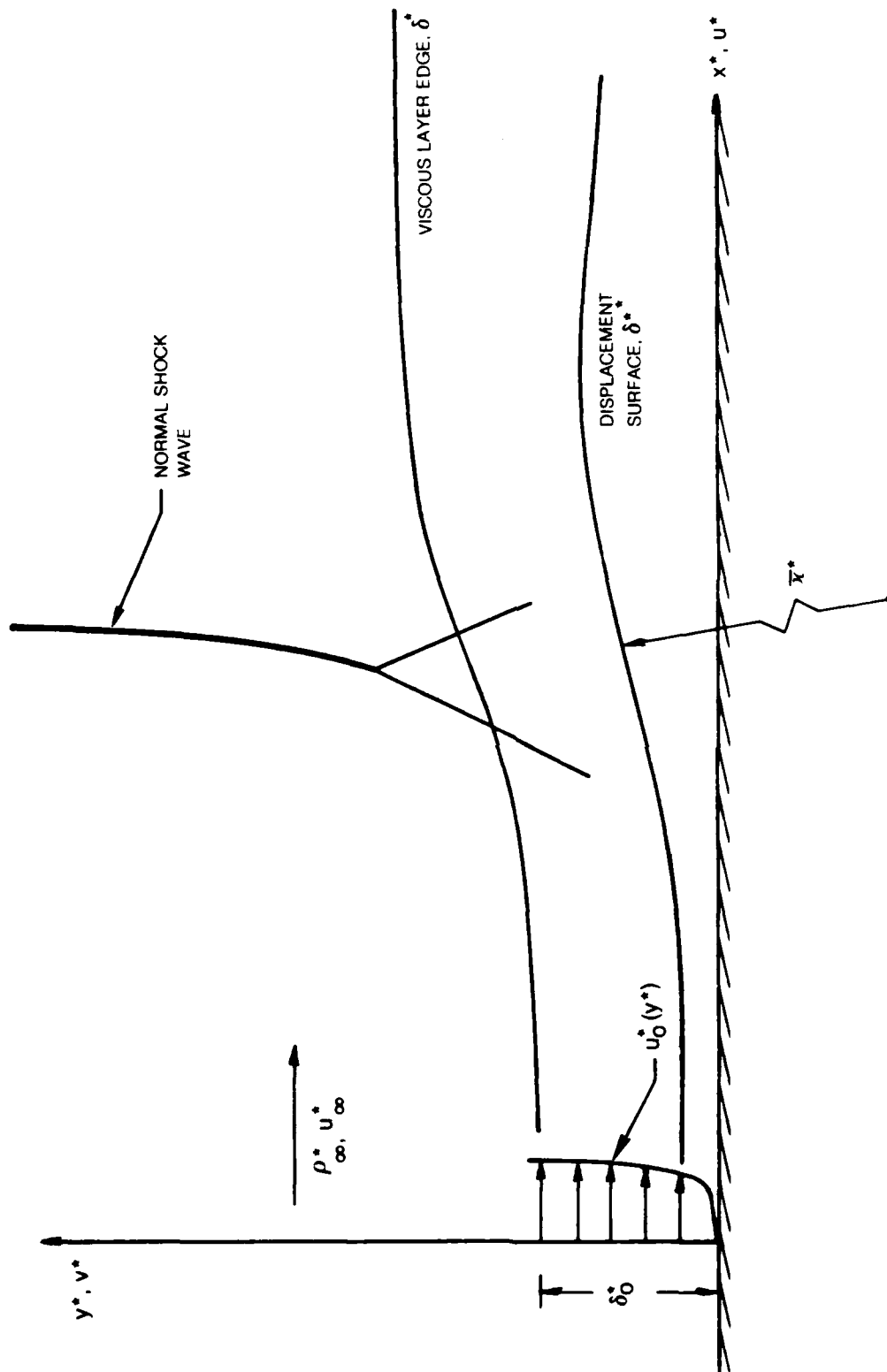


Fig. 5 Nomenclature for viscous flow analysis
(asterisk denotes dimensional quantity)

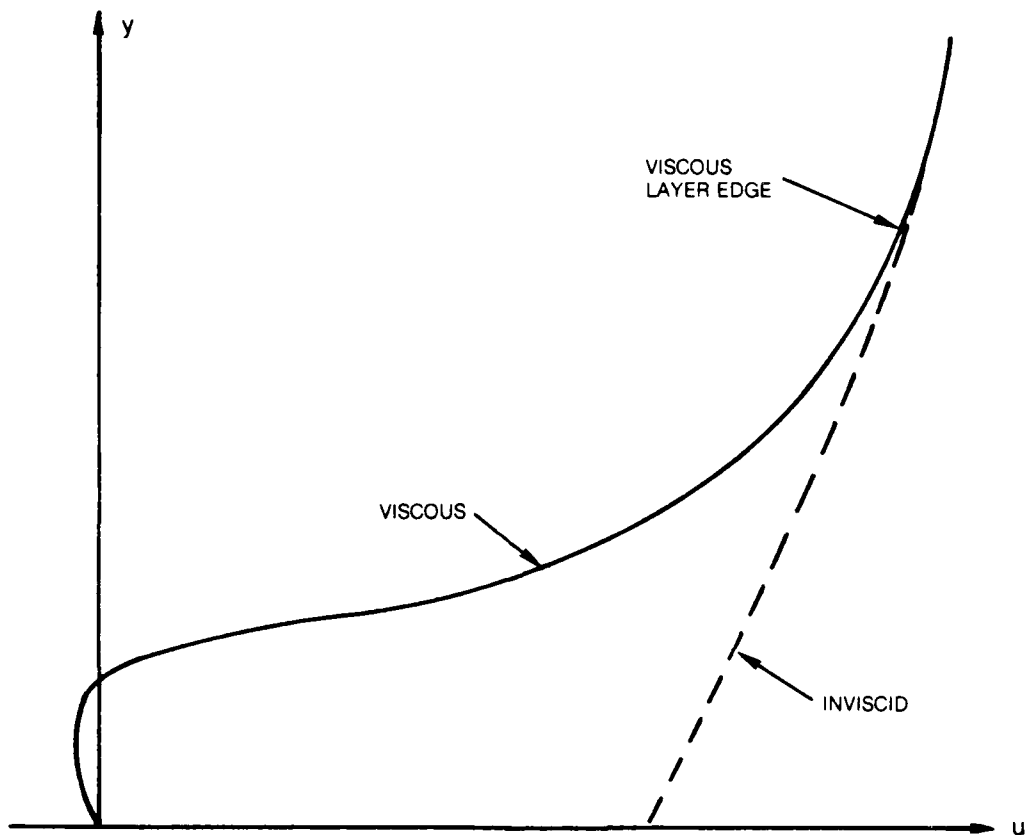


Fig. 6 Viscous-inviscid matching of velocity profile

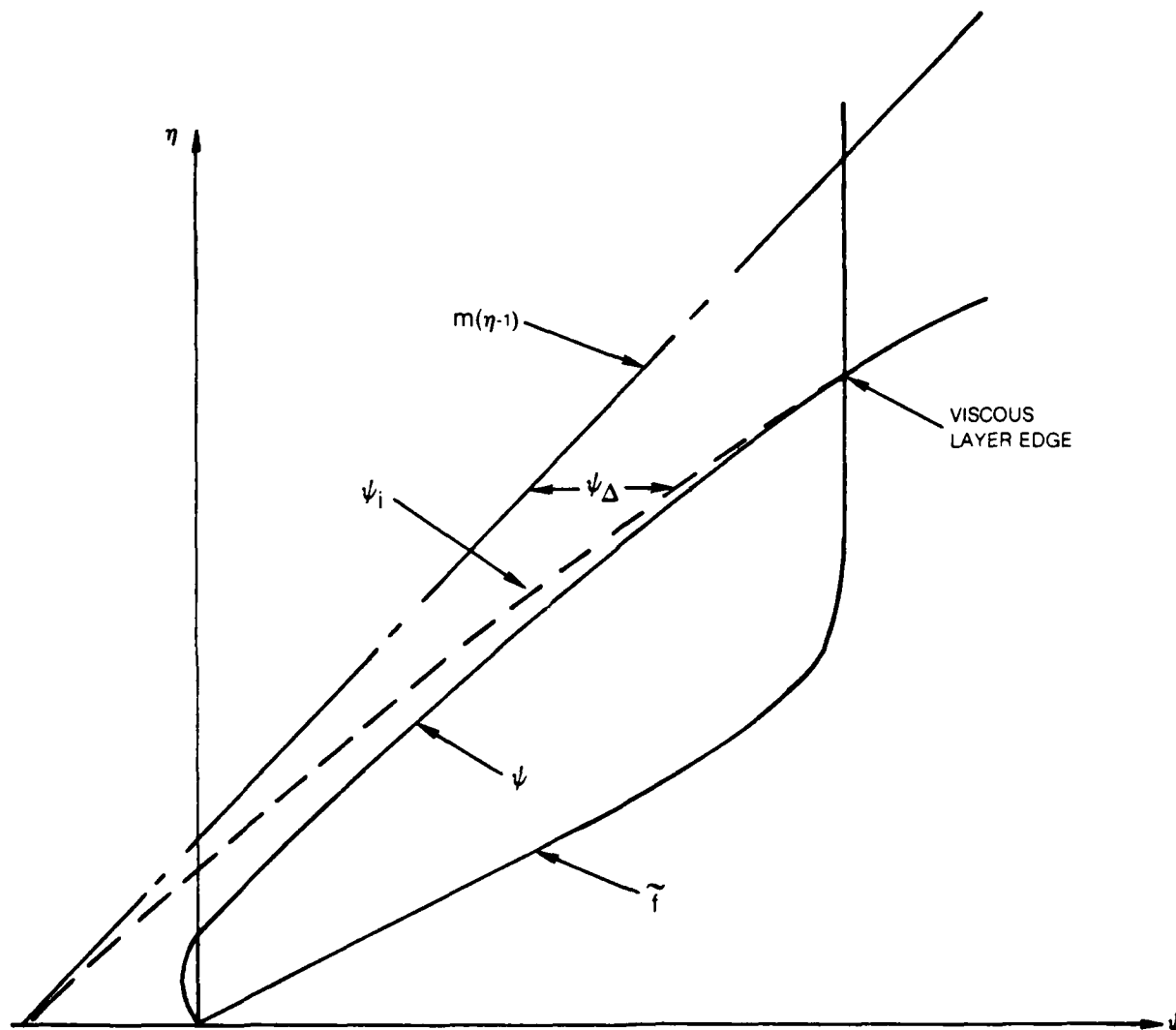


Fig. 7 Viscous and inviscid stream functions in viscous region

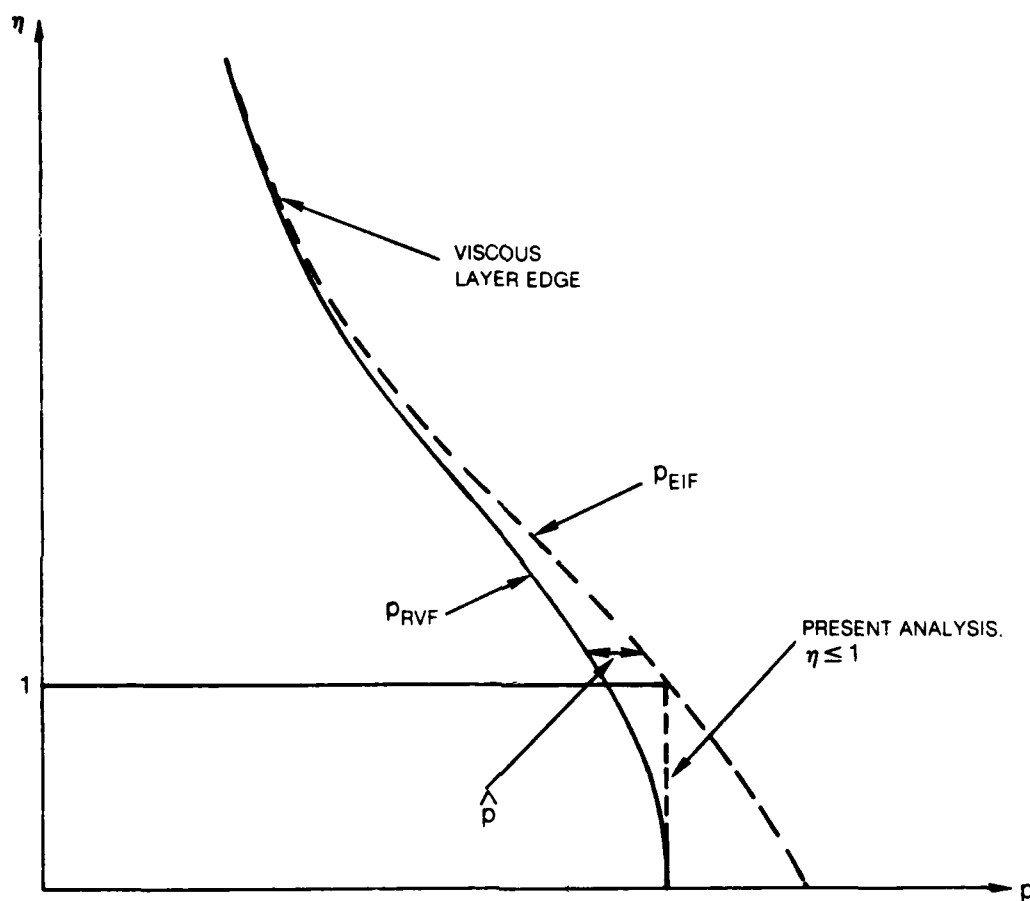


Fig. 8 Pressure distributions across the viscous region

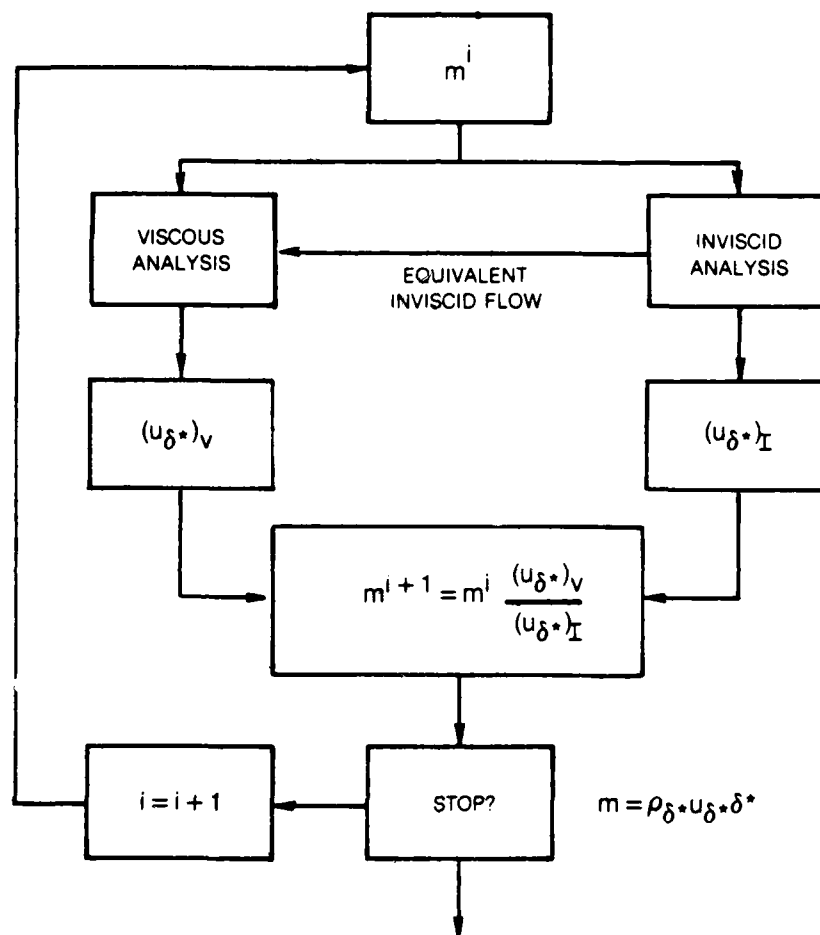


Fig. 9 Viscous-Inviscid global iteration technique

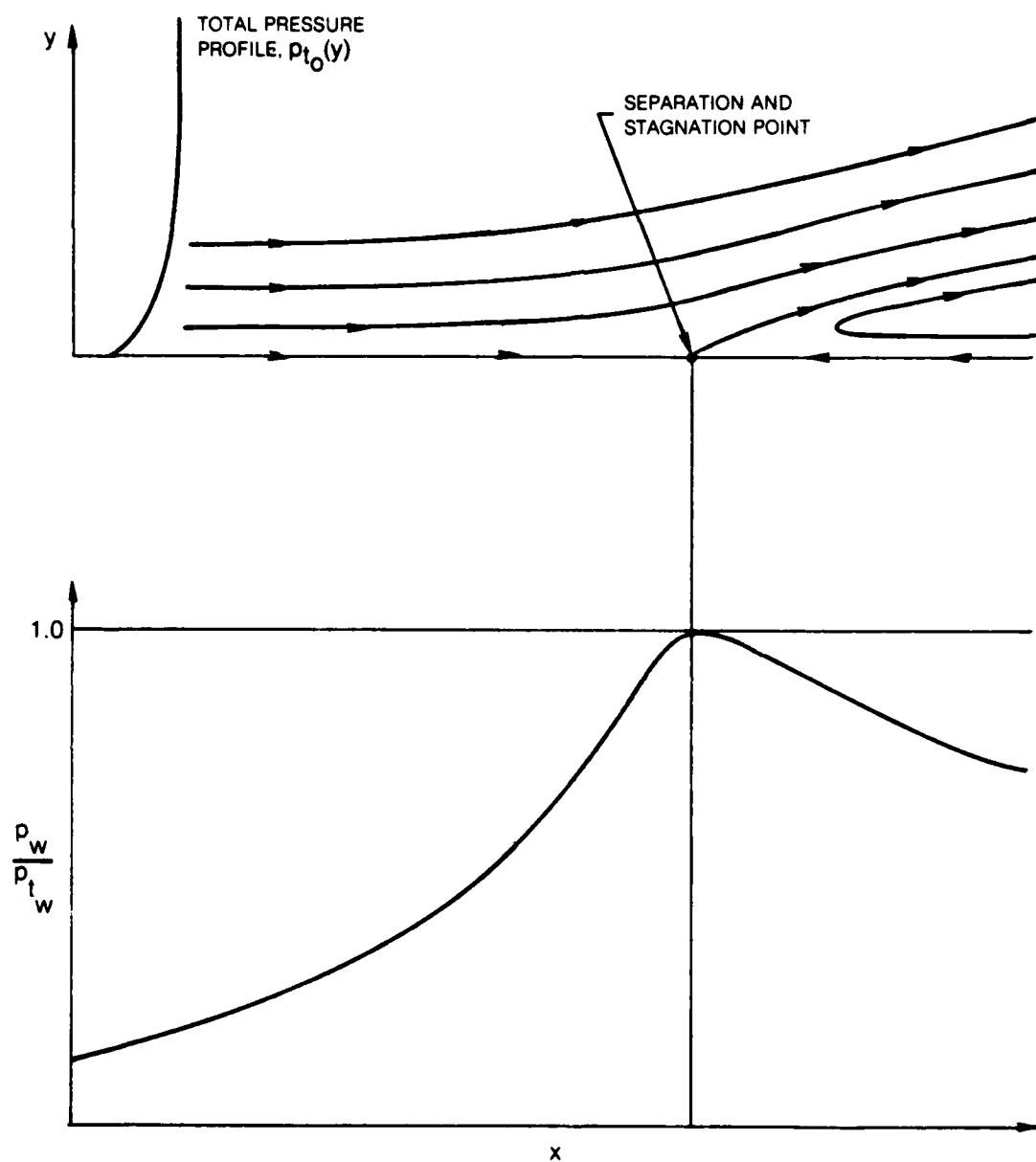
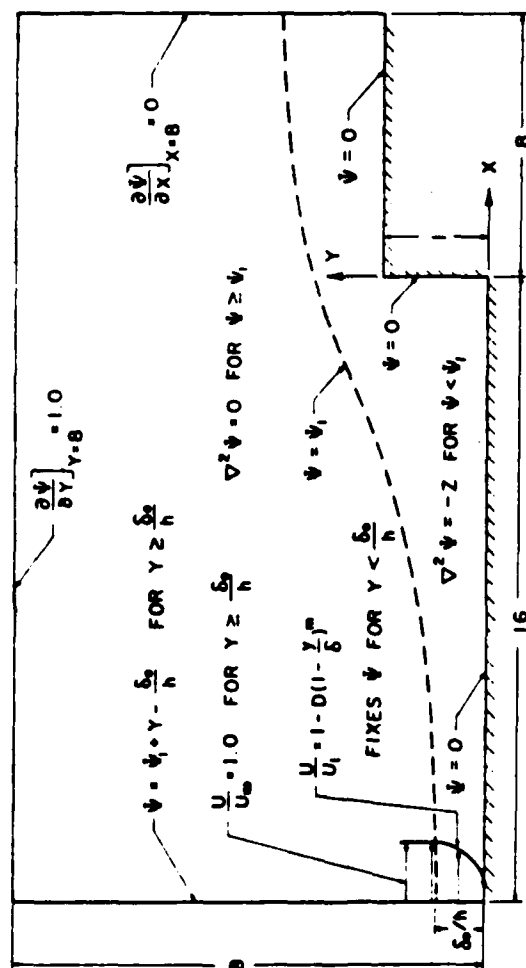
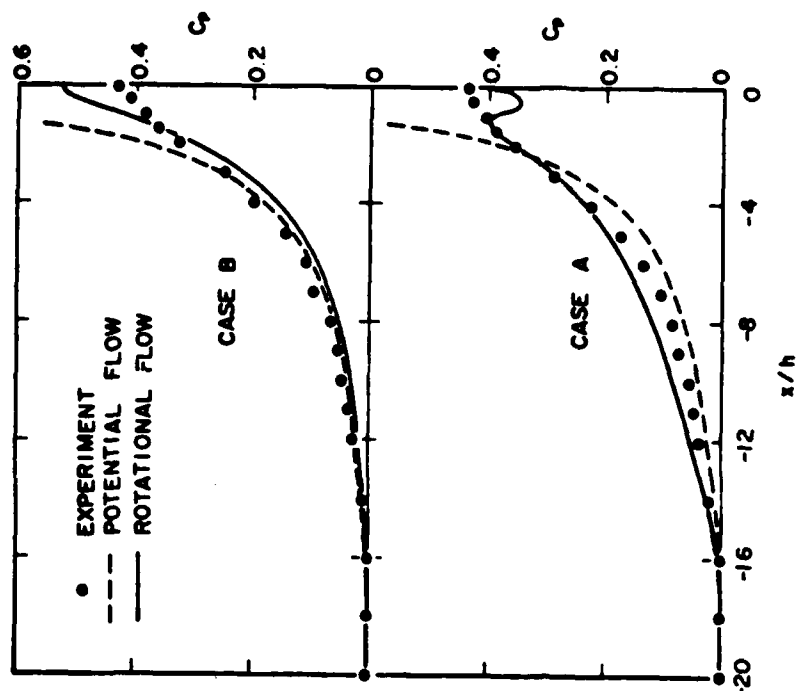


Fig. 10 Wall pressure distribution and streamline pattern in inviscid separated flow



Rotational flow field model



Wall pressure distribution ahead of the step

Fig. 11 Taulbee and Robertson analysis of rotational inviscid flow over a step

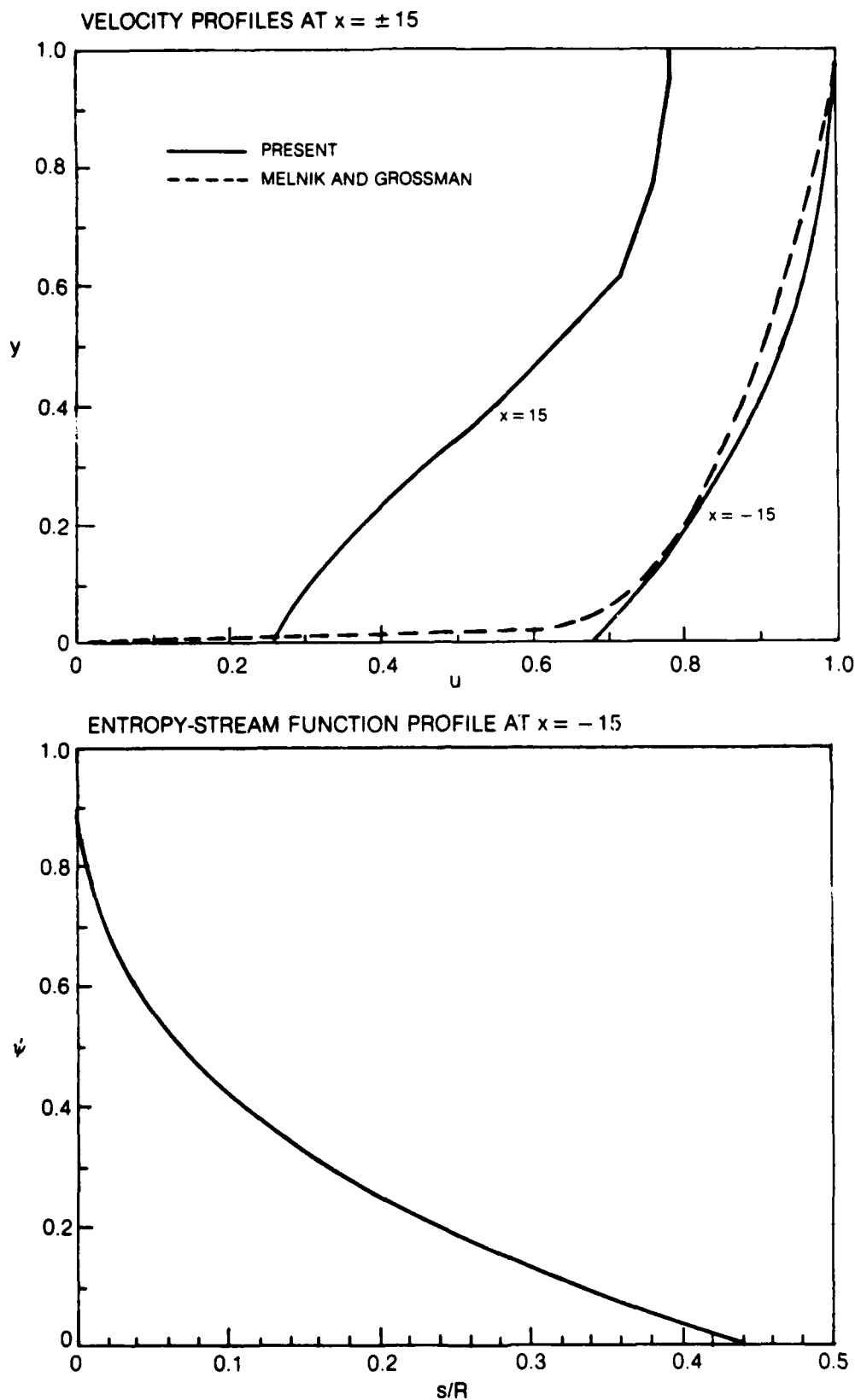


Fig. 12 Upstream profiles for inviscid rotational flow analysis of normal shock-wave, boundary-layer interaction at $M_\infty = 1.12$

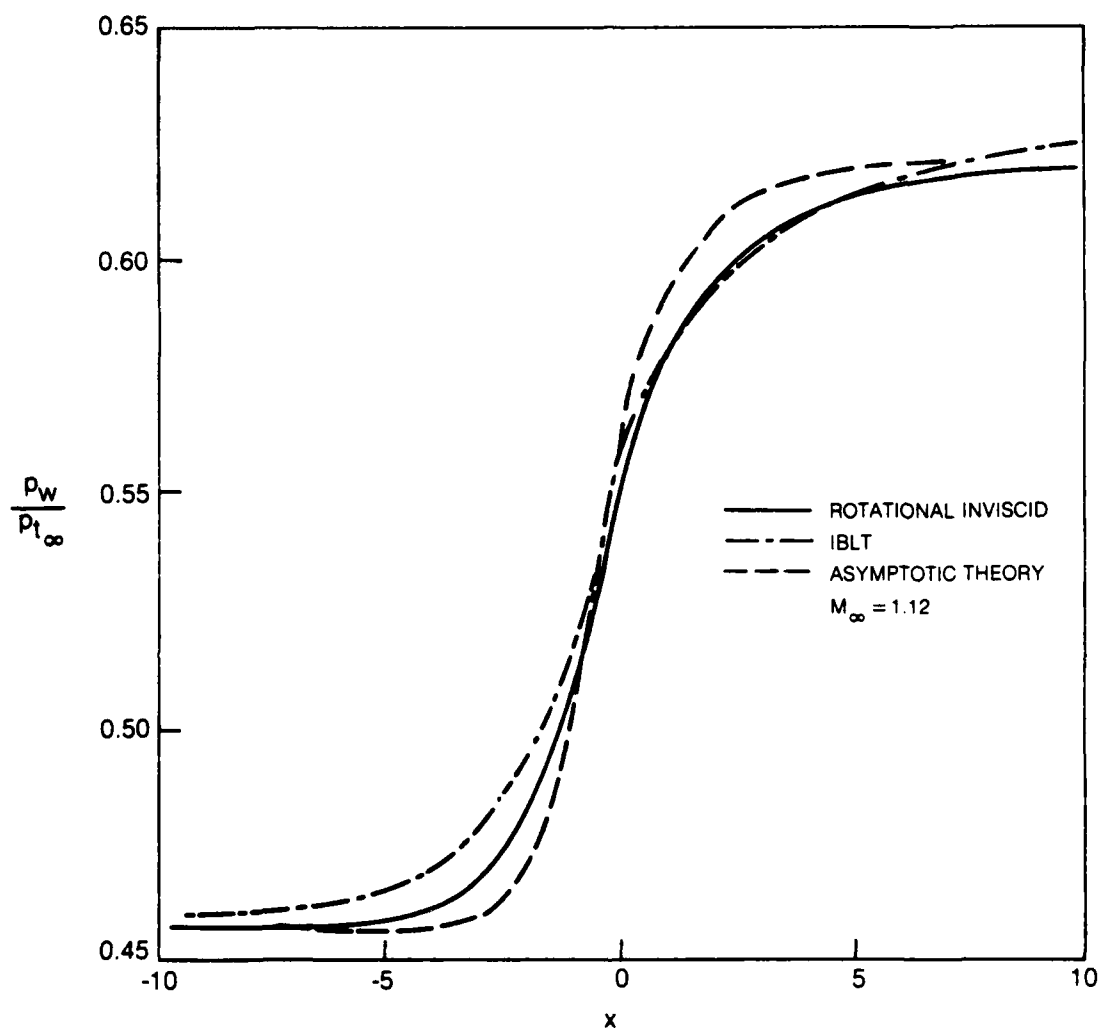


Fig. 13 Comparison of wall pressure from present rotational inviscid and interacting boundary layer theory (IBLT) with asymptotic theory of Melnik and Grossman

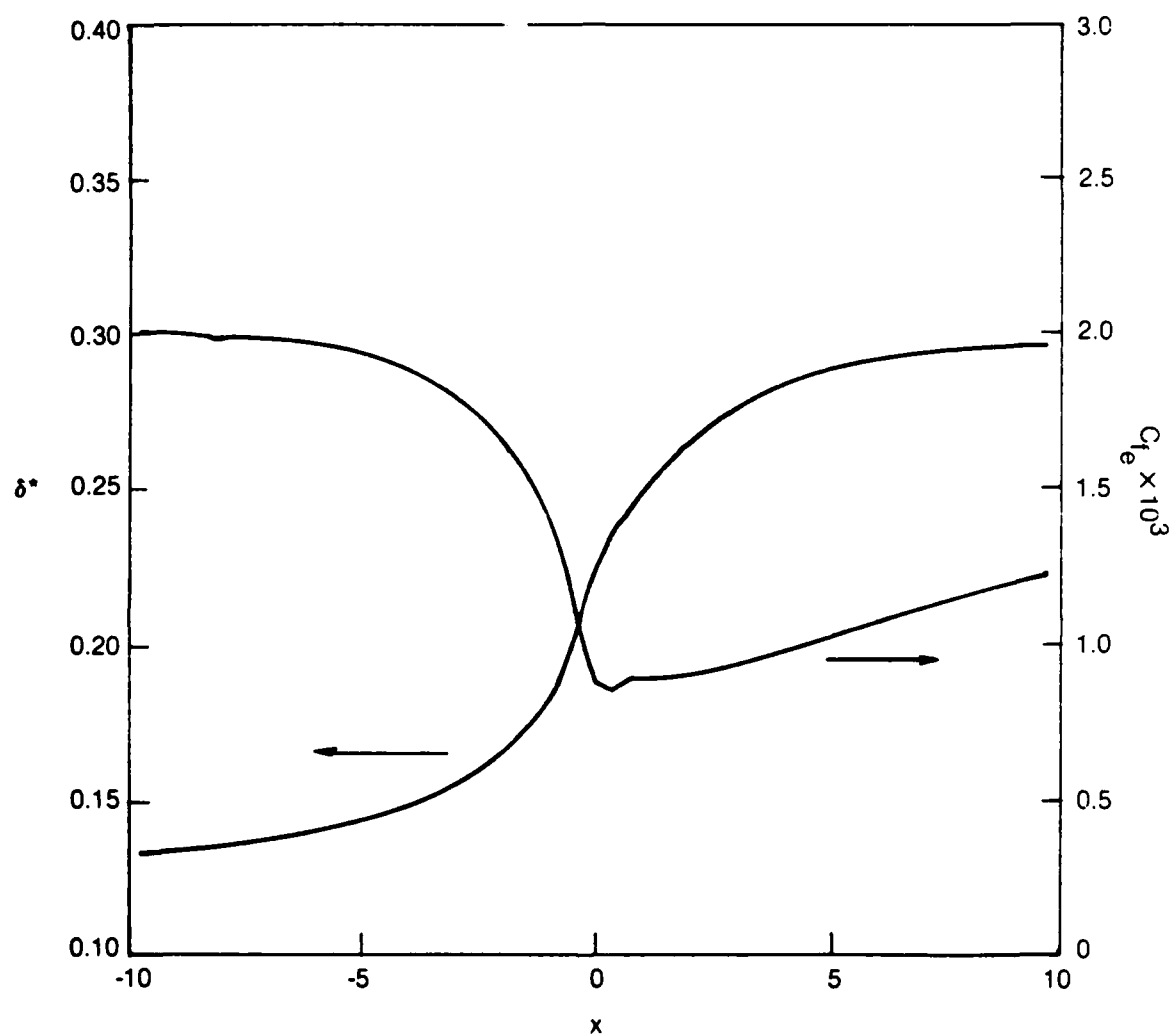


Fig. 14 Displacement thickness and skin friction computed from IBLT for $M_\infty = 1.12$

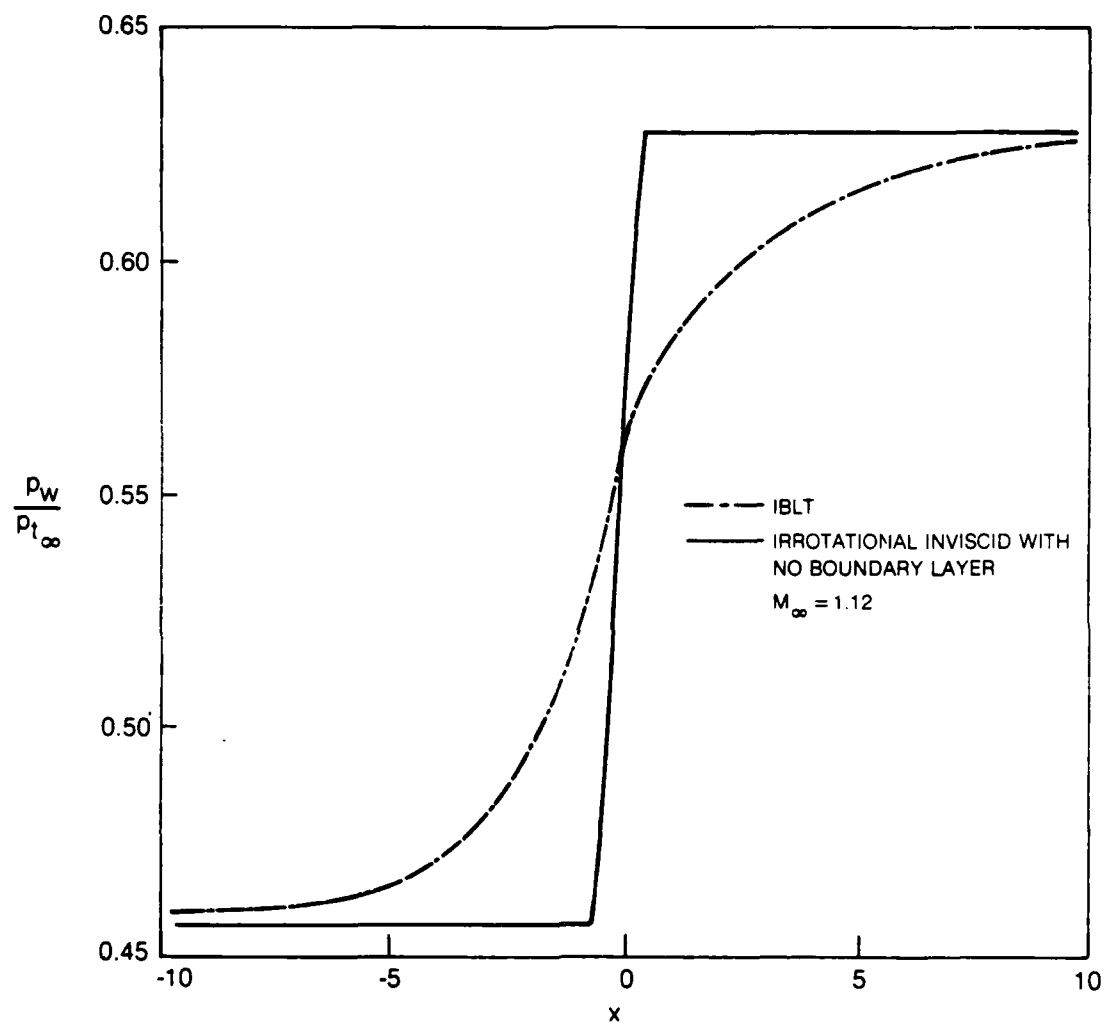


Fig. 15 Comparison of shock smearing due to artificial viscosity and boundary layer

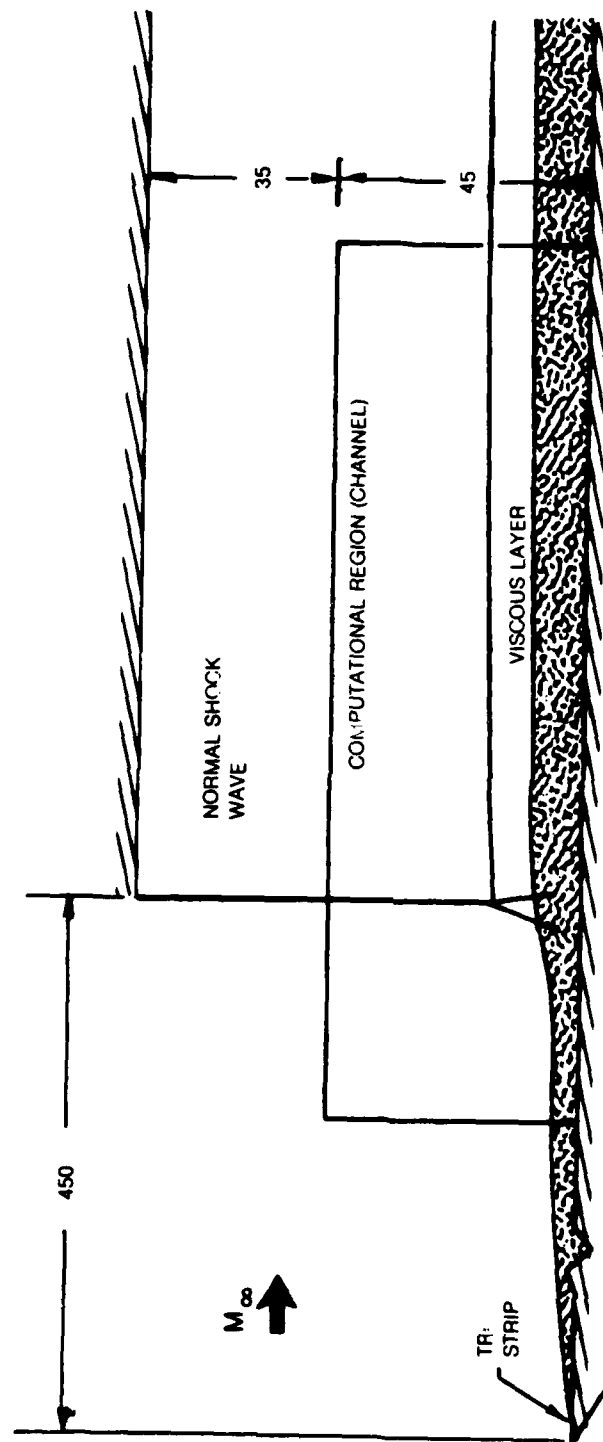


Fig. 16 Kool experimental configuration and present computational region
(all dimensions are in millimeters)

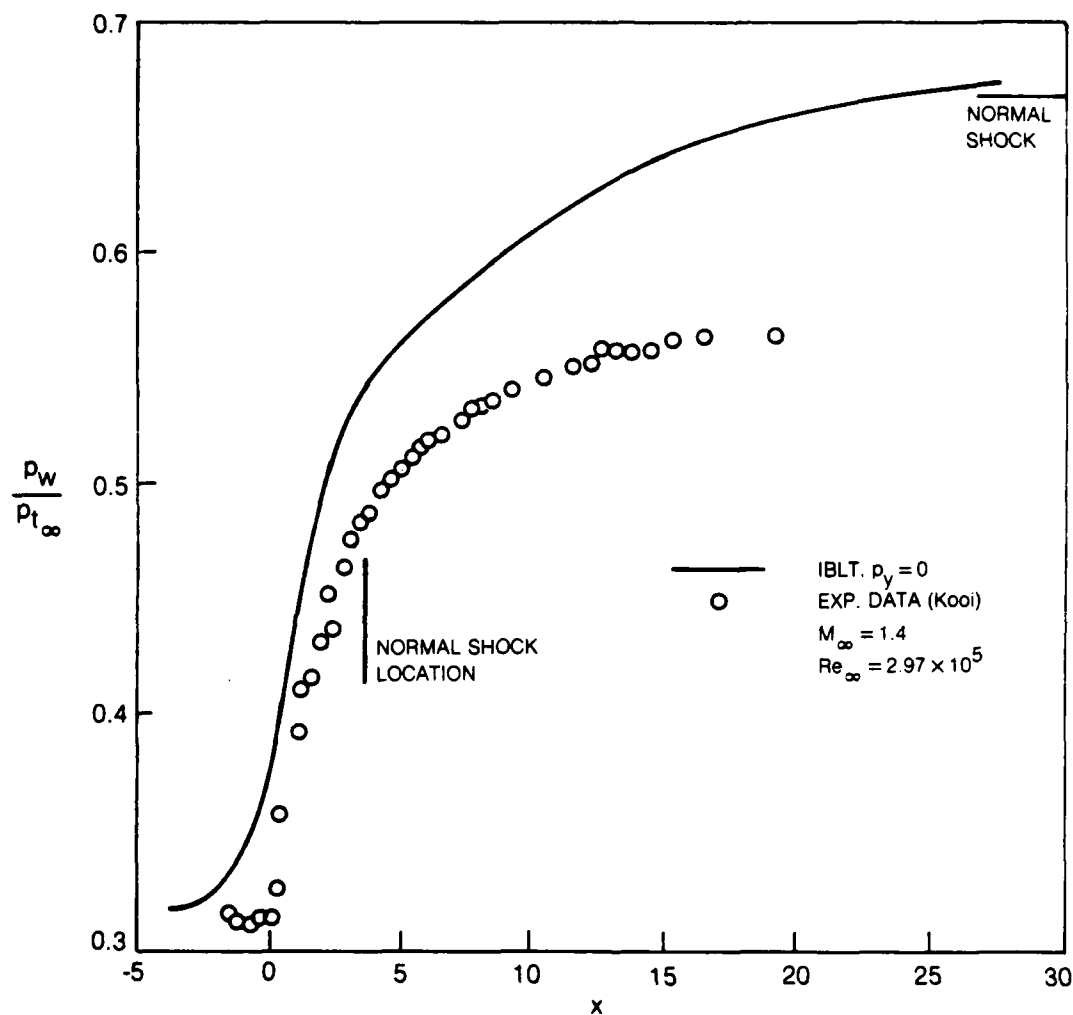


Fig. 17 Free air IBLT calculation of normal shock-wave, boundary-layer interaction
a) Wall pressure

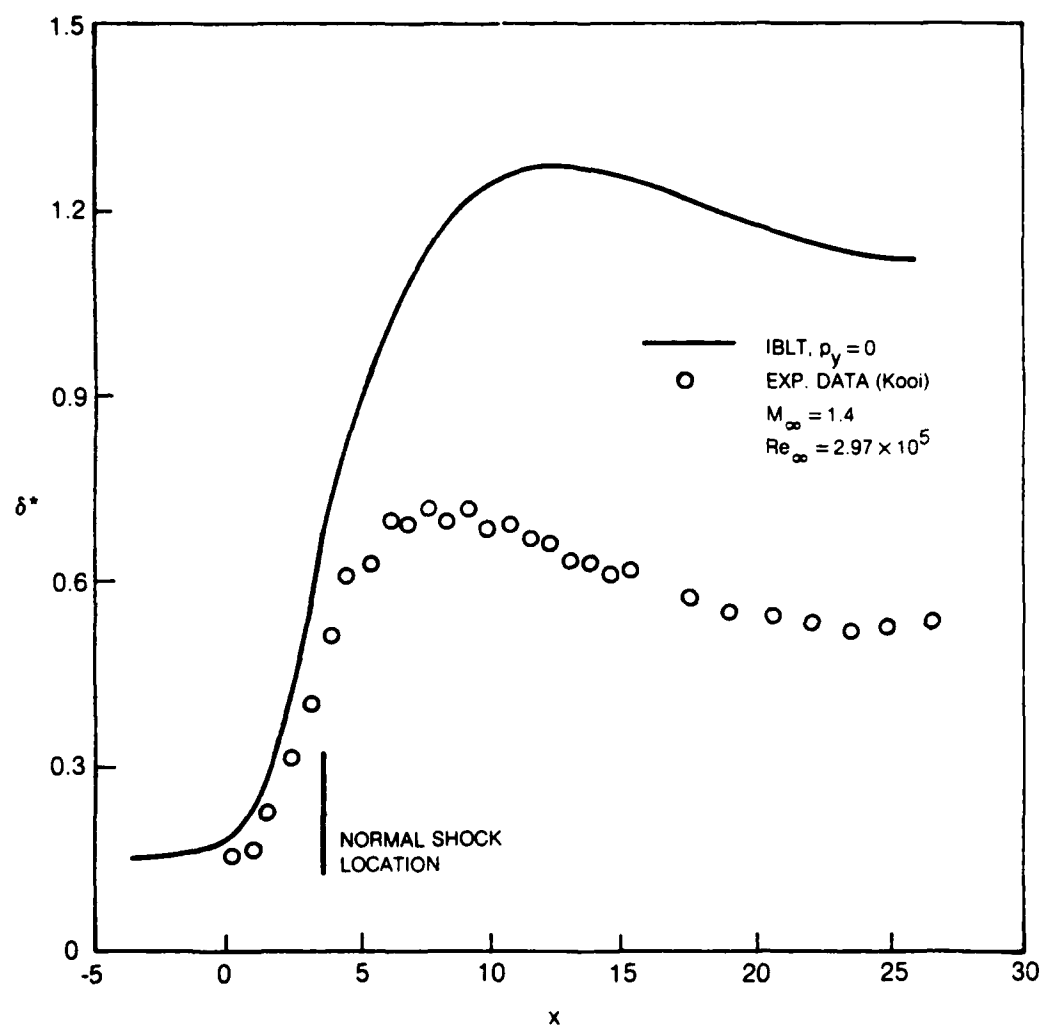


Fig. 17 Free air IBLT calculation of normal shock-wave, boundary-layer interaction
b) Displacement thickness

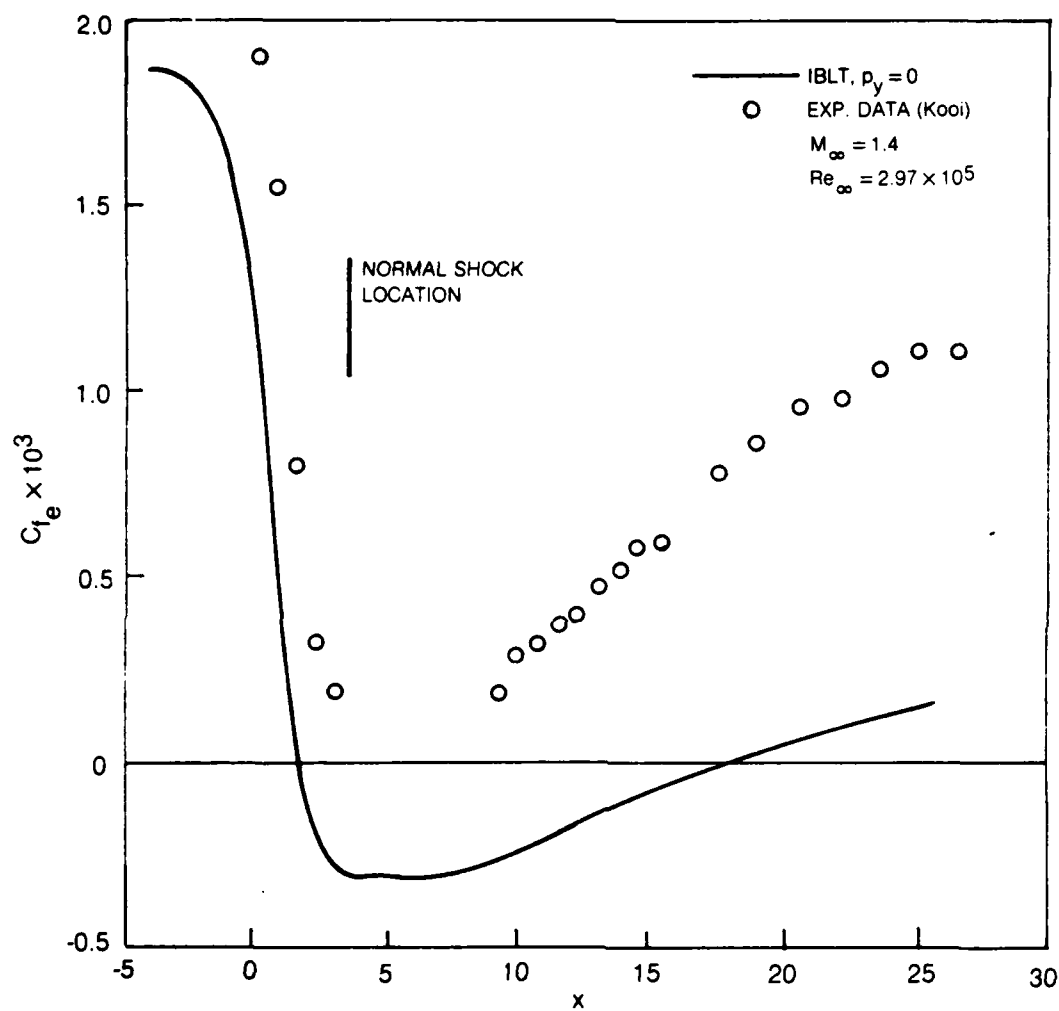
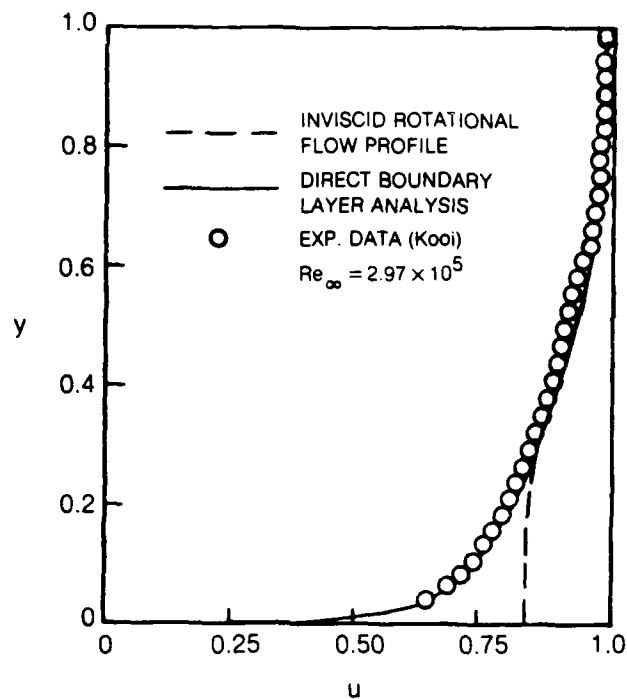


Fig. 17 Free air IBLT calculation of normal shock-wave, boundary-layer interaction
c) Skin friction

VELOCITY PROFILE



ENTROPY-STREAM FUNCTION PROFILE

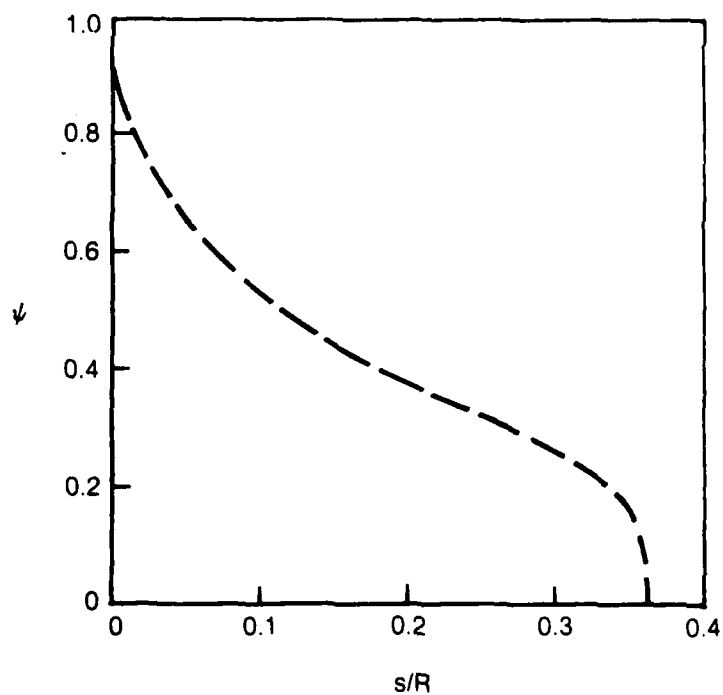


Fig. 18 Upstream profiles for inviscid rotational flow analysis of normal shock-wave, boundary-layer interaction at $M_{\infty} = 1.4$

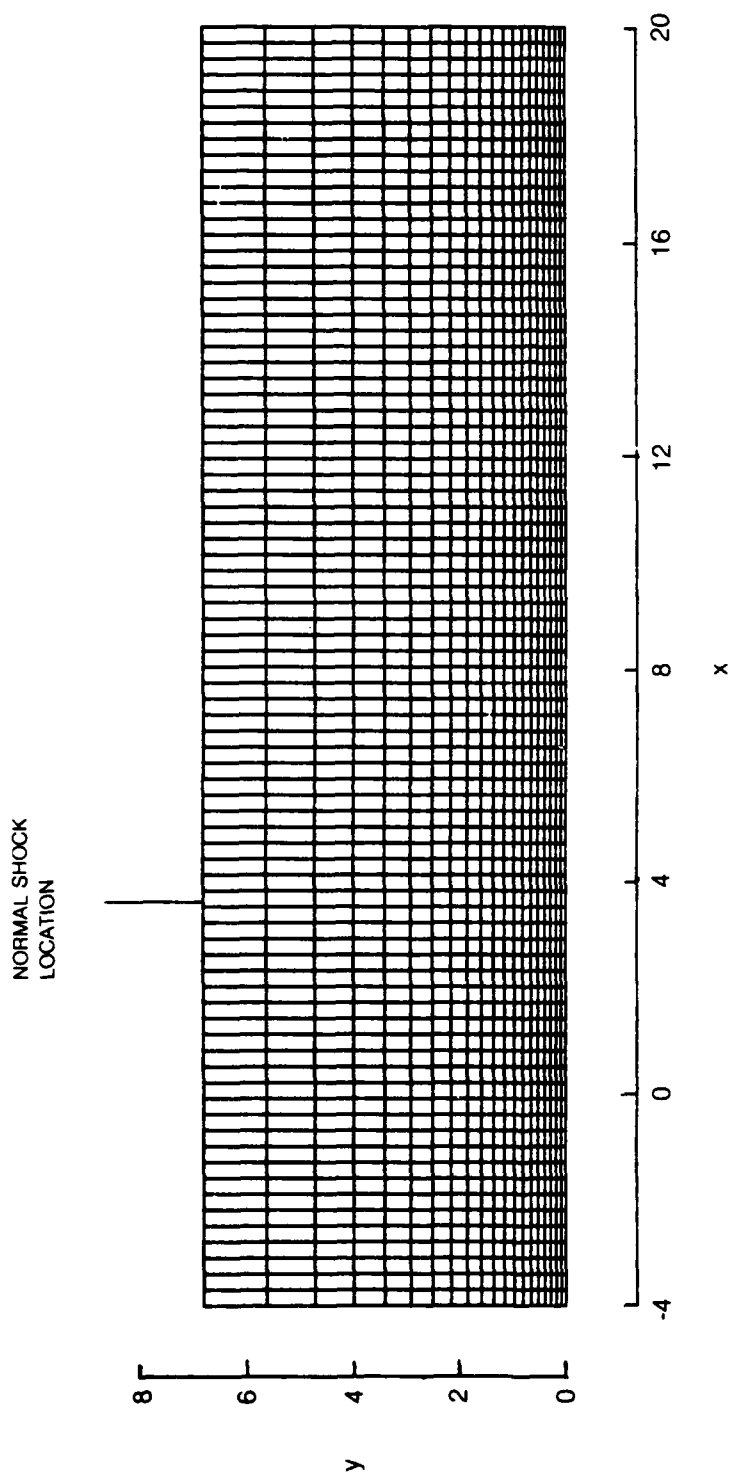


Fig. 19 Inviscid computational mesh for $M_{\infty} = 1.4$ channel calculation of Kool normal shock-wave, boundary-layer interaction

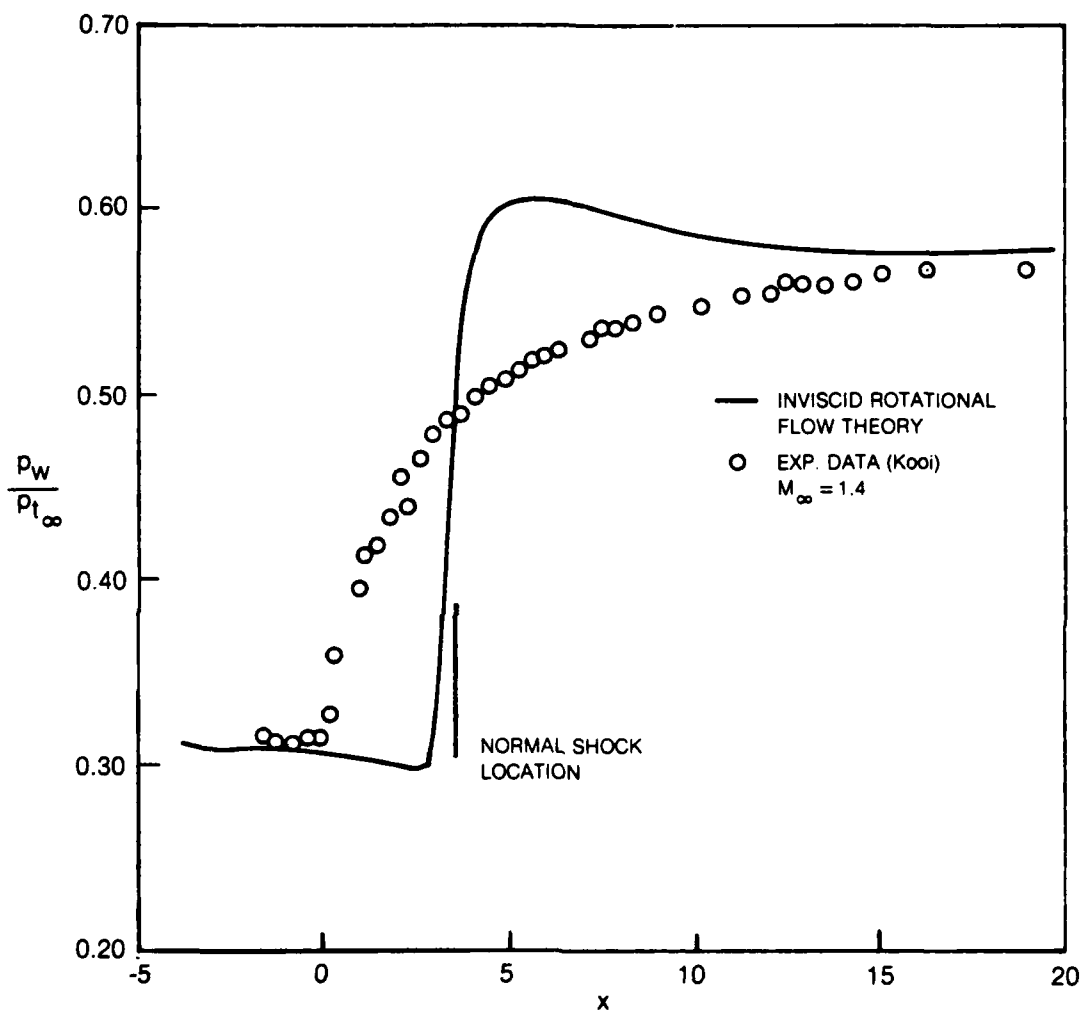


Fig. 20 Comparison of computed and experimental wall pressure distributions

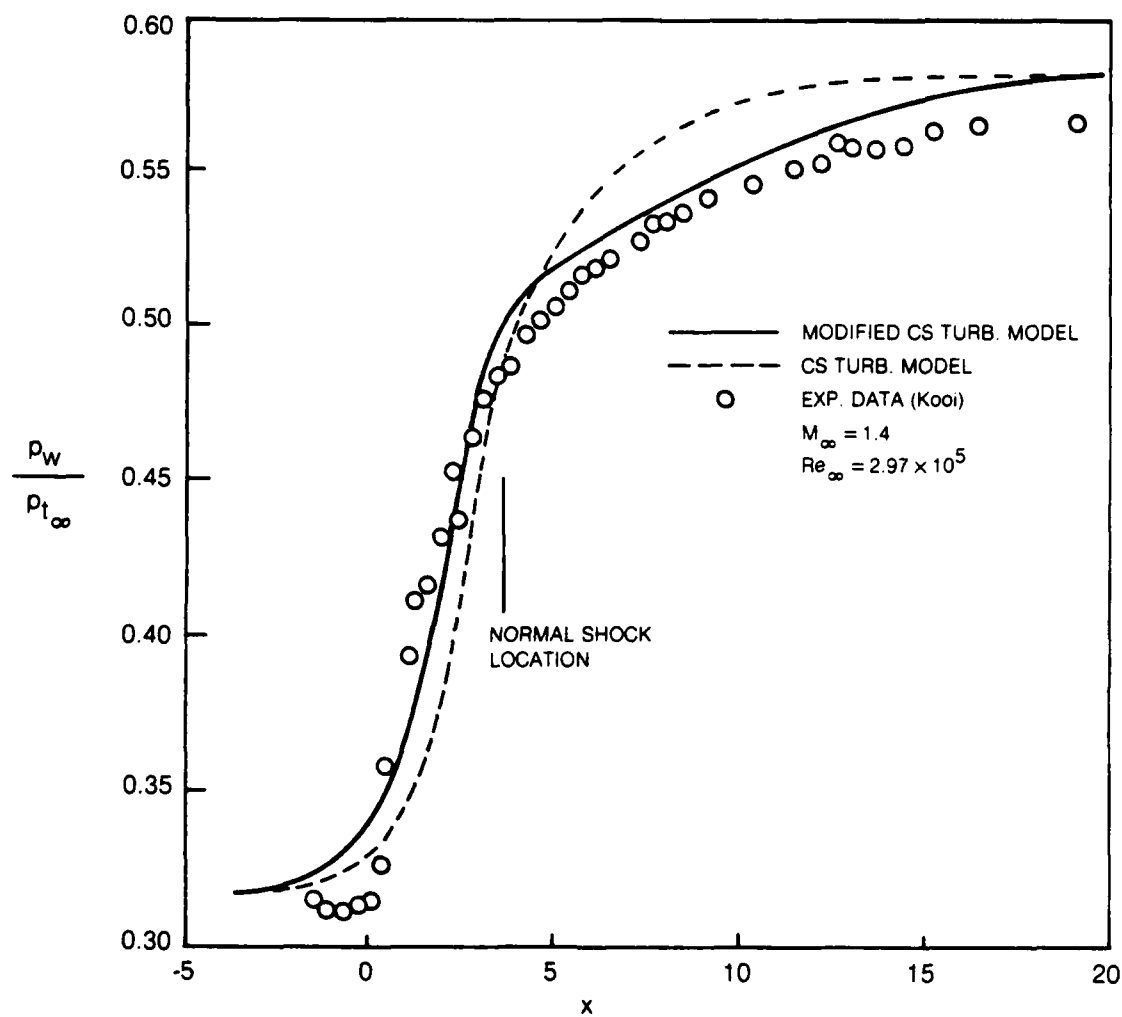


Fig. 21 Comparison of results from IBLT ($p_y \neq 0$) with experimental data for transonic normal shock-wave, boundary-layer interaction
a) Wall pressure

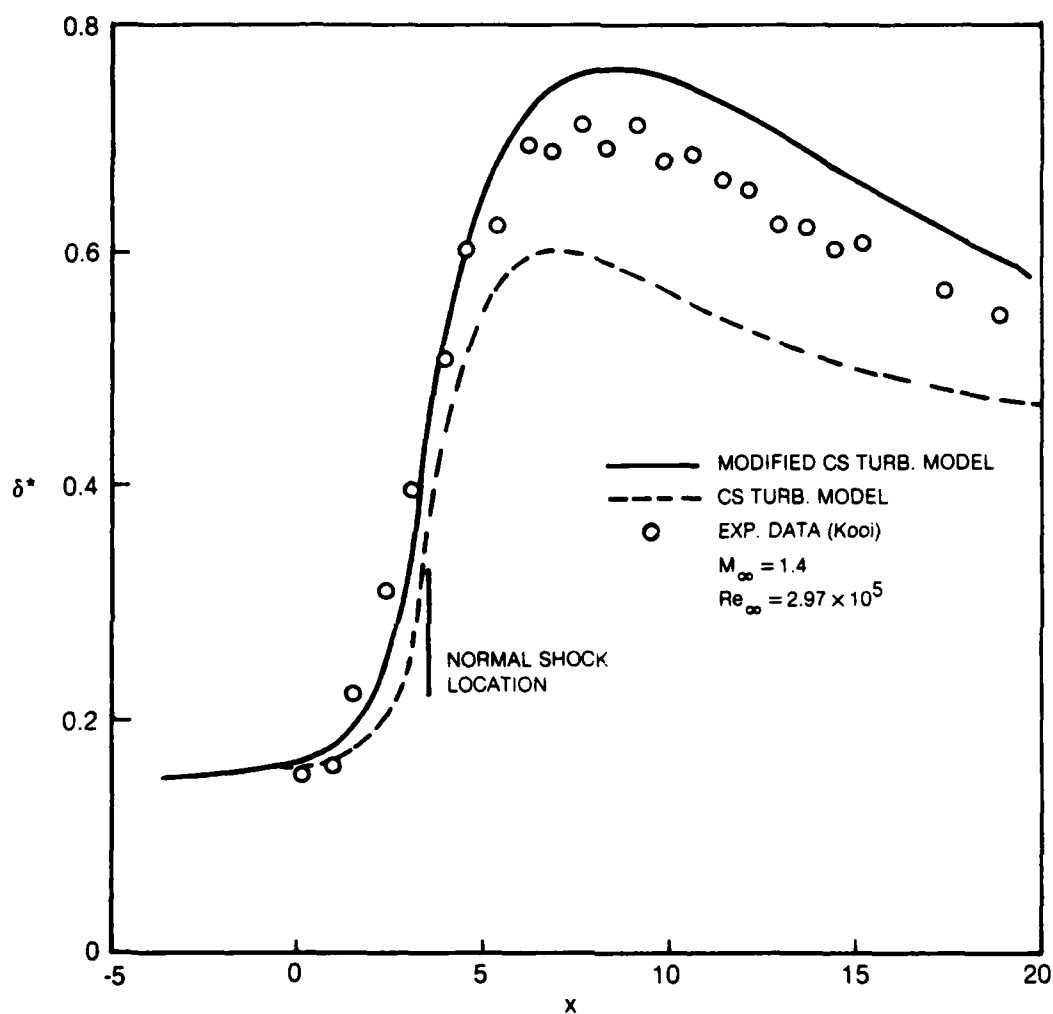


Fig. 21 Comparison of results from IBLT ($p_y \neq 0$) with experimental data for transonic normal shock-wave, boundary-layer interaction
b) Displacement thickness

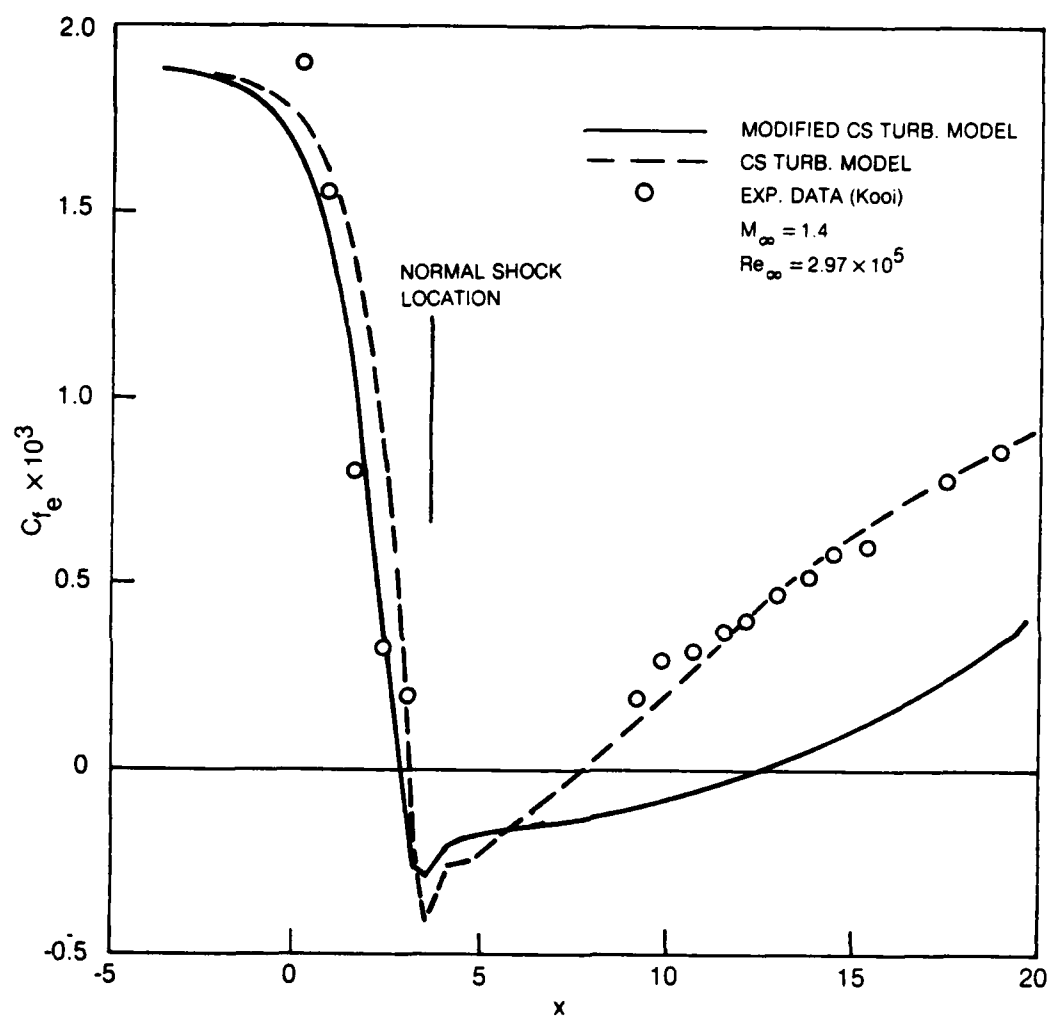


Fig. 21 Comparison of results from IBLT ($p_y \neq 0$) with experimental data for transonic normal shock-wave, boundary-layer interaction
c) Skin friction

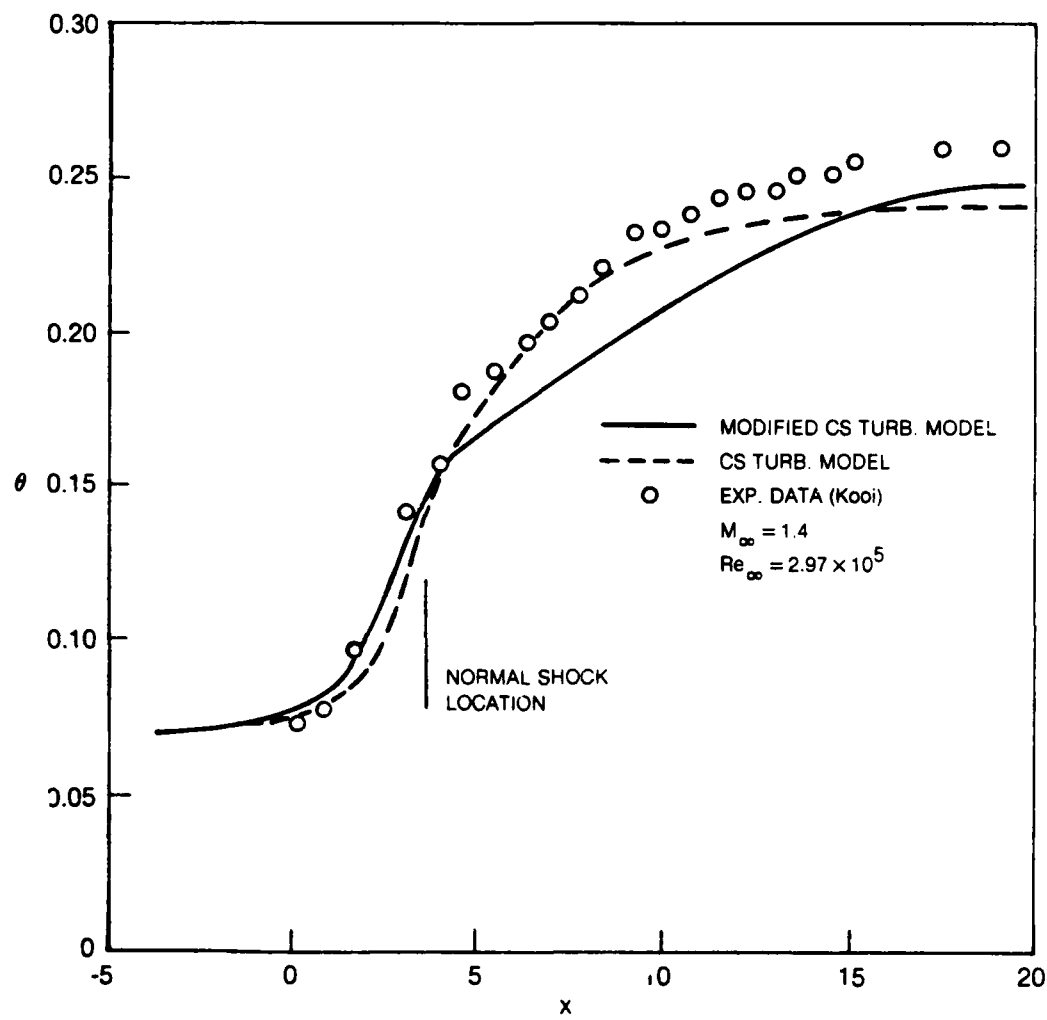


Fig. 21 Comparison of results from IBLT ($p_y \neq 0$) with experimental data for transonic normal shock-wave, boundary-layer interaction
d) Momentum thickness

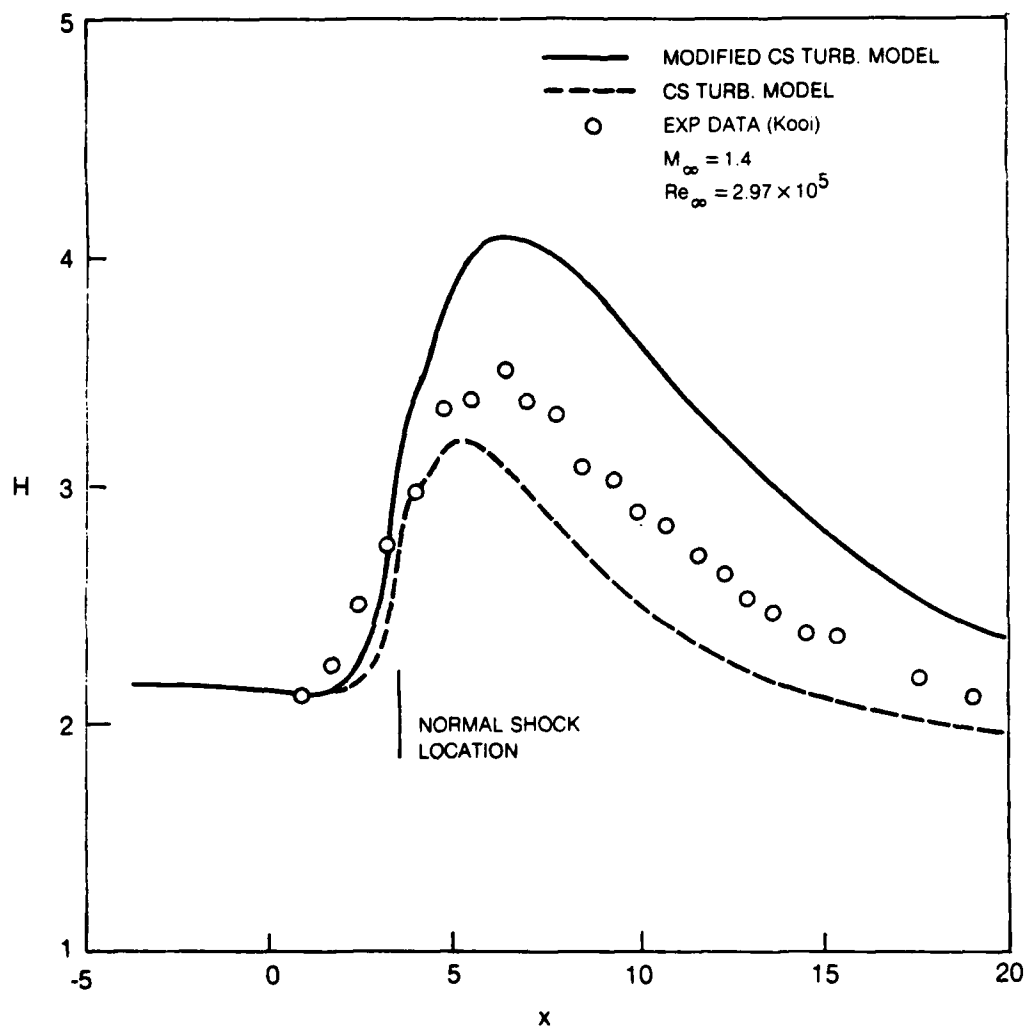


Fig. 21 Comparison of results from IBLT ($p_y \neq 0$) with experimental data for transonic normal shock-wave, boundary-layer interaction
e) Shape factor

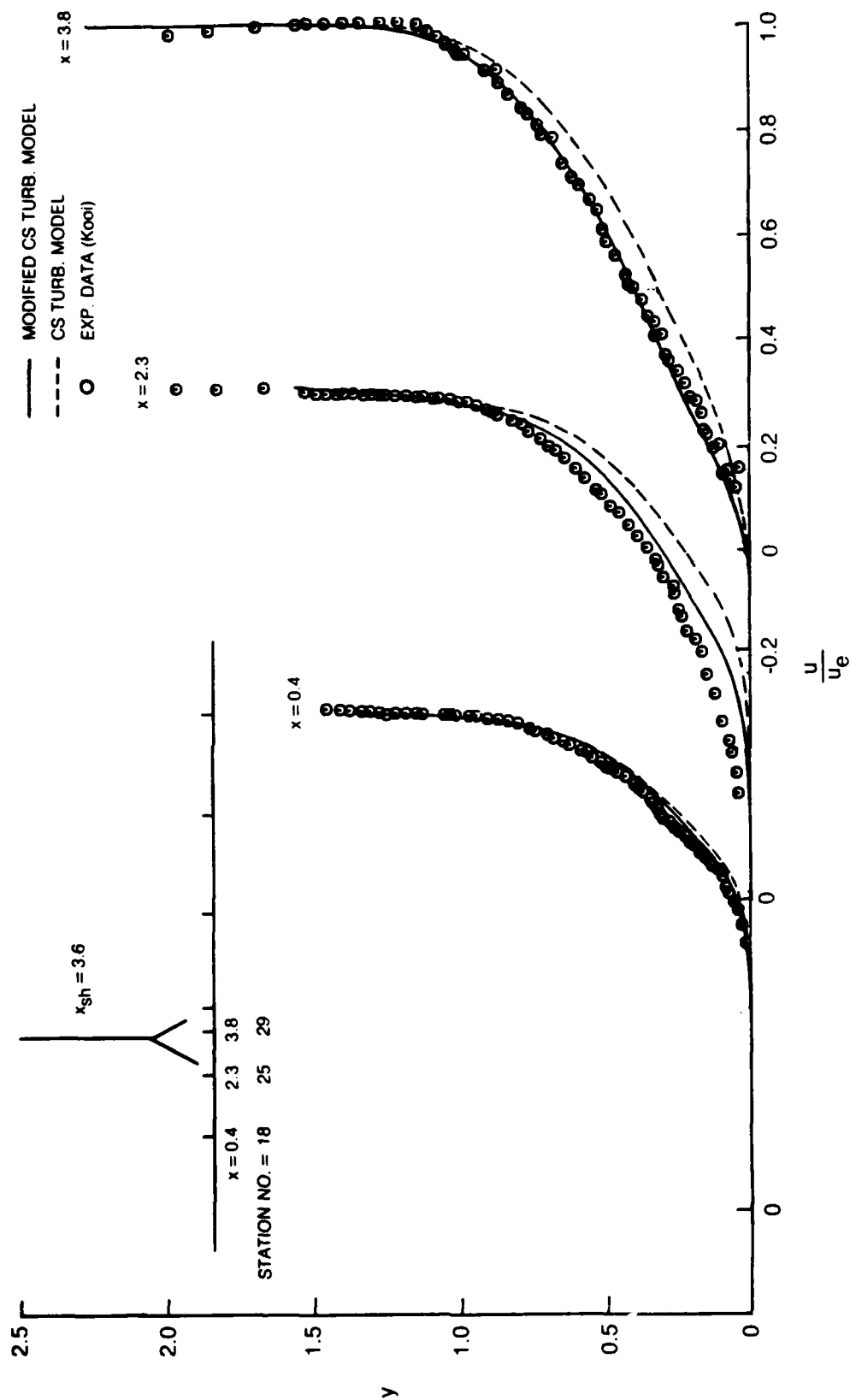
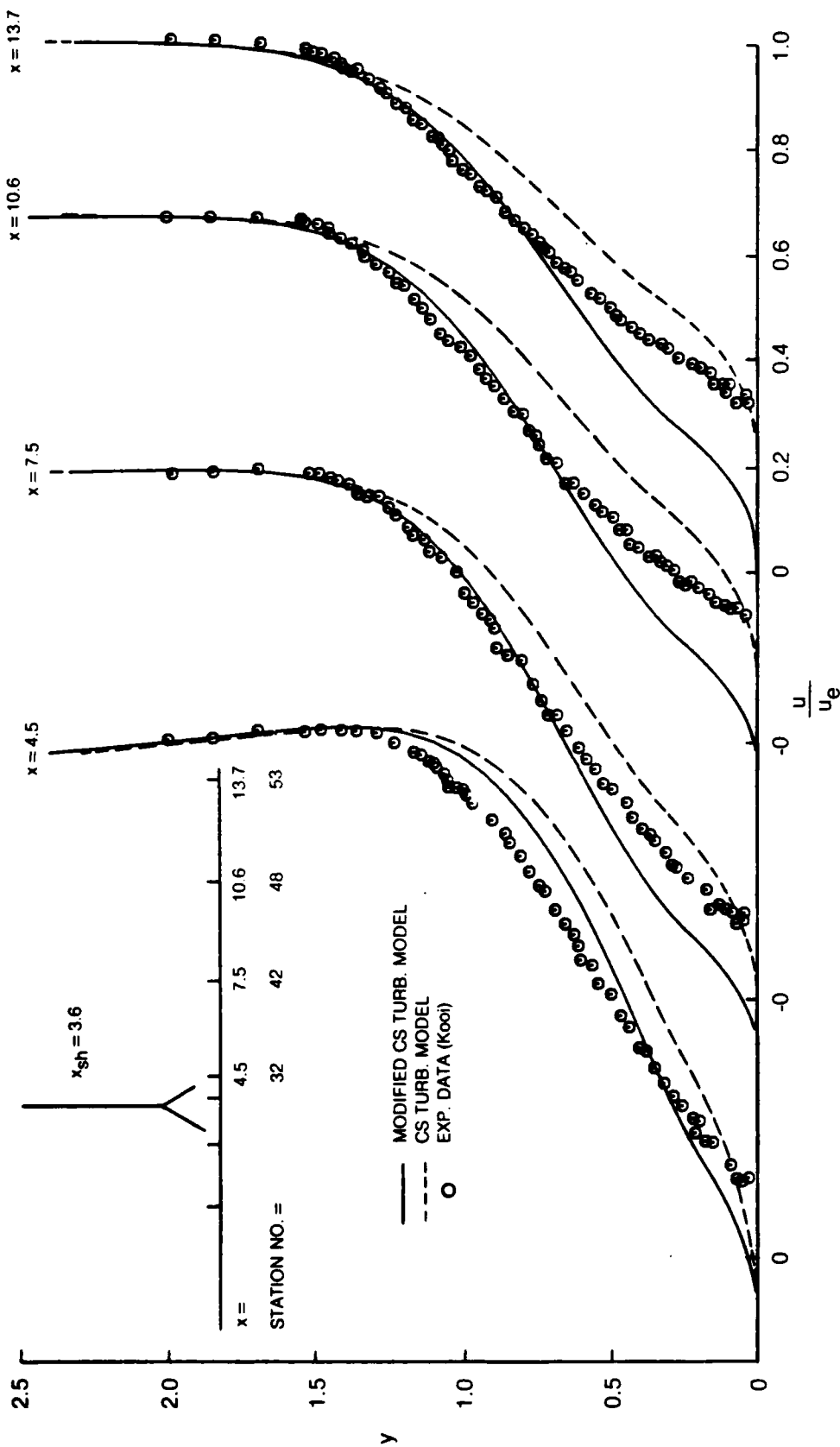


Fig. 22 Comparison of velocity profiles from IBLT ($p_y \neq 0$) with experimental data
for $M_\infty = 1.4$, $Re_\infty = 2.97 \times 10^5$
a) $x = 0.4$, 2.3 and 3.8



**Fig. 22 Comparison of velocity profiles from IBLT ($p_y \neq 0$) with experimental data for $M_\infty = 1.4$, $Re_\infty = 2.97 \times 10^5$
b) $x = 4.5, 7.5, 10.6$ and 13.7**

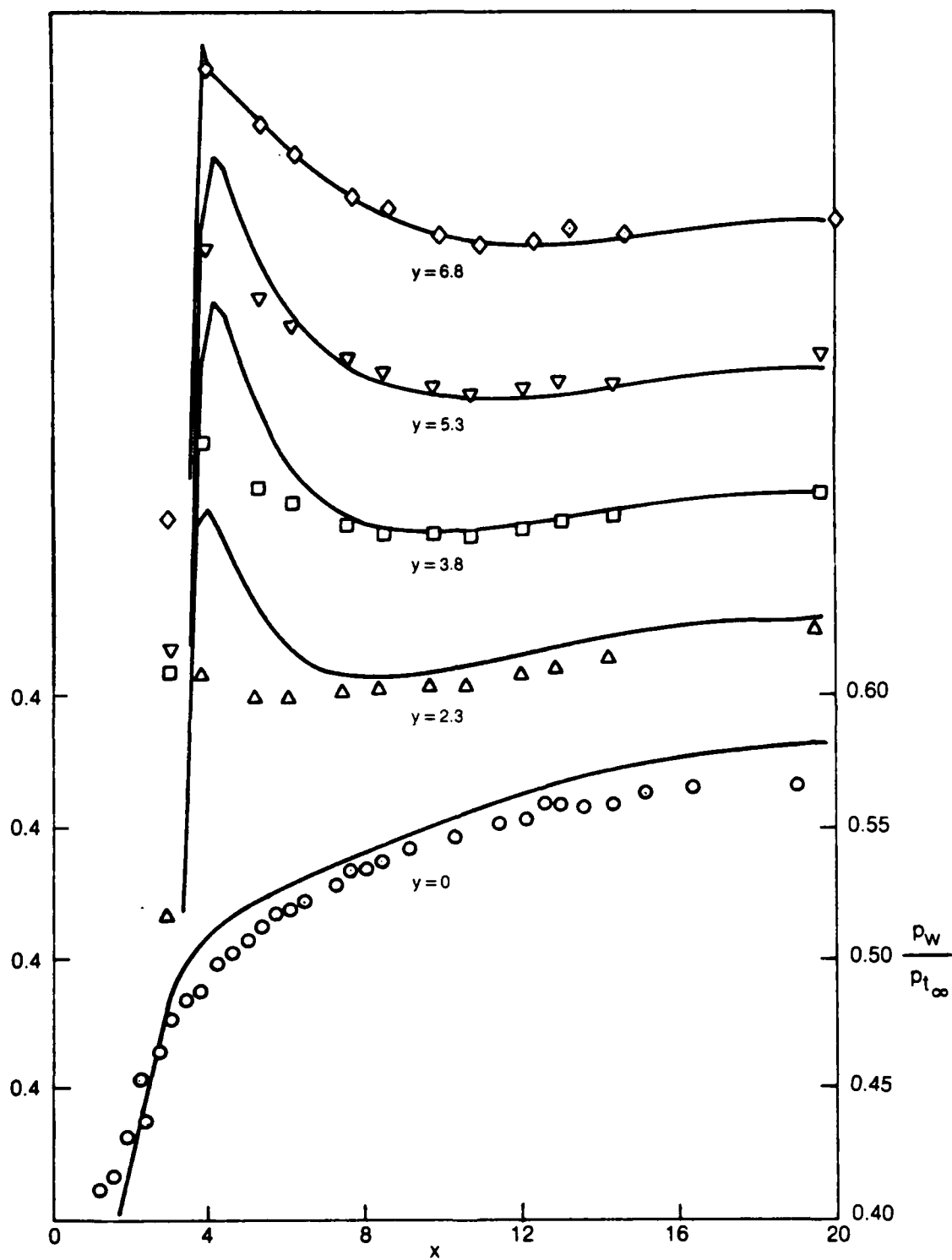


Fig. 23 Comparison of streamwise pressure distributions from IBLT ($p_y \neq 0$) and experimental data

CONTOUR LEGEND	
NO.	MACH NO.
1	0.85
2	0.90
3	0.95
4	1.00
5	1.05
6	1.10
7	1.15
8	1.20
9	1.25
10	1.30
11	1.35
12	1.40

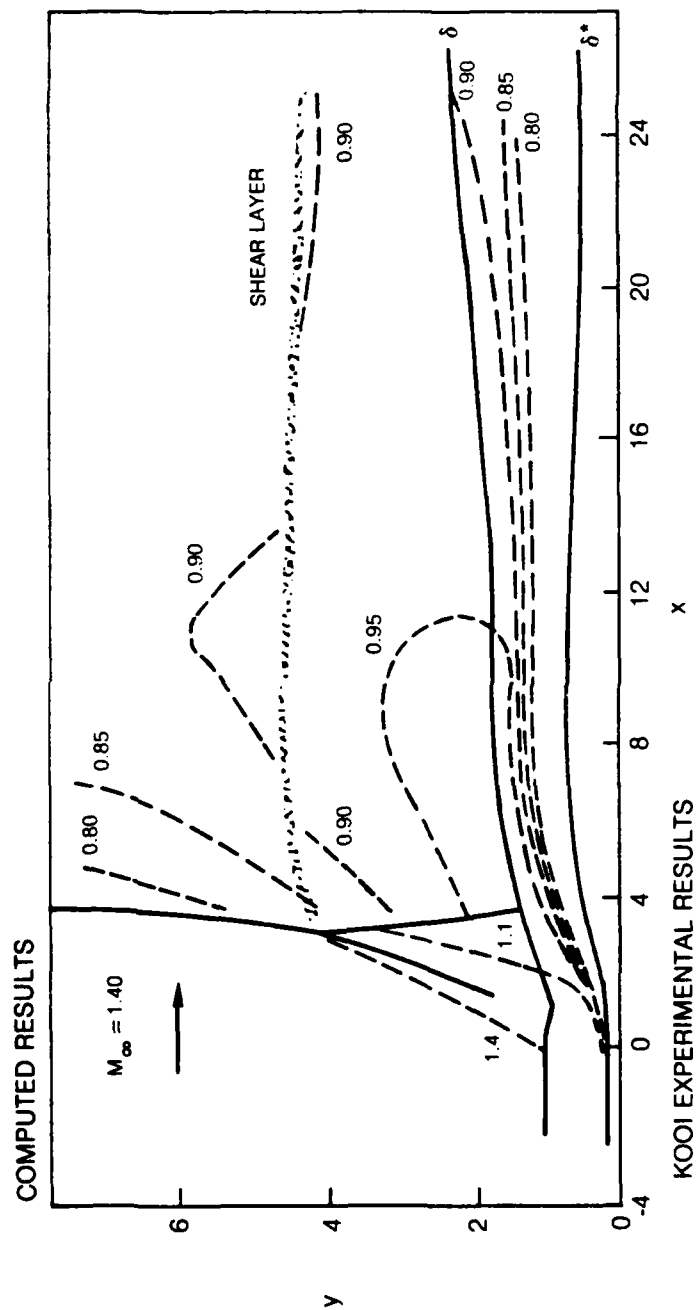
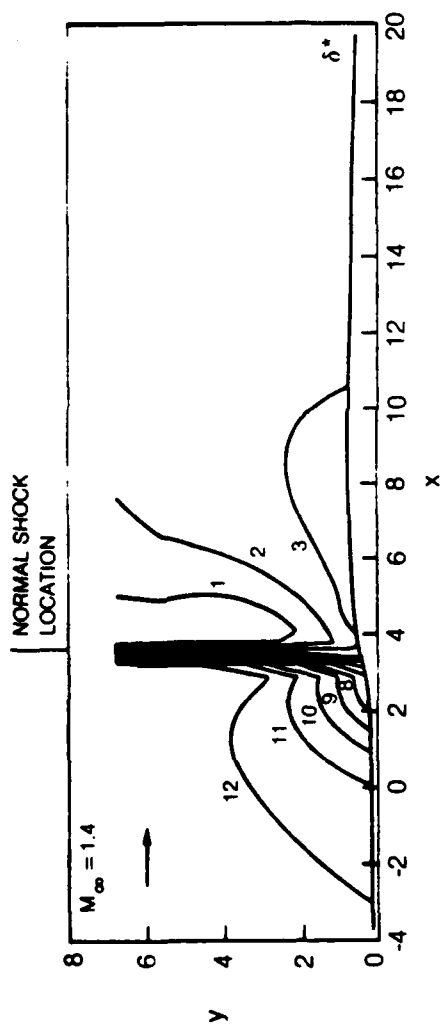


Fig. 24 Flow structure of normal shock-wave, boundary-layer interaction

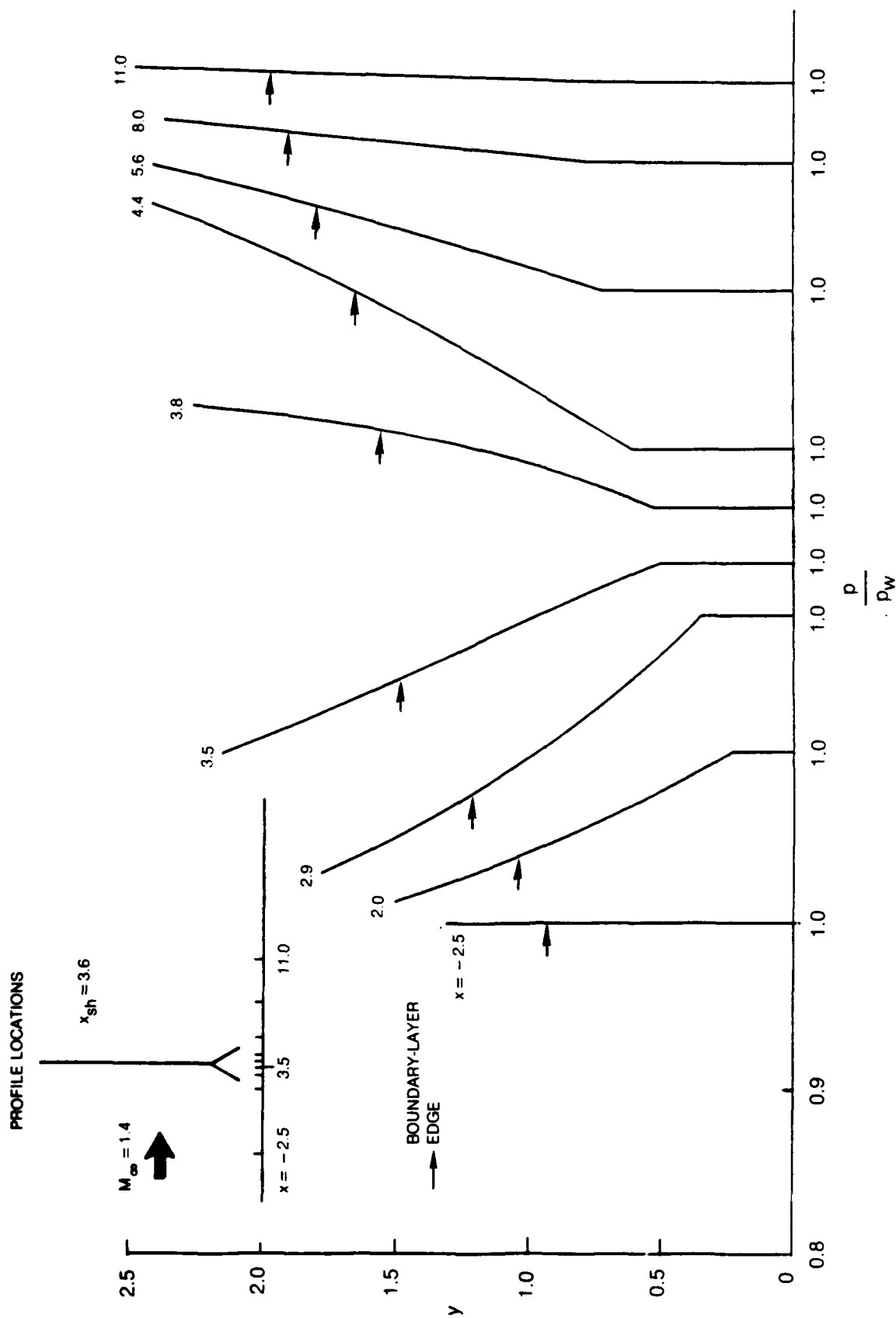


Fig. 25 Variation of pressure across boundary layer from equivalent inviscid flow (EIF) for transonic normal shock-wave, boundary-layer interaction

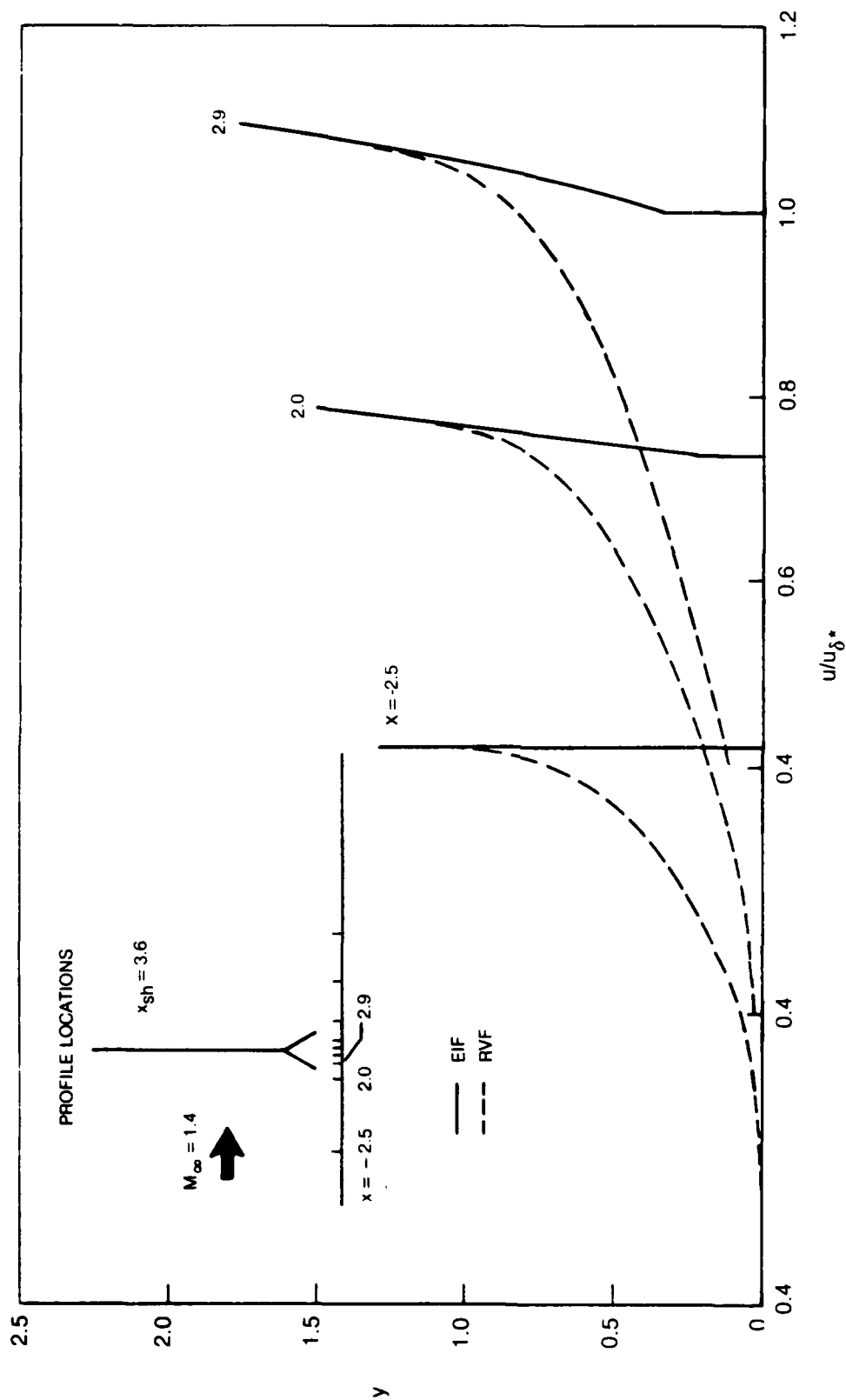


Fig. 26 Velocity from real viscous flow (RVF) and equivalent inviscid flow (EIF) for transonic normal shock-wave, boundary-layer interaction
a) $x = -2.5, 2.0, 2.9$

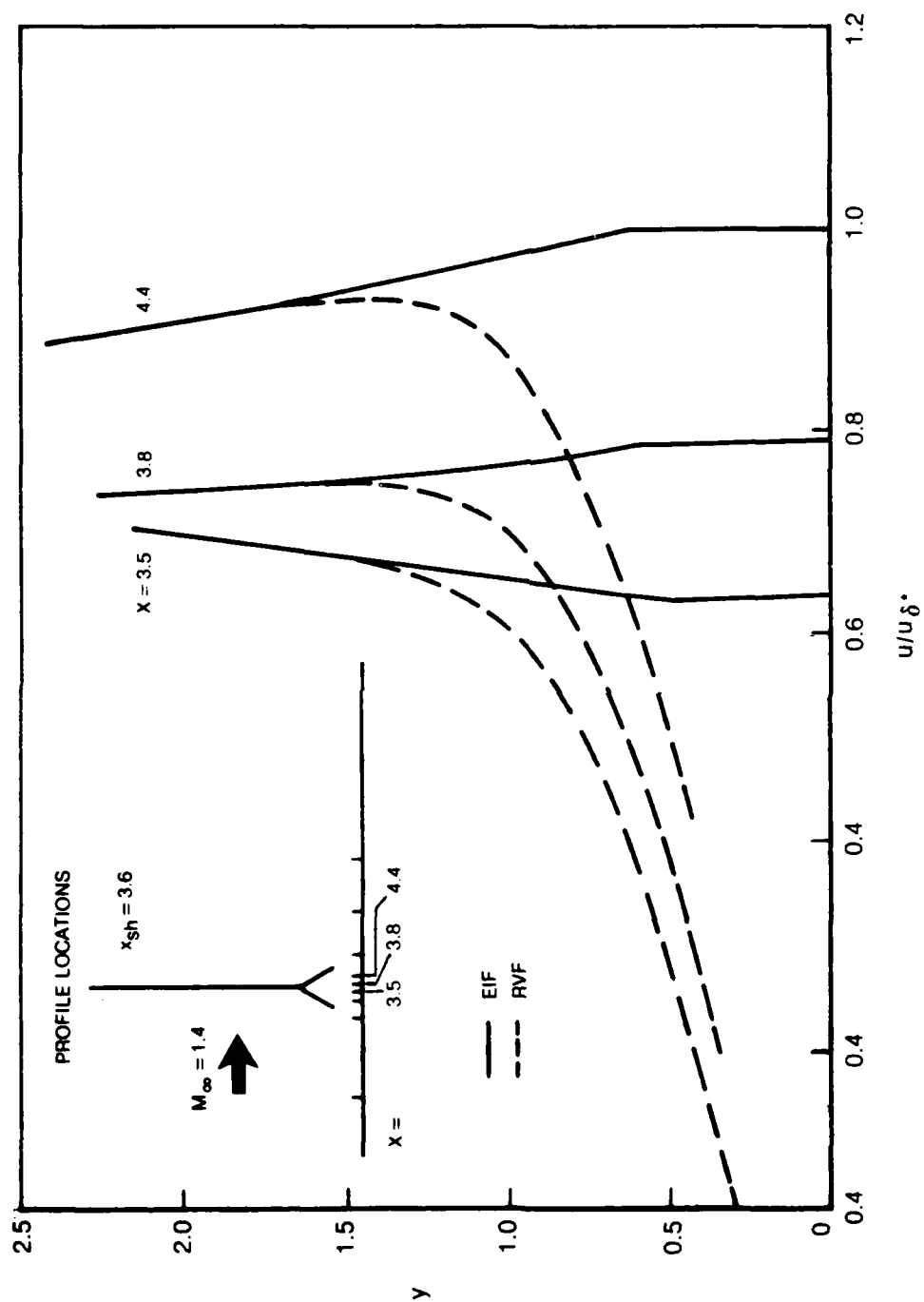


Fig. 26 Velocity from real viscous flow (RVF) and equivalent inviscid flow (EIF)
for transonic normal shock-wave boundary layer interaction
b) $x = 3.5, 3.8$, and 4.4

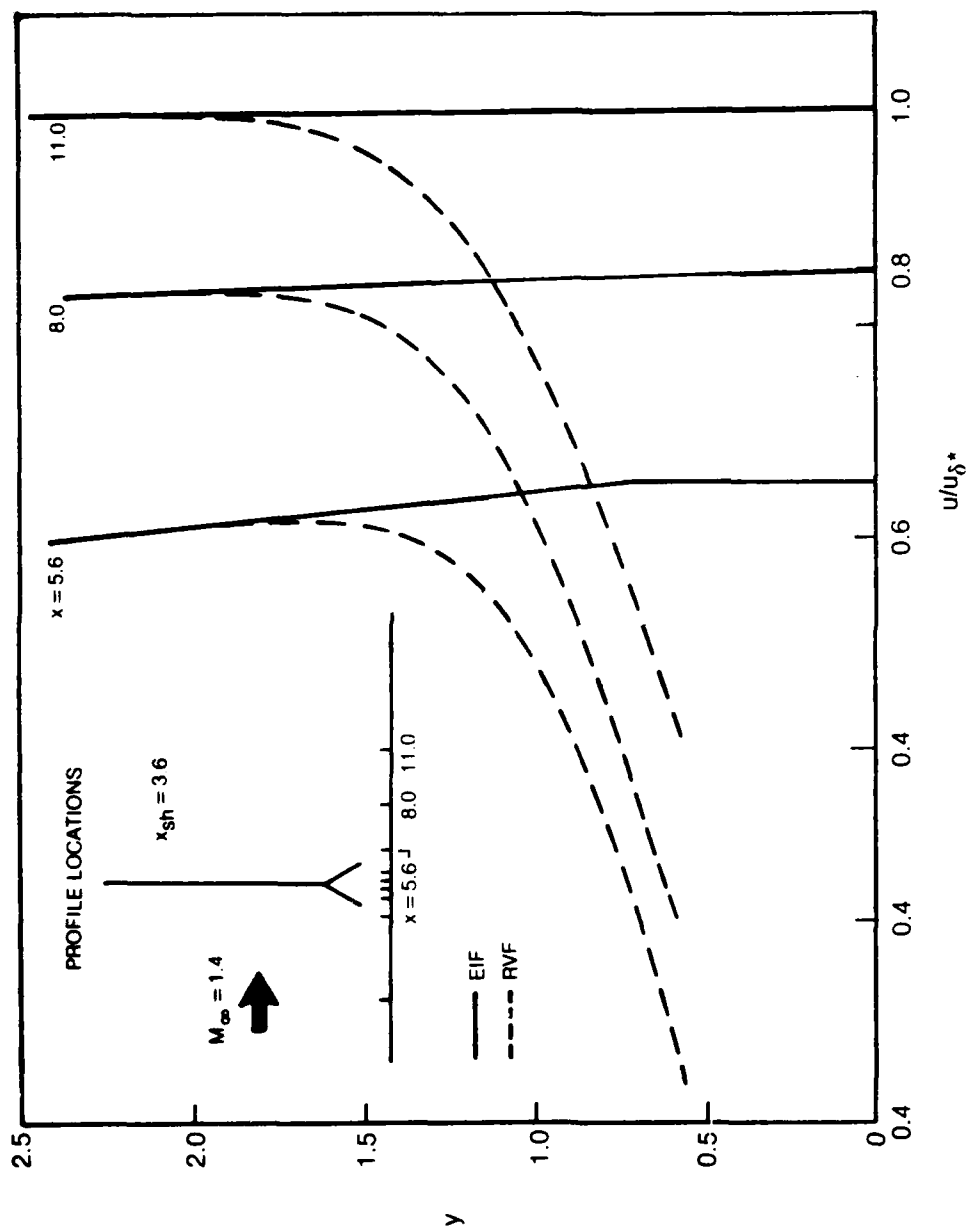


Fig. 26 Velocity from real viscous flow (RVF) and equivalent inviscid flow (EIF) for transonic normal shock-wave, boundary-layer interaction
c) $x = 5.6, 8.0$, and 11.0

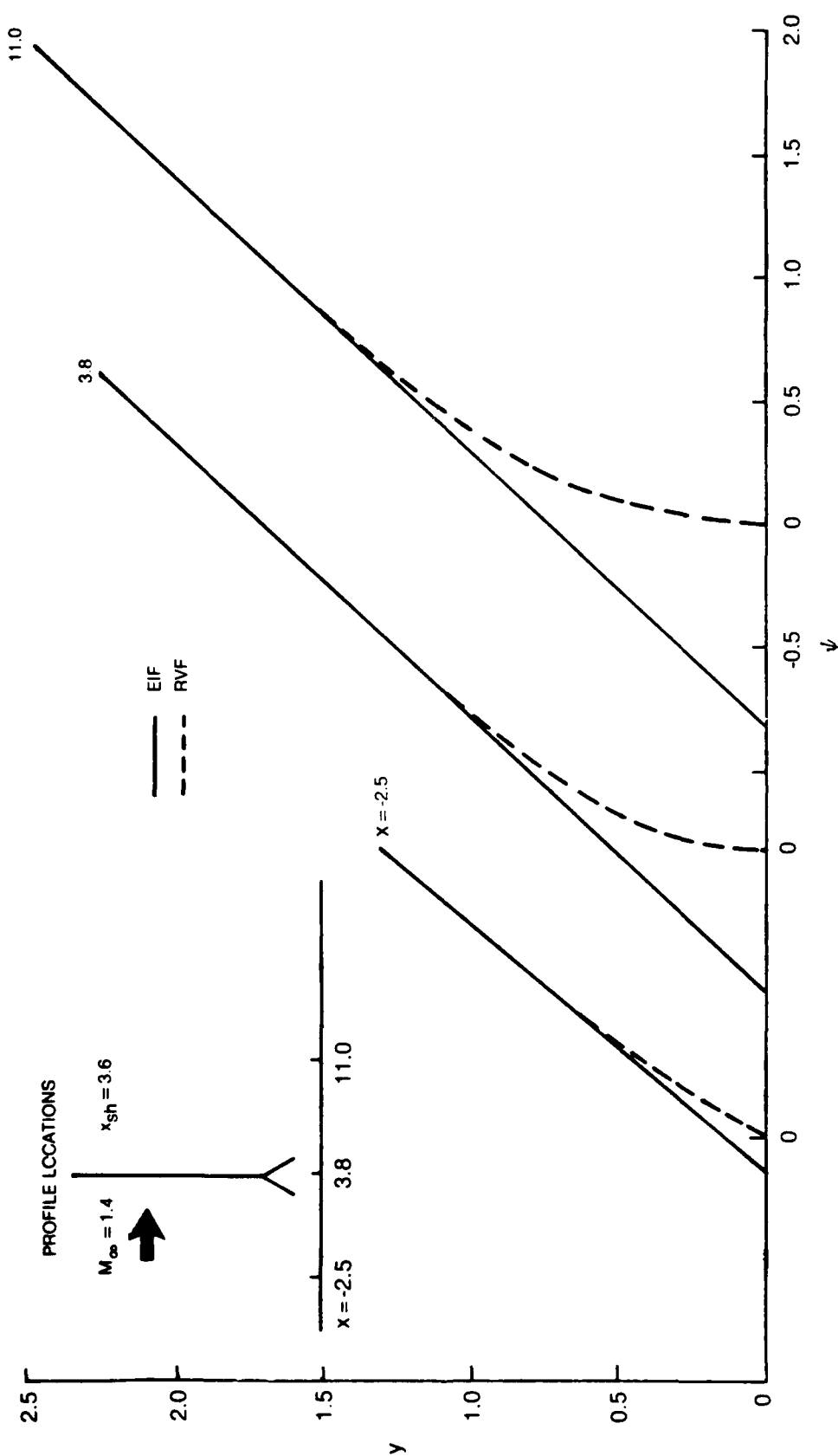


Fig. 27 Stream function profiles from real viscous flow (RVF) and equivalent inviscid flow (EIF) for transonic normal shock-wave, boundary-layer interaction

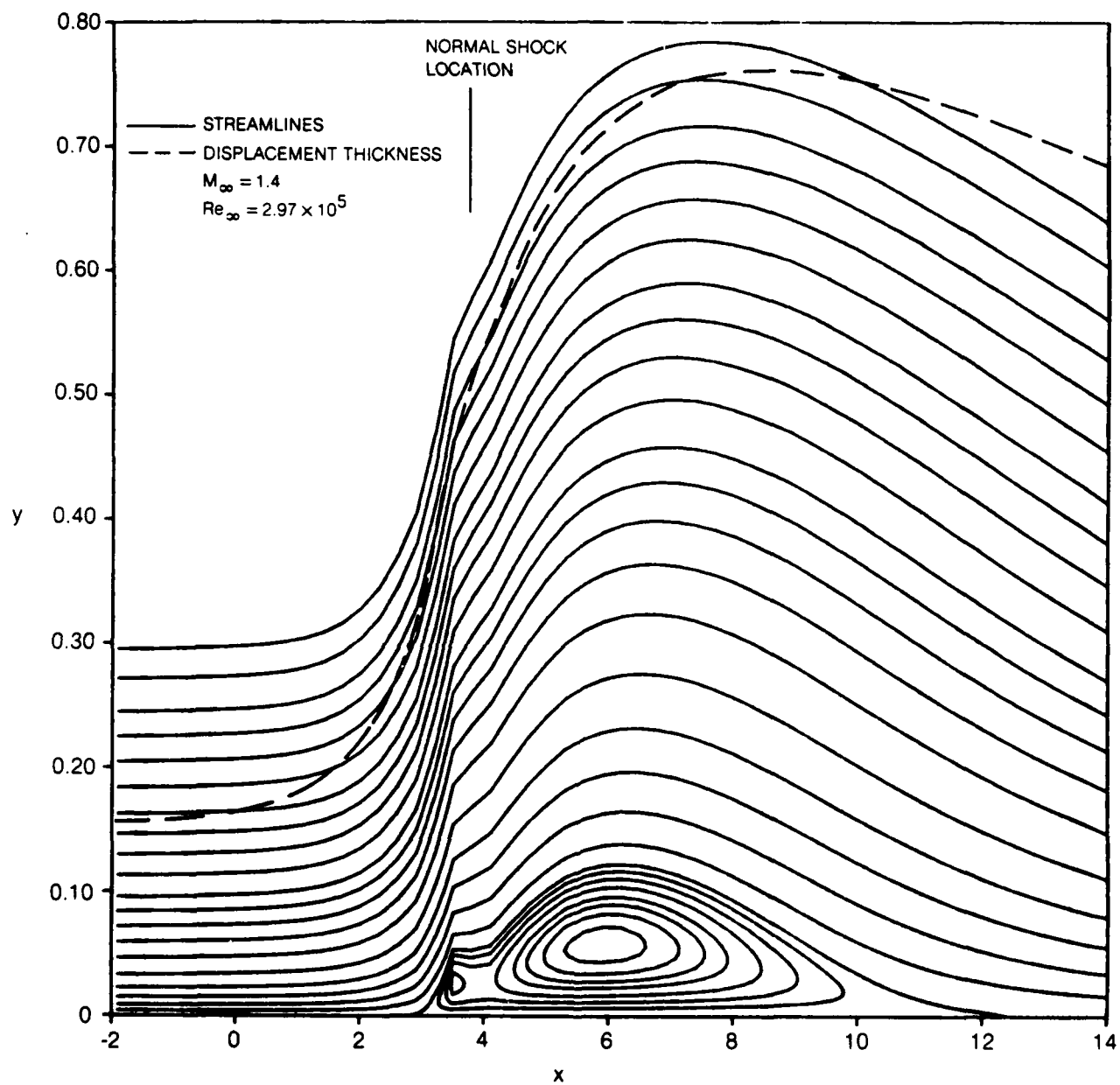


Fig. 28 Viscous streamlines and displacement thickness computed from IBLT, $p_y \neq 0$ for transonic normal shock-wave, boundary-layer interaction

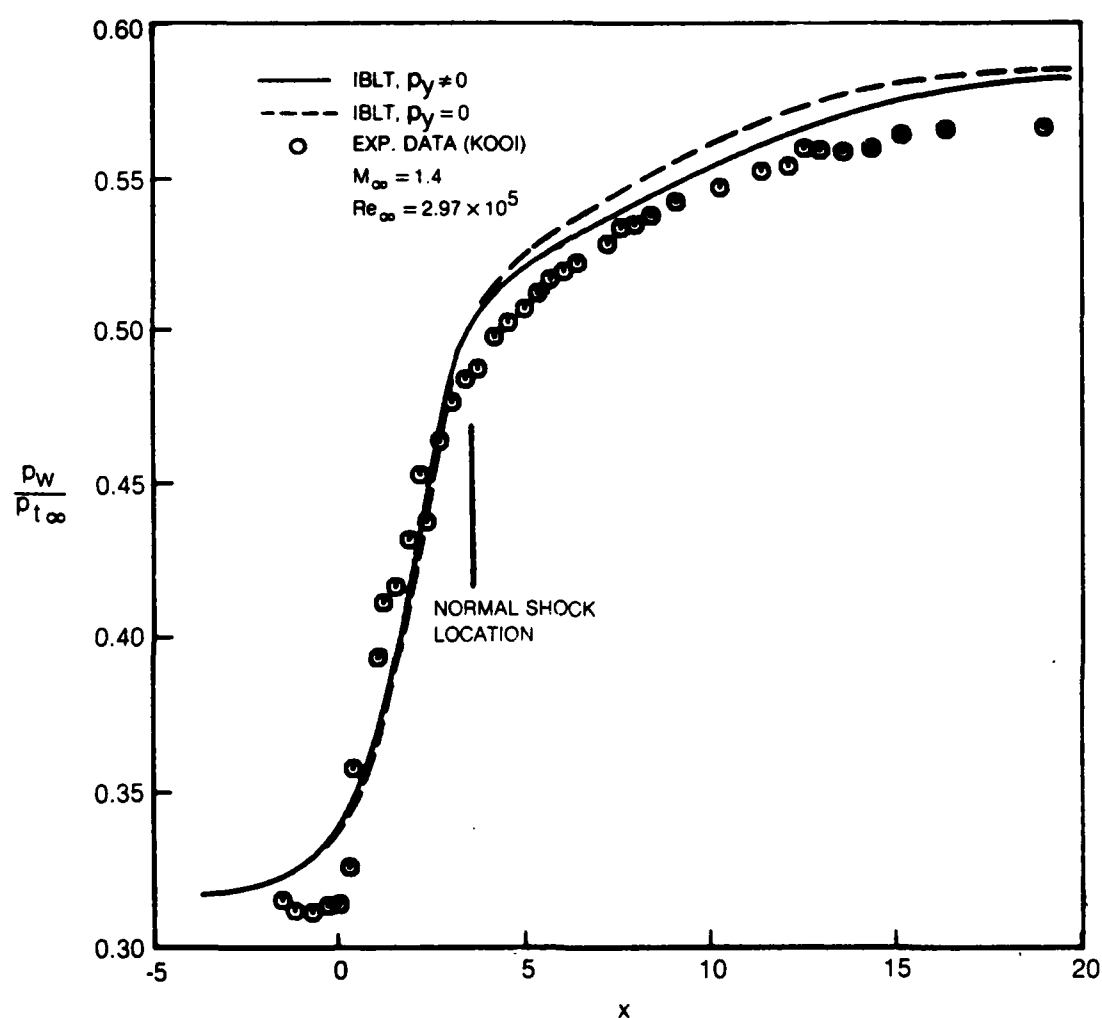


Fig. 29 Comparison of computed results from IBLT with and without normal pressure gradients across viscous layer for transonic normal shock-wave, boundary-layer interaction
a) Wall pressure

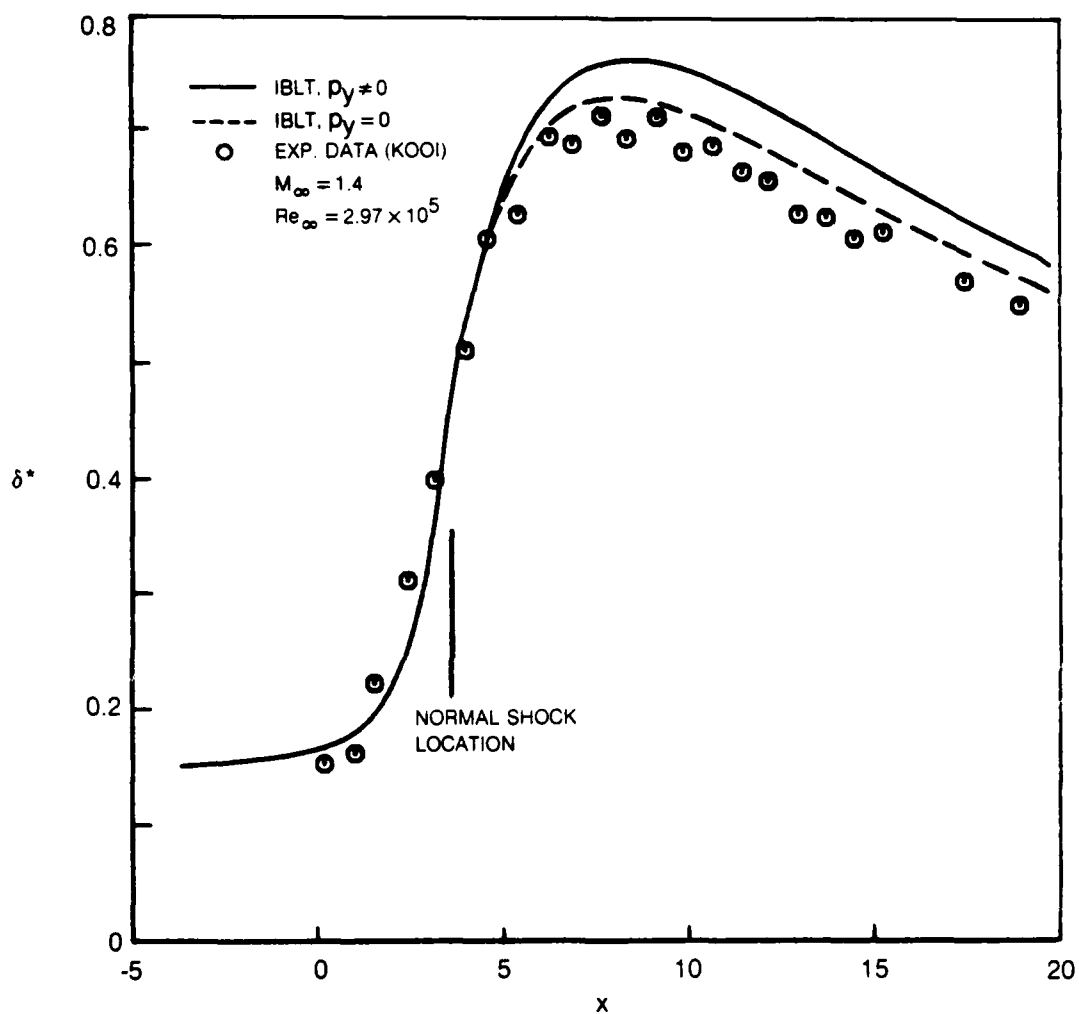


Fig. 29 Comparison of computed results from IBLT with and without normal pressure gradients across viscous layer for transonic normal shock-wave, boundary-layer interaction
b) Displacement thickness

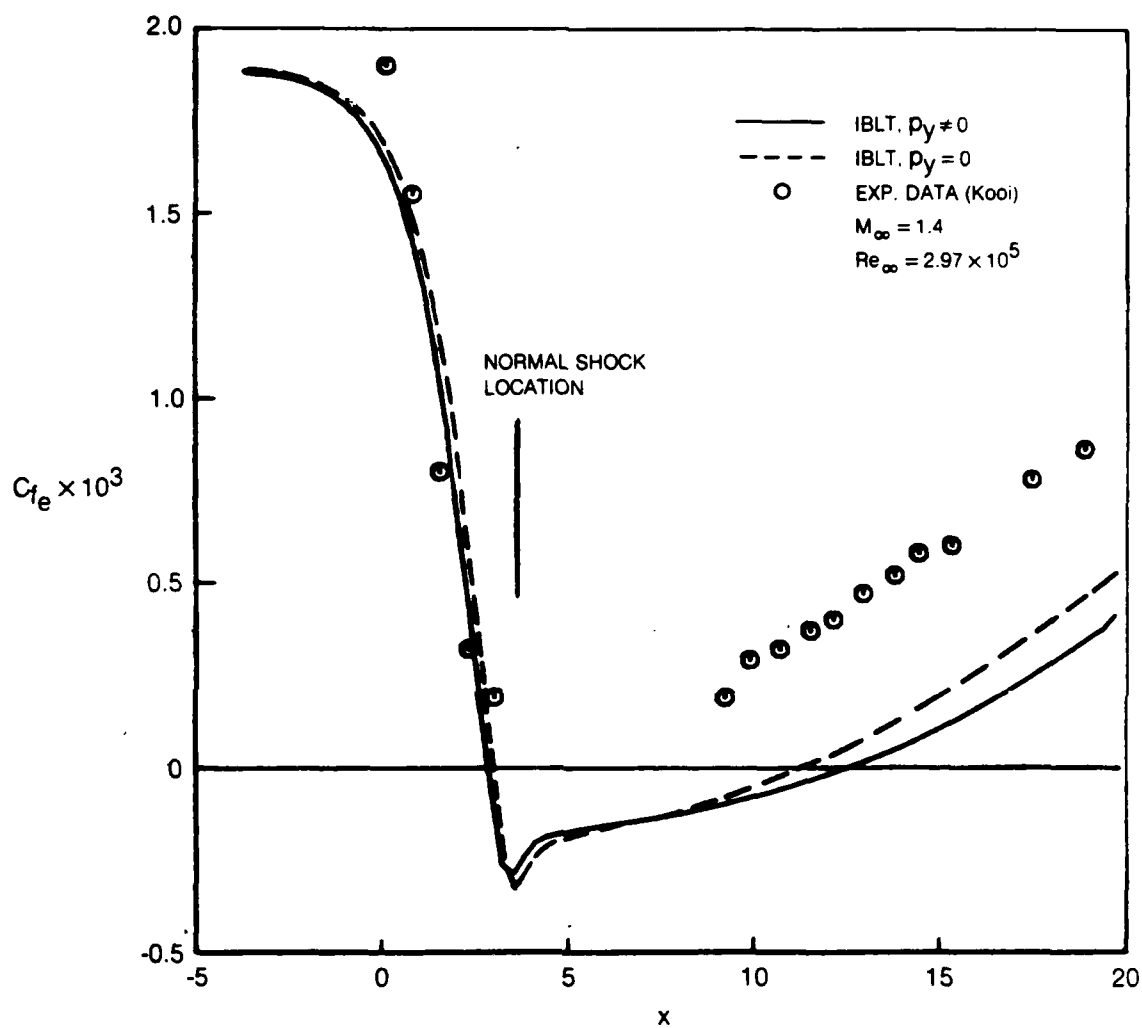


Fig. 29 Comparison of computed results from IBLT with and without normal pressure gradients across viscous layer for transonic normal shock-wave, boundary-layer interaction
c) Skin friction

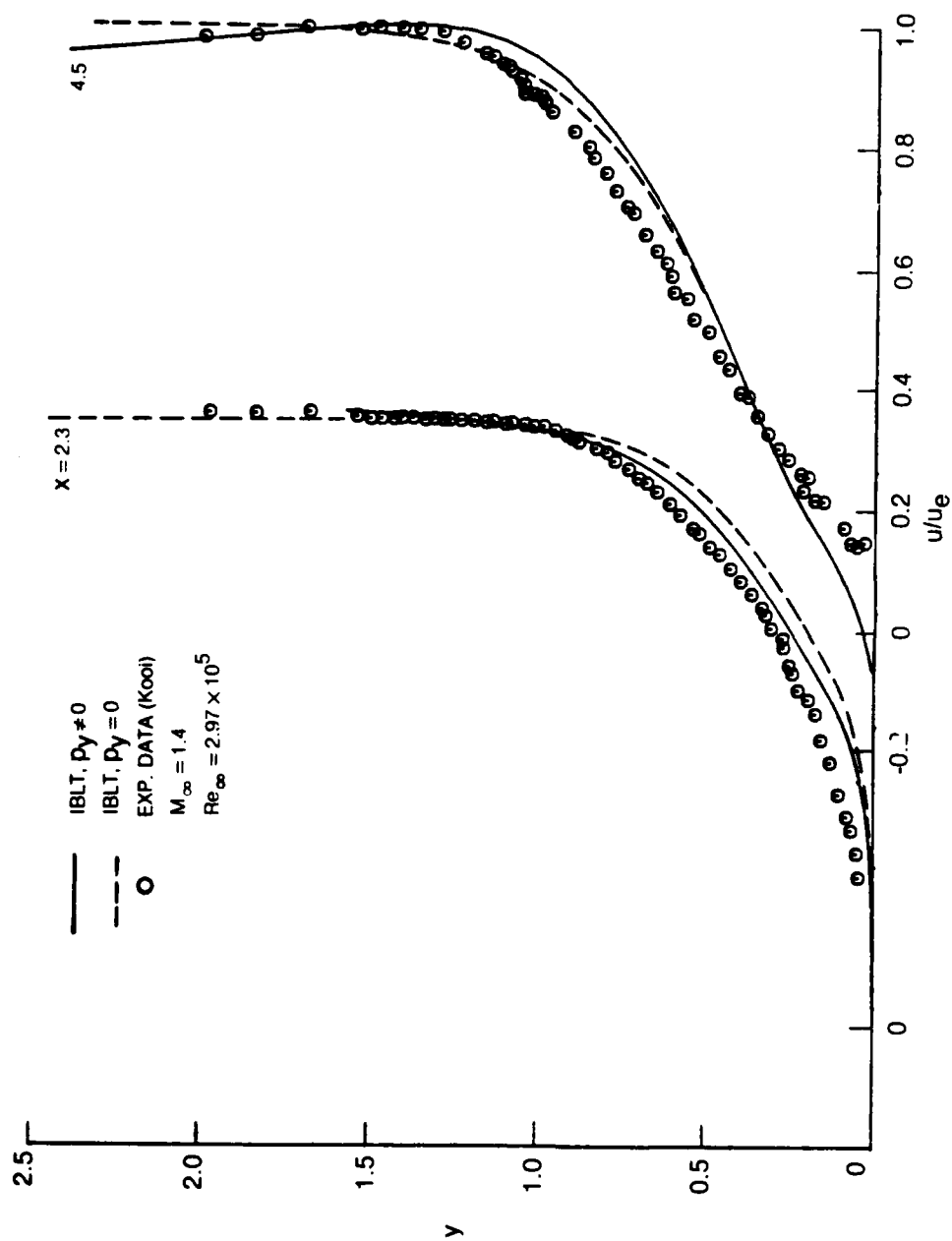


Fig. 30 Comparison of velocity profiles from experimental data and IBLT with and without normal pressure gradients across viscous layer

APPENDIX A

CALCULATIONS OF SEPARATION BUBBLES USING BOUNDARY-LAYER-TYPE EQUATIONS

A. Halim* and M. Hafez**

1. INTRODUCTION

Incompressible laminar flows with small separation bubbles have been successfully simulated using Navier Stokes equations for some years (see Roache⁽¹⁾). For example, Briley⁽²⁾ and Leal⁽³⁾ used stream function-vorticity formulation while Ghia et al⁽⁴⁾ used primitive variables. Simplified equations of the first formulation (where the streamwise viscous terms are neglected) were used by Ghia and Davis⁽⁵⁾, Werle and Bernstein⁽⁶⁾, Ghia, Ghia and Tesch⁽⁷⁾, and Inoue⁽⁸⁾. Similarly, partially parabolized, or semi-elliptic equations in terms of primitive variables were used by Mahgoub and Bradshaw⁽⁹⁾, and Rubin⁽¹⁰⁾.

In the first approach, careful treatment of the vorticity boundary condition at the wall is required, while conservation of mass is usually difficult to achieve in the second approach (see Orszag and Israeli⁽¹¹⁾).

Recently, boundary layer equations have been used to calculate separated flows. There are three main difficulties with classical boundary layer methods. First, it is well known that when the pressure is prescribed, the equations admit a singular solution (see the reviews by Brown and Stewartson⁽¹²⁾ and Williams⁽¹³⁾). By differentiating the x-momentum equation twice with respect to y and using the continuity equation, the shear stress at the wall is given by

*Research Engineer, The George Washington University, Joint Institute for Advancement of Flight Sciences, Hampton, VA
**Senior Scientist, Computer Dynamics, Inc., Virginia Beach, VA
The authors would like to acknowledge the support of NASA Langley Research Center; Office of Naval Research, Contract No. N00014-80-C-0494 and Air Force Office of Scientific Research Contract F49620-81-C-0041.

$$\frac{1}{2} (\tau^2)_x = C u_{yyyy} \quad (1)$$

Hence, unless, u_{yyyy} vanishes at the separation point, the shear stress has a square root singularity. More precisely, Goldstein⁽¹⁴⁾ showed that the function $\lim_{Re \rightarrow \infty} (Re^{1/2} \tau)$ which is

generally bounded upstream, is nonanalytic at the point of zero skin friction. There is no contradiction between this theory and Dean's results⁽¹⁵⁾ which show that the Navier-Stokes equations are analytic there. The limiting processes are different.

The second difficulty of direct boundary layer calculations is the possibility of nonunique solutions. This is clear from the similar solution. It has also been identified for non-similar solutions (see Murphy and King⁽¹⁶⁾ and the references therein).

Finally, the marching procedure is not stable for reversed flows. Flugge Lotz and Reyhner⁽¹⁷⁾ neglected the streamwise convective term when u is negative. More accurate solutions can be obtained by either using the appropriate upwind difference schemes and/or integrating the equations in the appropriate direction locally. The stability of such calculations can be improved by solving artificial time-dependent equations where the diagonal dominance is enhanced due to the time-like term.

The numerical breakdown of classical boundary layer methods near a separation point has been demonstrated by many authors (e.g. Wele and Davis⁽¹⁸⁾, Klienbergl and Steger⁽¹⁹⁾, and Fletcher and Dancey⁽²⁰⁾). The solution becomes singular and it is difficult to proceed the calculations downstream of the separation point. Following Goldstein's analysis, it can be shown that near the separation point x_s ,

$$\delta^*(x) = \delta^*(x_s) - \tau(x)/\frac{dp}{dx} + \dots \quad (2)$$

So that if $\frac{d\tau}{dx}$ is infinite there, so is $\frac{d\delta^*}{dx}$. Therefore regularity can be ensured by requiring either $\tau(x)$ or $\delta^*(x)$ to be regular. Catherall and Mangler⁽²¹⁾ were the first to obtain regular solution by specifying the displacement thickness. Carter⁽²²⁾ demonstrated that results of inverse boundary layer calculations are in good agreement with Navier Stokes solution. Similar success was reported by Cebeci, Keller, and Williams⁽²³⁾ using a nonlinear eigenfunction formulation. On the other hand, Klienbergl and Steger⁽¹⁹⁾ and Horton⁽²⁴⁾ specified the shear stress in their calculations and obtained regular solutions. Indeed, Horton concluded that the condition $u_{yyyy}=0$, at the separation point was satisfied up to the computational accuracy. It should be mentioned that specifying the displacement thickness leads to faster convergence and it seems it avoids the nonuniqueness problem.

The appropriate displacement thickness or wall shear must be obtained as part of the overall problem, from the interaction between the boundary layer and the inviscid flow. Calculation of laminar separation bubbles that includes this viscous inviscid interaction has been given by Carter and Wornom⁽²⁵⁾. On the other hand, it is argued that due to the interaction, the mainstream is always able to adjust itself to prevent the singularity from developing. Briley and McDonald⁽²⁶⁾⁽²⁷⁾ calculated the leading edge separated flows using a direct procedure, where the unsteady boundary layer equations are repeatedly solved until a steady state solution is obtained; after each time step, the prescribed pressure is updated from thin airfoil theory, thereby accounting for the displacement interaction. The same problem has been also solved by Kwon and Pletcher⁽²⁸⁾, Cebeci and Schimke⁽²⁹⁾, and Vatsa and Carter⁽³⁰⁾. Davis and Werle⁽³¹⁾⁽³²⁾ viewed the interactive boundary layer as an alternative to the asymptotic (triple deck) theory of Stewartson and Messiter. Recently, Carter⁽³³⁾, LeBalleur⁽³⁴⁾, Wigton⁽³⁵⁾, and Veldman⁽³⁶⁾ introduced different coupling procedures to accelerate the convergence of the interaction. For some special cases, inviscid rotational flow (see Taulbee and Robertson⁽³⁷⁾) or just boundary layer (see Pletcher⁽³⁸⁾) provide reasonable approximate solutions. In general, neither is uniformly valid and the interaction is required. The interaction reflects the boundary value nature of the problem which is important even for supersonic flows where (space-) marching procedures can be used for both the inviscid and the boundary layer parts separately (see Garvine⁽³⁹⁾).

In this paper, numerical calculations of separated flows are presented where boundary layer equations in terms of stream function, with different boundary conditions are integrated. For a retarded flow on a flat plate, results are compared with Briley's and Carter's solutions. More accurate models accounting for the pressure variation across the viscous layer are discussed. In many cases, the effect of such a variation is negligible.

For viscous inviscid interaction problems, a patching procedure is used where the unknowns along a vertical line in both domains are solved simultaneously leading to strong coupling. In this method, the grid should represent both the viscous and the inviscid scales, but the equations are simpler than the full Navier Stokes (biharmonic) equation.

2. A MODEL PROBLEM

Briley⁽²⁾ suggested to calculate retarded flows on a flat plate using Navier Stokes equations and compared the results with Howarth's boundary layer series solution where it breaks down at the separation point as predicted by Goldstein analysis. Later, Carter⁽²²⁾ prescribed the displacement thickness from Briley's solution and demonstrated that the inverse

boundary layer solution is in excellent agreement with Briley's results. Recently many authors solved the same problem - Amarante and Cheng⁽⁴⁰⁾ and Cebeci and Stewartson⁽⁴¹⁾ used interactive boundary layer methods while Inoue⁽⁸⁾ used parabolized Navier Stokes equations. We chose this model problem to test present formulations.

3. BOUNDARY LAYER EQUATIONS

In terms of the tangential and the normal velocity components, the continuity and the tangential momentum equations read:

$$u_x + v_y = 0 \quad (3)$$

$$uu_x + vu_y = -p_x + \nu u_{yy} \quad (4)$$

with the boundary conditions $u=v=0$ at $y=0$, and $u=u_e$ at $y=y_e$ (edge of boundary layer), where it is assumed that p_x does not vary with y . Equations (3) and (4) can be written in terms of stream function and vorticity, namely:

$$u\omega_x + v\omega_y = \nu\omega_{yy} \quad (5)$$

$$-\omega = \psi_{yy} \quad (6)$$

with the boundary conditions $\psi=\psi_y=0$ at $y=0$ and $\psi_y=u_e$ and $\omega=0$ at $y=y_e$.

Another form of the above equations is simply:

$$u\psi_{yyx} + v\psi_{yyy} = \nu\psi_{yyyy} \quad (7)$$

The advantage of form (7) is discussed next.

First, the discretization is straightforward; (for uniform mesh):

$$\psi_{yyyy} \approx (\psi_{i,j+2} - 4\psi_{i,j+1} + 6\psi_{i,j} - 4\psi_{i,j-1} + \psi_{i,j-2})/\Delta y^4 \quad (8-1)$$

$$\psi_{yyy} \approx (\psi_{i,j+2} - 2\psi_{i,j+1} + 2\psi_{i,j-1} - \psi_{i,j-2})/\Delta y^3/2. \quad (8-2)$$

$$\psi_{yyx} \approx ((\psi_{i,j+1} - 2\psi_{i,j} + \psi_{i,j-1}) - (\psi_{i-1,j+1} - 2\psi_{i-1,j} + \psi_{i-1,j-1}))\Delta y^2/\Delta x$$

$$\text{if } u > 0 \quad (8-3)$$

$$\approx ((\psi_{i+1,j+1} - 2\psi_{i+1,j} + \psi_{i+1,j-1}) - (\psi_{i,j+1} - 2\psi_{i,j} + \psi_{i,j-1})) / \Delta y^2 \Delta x$$

if $u < 0$ (8-4)

u and v are expressed in terms of ψ :

$$u \approx (\psi_{i,j+1} - \psi_{i,j-1}) / 2\Delta y \quad (8-5)$$

$$v_{C.D} \approx - (\psi_{i+1,j} - \psi_{i-1,j}) / 2\Delta x \quad (8-6)$$

or $v_{B.D} \approx - (\psi_{i,j} - \psi_{i-1,j}) / \Delta x \quad (8-7)$

At each $x=\text{constant}$ line the unknowns form a five diagonal scalar system of equations. Both wall boundary conditions can be easily incorporated implicitly. Similarly, the edge boundary conditions can be implemented by augmenting the system with the extra relations, for example $\psi_y = u_e$ and $\psi_{yy} = 0$. In this case, the non-zero coefficients of the matrix are shown in sketch (1).

$$\begin{bmatrix} x & & & & x \\ & x & & & \\ x & x & x & & \\ & x & x & x & x \\ & & & x & x & x & x & x \\ & & & & x & & \\ & & & & & x & x \end{bmatrix} \begin{bmatrix} \psi_J \\ \psi_{J-1} \\ \psi_{J-2} \\ \\ \psi_2 \\ \psi_1 \\ \psi_0 \end{bmatrix}$$

Sketch (1) - Nonzero Elements of the System Matrix

The resulting equations can be solved efficiently by a Gaussian elimination procedure specialized to five diagonal scalar systems (an extension of Thomas algorithm). For attached flows, assuming an initial profile is given and with a backward difference approximation of v , equation (7) is integrated by marching in the x -direction. Few iterations are required at each station to account for the nonlinearity. For separated flows, centered differences are used for v and a downstream boundary condition seems to be required. Two possibilities are tested, at the last station, a backward difference approximation is used for v or v is set equal to zero. Also, global (sweeps) rather than local iterations are employed.

4. PARTIALLY PARABOLIZED NAVIER STOKES EQUATIONS

In this model, only the streamwise viscous terms in the full equations are neglected, namely,

$$u_x + v_y = 0 \quad (9)$$

$$uu_x + vu_y = -p_x + \nu u_{yy} \quad (10)$$

$$uv_x + vv_y = -p_y + \nu v_{yy} \quad (11)$$

It is argued that the term v_{yy} in equation (11) is also of higher order.

Equations (9-11) can be written in terms of stream function and vorticity:

$$u\omega_x + v\omega_y = \nu\omega_{yy} \quad (12)$$

$$-\omega = \psi_{xx} + \psi_{yy} \quad (13)$$

The difference between equations (12) and (13) and the boundary layer equations (5) and (6) is the term ψ_{xx} in equation (13). Inoue⁽⁸⁾ solved equations (12)-(13) for Briley's problem and obtained close results.

Substituting equation (13) into equation (12) leads to a fourth order equation in ψ :

$$u(\psi_{xx} + \psi_{yy})_x + v(\psi_{xx} + \psi_{yy})_y = \nu(\psi_{xx} + \psi_{yy})_{yy} \quad (14)$$

Centered differences are always used for $\psi_{xx} + \psi_{yy}$, upwind differences are used for the streamwise convection operator $u\partial_x$. The wall boundary conditions are $\psi = \psi_y = 0$ and at the outer edge $\psi_{xx} + \psi_{yy} = 0$ and $\psi_y = u_e$.

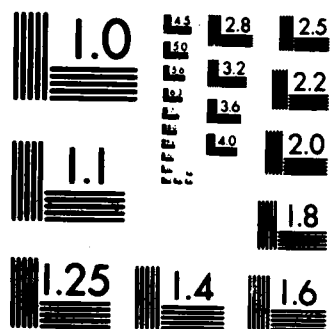
To solve equation (14), two artificial time dependent terms are added, $\alpha\psi_t$ and $\beta(\psi_{xx} + \psi_{yy})_t$ to enhance diagonal dominance. Again a five diagonal scalar system at each station is solved in the same manner the boundary layer equation (7) is solved. At the downstream boundary, the ψ_{xx} term in equation (14) is neglected and the equation reduces to equation (7). Global iteration is always needed.

The extra terms in equation (14) and not in equation (7) are:

$$-u\psi_{xxx} - v\psi_{xxy} + \nu\psi_{xxyy}$$

AD-A137 052 ANALYSIS OF TRANSONIC SHOCK INDUCED SEPARATED FLOW 2/2
INCLUDING NORMAL PRESS. (U) UNITED TECHNOLOGIES
RESEARCH CENTER EAST HARTFORD CT J E CARTER ET AL.
UNCLASSIFIED OCT 83 UTRC/R83-915712-2 AFOSR-TR-83-1283 F/G 20/4 NL

END



MICROCOPY RESOLUTION TEST CHART
NATIONAL BUREAU OF STANDARDS-1963-A

These terms are equal to p_{xy} which has been neglected in boundary layer calculations. For many cases, a boundary layer type equation can be used, where the term p_{xy} is lagged. For example, the pressure can be obtained from a triadiagonal system resulting from the discretization of:

$$p_{yy} = - (u v_x + v v_y)_y \quad (15)$$

with the boundary conditions:

$$p_y = 0 \quad \text{at the wall}$$

$$\text{and } p = H - \frac{1}{2} (u^2 + v^2) \quad (16)$$

at the outer edge, where H is a constant. In equation (15), the viscous term vv_{yyy} has been neglected. After the pressure is calculated, the term p_{xy} is updated. To ensure stability of calculations, the pressure is underrelaxed.

5. VISCOUS/INVISCID INTERACTION

The viscous terms are negligible far from the wall, and the flow becomes inviscid. There are several methods for boundary layer and inviscid calculations. Four possibilities are considered:

1. using Hilbert integral for inviscid flow and integral boundary layer calculations,
2. using Hilbert integral and finite difference boundary layer calculations,
3. using finite differences for inviscid flows and integral boundary layer calculations,
4. using finite differences for both inviscid and boundary layer flows.

In our opinion, except for class 4, the inviscid and viscous equations should be solved simultaneously (see for example references (42), (36), and (43)). A coupling procedure is needed only for class 4, where at each step, the inviscid and the boundary layer equations are solved separately; the coupling procedure update the boundary conditions for both calculations and the process is repeated until convergence.

An alternative formulation, based on a patching (or zonal) procedure is tested here. One requirement for the present method is the existence of an overlap region, where the equations on both sides are valid. In the viscous region, the partially parabolized Navier Stokes equations are used where the vorticity is convected and diffused. On the other hand, the

equation for the inviscid region is

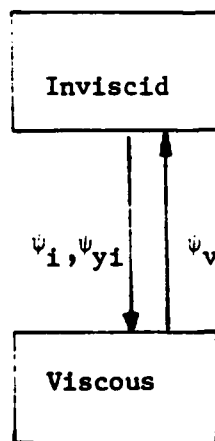
$$\psi_{xx} + \psi_{yy} = -\omega \quad (17)$$

where

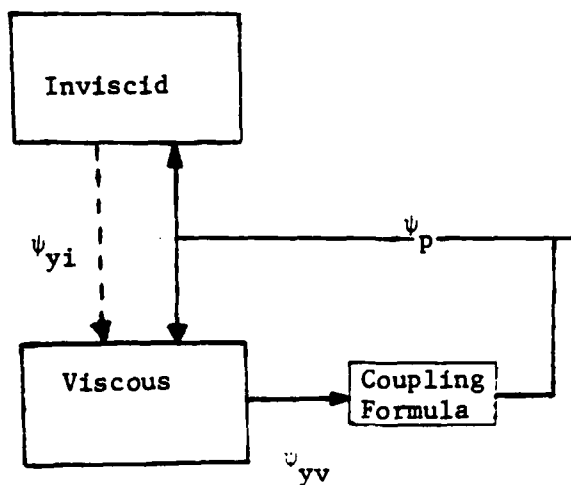
$$\omega = \omega(\psi) \quad (18)$$

i.e., the vorticity is only convected. Hence, the patching line should be in a region, where the viscous terms are negligible. If the patching line is chosen far from the wall, the vorticity there vanishes and the flow is irrotational. It is clear that this is a special case and the irrotationality is not necessarily required in the present method. Numerical implementation is simple. At each vertical line, the viscous terms are tested (for all the points), when they are relatively small, the five diagonal system is replaced by a tridiagonal system resulting from equation (17). It would be more efficient, to have a dynamic grid generation method, where the grid points are distributed according to the proper scales based on order of magnitude analysis.

If one wishes, for some reason (say to take full advantage of the different scales involved), to solve the viscous and the inviscid problem separately, a coupling procedure is needed. Two methods have been tested, the first is a direct local coupling and the second is a semi-inverse implicit procedure as shown in Sketches (2) and (3) respectively.



Sketch (2) - A direct local coupling procedure



Sketch (3-a) - A semi-inverse implicit coupling procedure.

$$\begin{bmatrix} K_{ii} & 0 & K_{ip} \\ 0 & K_{vv} & K_{vp} \\ K_{pi} & K_{pv} & K_{pp} \end{bmatrix} \begin{bmatrix} \psi_i \\ \psi_v \\ \psi_p \end{bmatrix}$$

ψ_i = unknowns in Inviscid Region, K_{ii} = matrix of inviscid equations

ψ_v = unknowns in Viscous Region, K_{vv} = matrix of viscous equations

ψ_p = unknowns along the patching line, K_{pp} = matrix of coupling equations

Sketch (3-b) - Partitioning of the total matrix for the implicit coupling procedure

In the first method, the patching line is chosen between grid points say P and P+1. ψ_p , from the viscous region is used as boundary condition for the inviscid calculations which provide ψ_{p+1} and ψ_{p+2} as boundary conditions for the viscous calculations. Convergence is achieved when ψ_p , ψ_{p+1} and ψ_{p+2} are the same (within some tolerance) in both calculations. The second method starts with an initial guess for p. The inviscid problem is solved first, followed by the viscous problem using the same values for ψ_p as well as ψ_{p+1} from the inviscid output. Next ψ_p is updated through a coupling formula, equation (19), and the process is repeated. The coupling formula is consistent with the inviscid equation, namely,

$$(\psi_{i+1,p}^{n+1} - 2\psi_{i,p}^{n+1} + \psi_{i-1,p}^{n+1})/\Delta x^2 + \alpha(\psi_{i,p+1}^{n+1} + \psi_{i,p-1}^{n+1})/\Delta y^2 - 2\psi_{i,p}^{n+1}/\Delta y^2 = -\omega(i,p) \quad (19)$$

where α is a relaxation parameter, $\psi_{i,p+1}$ is obtained from the inviscid calculations, while the viscous calculations provide $\psi_{i,p-1}$. A tridiagonal solver is used to obtain $\psi_{i,p}^{n+1}$. If the x-term and ω are neglected, equation (19) reduces to:

$$\psi_{i,p}^{n+1} = \psi_{i,p}^n + \alpha \frac{\Delta y}{2} (u_i - u_v) \quad (20)$$

Equation (20) is similar to Carter's formula⁽³³⁾. It is found, however, that equation (19) leads to faster convergence.

(As a side remark, we notice that, for transonic calculations, equation (19) should reflect, the local character of the flow, whether subsonic or supersonic and in this case, equation (19) is replaced by:

$$\delta\psi_{xx} - \beta\delta\psi_x - \alpha\delta\psi = -[(\psi_x/\bar{\rho})_x + (\psi_y/\bar{\rho})_y] \quad (19')$$

where $\delta\psi$ is $\psi^{n+1} - \psi^n$ and β and α are relaxation parameters and $\bar{\rho}$ is an artificial density to produce dissipation in the supersonic region. Transonic calculations will be reported elsewhere.)

6. NUMERICAL RESULTS

Three uniform meshes (in x and y) are used: Coarse (35, 77), intermediate (76, 77), and fine (151, 77). Howarth profile is specified at the upstream boundary. Different edge boundary conditions are tested. Five cases are discussed here.

Case 1: $\psi_e = u_e(y - \delta^*)$, and $\psi_{yy} = 0$, where δ^* is prescribed from Briley's solution.

Case 2: $\psi_e = u_e (y_e - \delta^*)$, and $\psi_y = u_e$.

Case 3: $\psi_y = \bar{u}$, and $\psi_{yy} = 0$, where \bar{u} is the output of Case 1.

Case 4: $\psi_y = u_e$, and $\psi_{yy} = 0$.

The results shown for Cases 1 to 4 are for intermediate mesh.

Case 5: Same as Case 4 but using fine mesh.

Case 1 is the same as Carter's inverse boundary layer calculations. Case 2 has a hybrid boundary condition where both ψ and ψ_y are prescribed. As expected, the solution is regular since by specifying ψ , v is guaranteed to be bounded. We notice that if ψ and ψ_y are prescribed at the wall and at $y=y_e$, an approximate solution, with closed streamlines is obtained using a cubic polynomial ($\psi_{yyy}=0$). Case 3 is interesting since it demonstrates that the calculations are stable and the solution is unique and regular. The results of Cases 4 and 5 are somewhat surprising since this is similar to the classical direct boundary layer calculations. There are, however, some differences, since centered differences are used for v and a downstream boundary condition is required. These results are, of course, for finite Reynolds number and finite grid size (the scheme is first order accurate). Indeed, if backward differences are used for v , the solution becomes singular as approaching the separation point and the calculation is not stable downstream of the zero skin friction point.

Figure (1) shows the streamlines calculated by Briley and by Carter. In figure (2), the corresponding streamlines of the five cases discussed above are presented. The rates of convergence are plotted in figure (3). We notice that the convergence is faster when ψ is prescribed. Comparing Case 1 to Carter's calculation, it is at least twice as fast. Figures (4) and (5) show the displacement thickness and the wall shear distributions.

The discrepancy between the boundary layer solutions of Cases (4) and (5) and the Navier Stokes solution may be due to the different boundary conditions. In Briley's calculation, $\psi_{xx} + \psi_{yy} = -\omega = 0$ is used, while the boundary layer approximation of the vorticity, ψ_{yy} is set equal to zero in Cases 4 and 5. From the streamlines shown in figure (1), it is clear that at $y=y_e$, ψ_{xx} does not vanish.

If viscous inviscid interaction is allowed, the results do not agree with Briley's, since in his study, it was assumed that "along the outer flow boundary u was available from an inviscid solution. In the resulting Navier Stokes solution, the v -component of velocity along the outer-flow boundary generally will not agree with that from the inviscid solution used to prescribe the distribution of u along that boundary, and the

mismatch in v is an indication of interaction between the inviscid and viscous solutions which has been neglected. To account for the interaction, it would be necessary to successively recompute the inviscid and Navier-Stokes solutions, allowing in some manner for the influence of one upon the other, until the two solutions no longer change significantly."

The present viscous inviscid interaction method described above, does not produce any separation for the cases Briley solved. In a recent paper, by Cebeci and Stewartson⁽⁴¹⁾, it was shown that, based on interactive boundary layer calculations, the critical value of x_0 (a parameter defining the corner point of the external velocity) to induce separation is 0.215 for $Re=10^6/48$. Comparable results, for the displacement thickness are shown for $x_0=0.23$ (corresponding to Briley's solution for $x_0=0.202$). They found that there is a maximum value of x_0 , after which the numerical procedure breaks down. Furthermore, this maximum value is a decreasing function of Reynolds number and seems to approach the value 0.12 predicted by Howarth. It was concluded that there is a bound to the usefulness of interactive boundary layer theory, and once it is exceeded the theory in some sense goes sour; possibly the global flow properties then rapidly change over to those corresponding to Kirchhoff free-streamline flow.*

Cebeci and Stewartson used Hilbert integral for inviscid flow and Keller's box scheme for the boundary layer calculation. Their results are compared to the present viscous inviscid calculations where finite differences are used for both regions, as shown in figure (6). The agreement is reasonable, taking into consideration the finite domain of integration of the finite difference calculations (130x115 points are used with $x_e=1.2$, and $y_e\sqrt{Re} = 8.11$). The performance of the present method for the cases where the interactive boundary layer calculations diverge is the subject of further investigation.

7. CONCLUDING REMARKS

The boundary layer equations, in terms of a stream function (differentiated to yield a fourth order equation) is integrated, marching in the main stream direction. A special Gaussian elimination procedure is applied to a scalar five diagonal system of equations at each step, which, in a sense, is similar to Davis Coupled Method⁽⁴⁴⁾ (where continuity and momentum equations are solved together). The present scheme is not, however, as compact as Cranck-Nicholson's or Keller's box schemes⁽⁴⁵⁾. Nevertheless, for boundary layer type calculations, a smooth stretching transformation is usually employed and accuracy is not sacrificed for the resulting nonuniform mesh.

Solutions of retarded flows are presented for different outer boundary conditions, namely direct, inverse and hybrid.

*Navier Stokes solutions similar to those of Briley (but with higher Re , x_0 , and y_e) were successfully calculated by Murphy⁽⁴⁶⁾.

Regular solutions at the separation and reattachment points are obtained. Since centered differences are used for $v = -\psi_x$, a downstream boundary condition is required and thus nonuniqueness as well as singularities are avoided, at least for this formulation with the grid size and the Reynolds numbers considered.

To allow for viscous inviscid interaction, a patching procedure is tested where a partially parabolized Navier-Stokes equation for ψ is solved simultaneously with the inviscid Poisson equation via a vertical line relaxation. For each line, a coupled system (tridiagonal in the inviscid region and five diagonal in the viscous region) is solved by efficient Gaussian elimination. Artificial time-dependent terms are added to enhance the stability of calculations.

It seems that the present stream function formulation leading to a single equation is advantageous for discretization and convergence. In this work, only small separation bubbles are calculated. Simulation of large regions of massive separation would be of great interest; for such cases, however, the flow in reality may not remain laminar.

References

1. ROACHE, P. - Computational Fluid Dynamics, Hermosa Pub., 1972.
2. BRILEY, W. R. - A numerical study of laminar separation bubbles using the Navier-Stokes equations, J. Fluid Mech., Vol. 47, pp. 713-736, 1971.
3. LEAL, L. G. - Steady separated flow in a linearly decelerated free stream, J. Fluid Mech., Vol. 59, pp. 513-535, 1973.
4. GHIA, V., GHIA, K. N., RUBIN, S. G. and KHOSLA, P. K. - Study of separated flow in a channel using primitive variables, Computers and Fluids, Vol. 9, pp. 123-142, 1981.
5. GHIA, V. and DAVIS, R. T. - Navier-Stokes solutions for flow past a class of two-dimensional semi-infinite bodies, AIAA Journal, Vol. 12, No. 12, pp. 1659-1665, 1974.
6. WERLE, M. J. and BERNSTEIN, J. M. - A comparative numerical study of models of the Navier-Stokes equations for incompressible separated flows, AIAA Paper 74-48, Jan. 1975.
7. GHIA, K. N., GHIA, V., and TESCH, W. A. - Evaluation of several approximate models for laminar incompressible separation by comparison with complete Navier-Stokes solutions, AGARD Conf. Proc. No. 168, pp. 6-1 to 6-15, 1975.
8. INOUE, O. - Separated boundary layer flows with high Reynolds numbers, Lecture Notes in Physics, Vol. 141, pp. 224-229, 1981.
9. MAHGOUB, H., BRADSHAW, P. - Calculation of Turbulent inviscid flow interactions with large normal pressure gradients, AIAA J., Vol. 17, pp. 1025-1029, 1979.

10. RUBIN, S. - Incompressible Navier-Stokes and parabolized Navier-Stokes formulations and computational techniques, this volume.
11. ORSZAG, S. and ISRAELI, M. - Numerical simulation of viscous incompressible flows, *Ann. Rev. Fluid Mech.*, Vol. 6, pp. 281-318, 1974.
12. BROWN, S. and STEWARTSON, K. - Laminar separation, *Ann. Rev. Fluid Mech.*, Vol. 1, pp. 45-72, 1969.
13. WILLIAMS, J. - Incompressible boundary layer separation, *Ann. Rev. Fluid Mech.*, pp. 113-144, 1979.
14. GOLDSTEIN, S. - On laminar boundary layer flow near a position of separation, *Quart. J. Mech. Appl. Math.*, Vol. 1, pp. 43-69, 1948.
15. DEAN, W. - Note on the motion of liquid near a position of separation, *Proc. Camb. Phil. Soc.*, Vol. 46, pp. 293-306, 1950.
16. MURPHY, J. and KING, L. - Airfoil Flow-field calculations with coupled boundary-layer potential codes, Second Symposium on Numerical and Physical Aspects of Aerodynamic Flows, Calif. State Univ., Long Beach, CA, 1983.
17. REYHNER, T. A. and FLUGGE-LOTZ, I. - The interaction of a shock wave with a laminar boundary layer, *Int. J. on Non-Linear Mech.*, Vol. 3, No. 2, pp. 173-199, 1968.
18. WERLE, M. and DAVIS, R. - Incompressible laminar boundary layers on a parabola at angle of attack: A study of the separation point, *J. of Appl. Math.*, Vol. 7, 1972.
19. KLIENBERG, J. and STEGER, J. - On laminar boundary-layer separation, AIAA Paper 74-94, 1974.
20. PLETCHER, R. and DANCEY, C. - A direct method of calculating through separated regions in boundary layer flow, *J. of Fluids Engineering*, pp. 568-572, 1976.
21. CATHERALL, D. and MANGLER, K. - The integration of the two-dimensional laminar boundary-layer equations past a point of vanishing skin friction, *J. Fluid Mech.*, Vol. 26, pp. 163-182, 1966.
22. CARTER, J. - Inverse solutions for laminar boundary layer flows with separation and attachment, NASA TR R-447, 1975.
23. CEBECI, T., KELLER, H. and WILLIAMS, P. - Separating boundary-layer flow calculations, *J. of Comp. Physics*, Vol. 31, pp. 363-378, 1979.
24. HORTON, H. - Separating laminar boundary layers with prescribed wall shear, AIAA J., Vol. 12, 1974.
25. CARTER, J. and WORNOM, S. - Solutions for incompressible separated boundary layers including viscous-inviscid interaction, NASA SP 347, 1975.
26. BRILEY, W. and McDONALD, H. - Numerical prediction of Incompressible separation bubbles, *J. Fluid Mech.*, Vol. 69, pp. 631-656, 1975.
27. BRILEY, W. and McDONALD, H. - A survey of recent work of interacted boundary layer theory for flow with separation, Second Symposium on Numerical and Physical Aspects of Aerodynamic Flows, Calif. State Univ., Long Beach, CA, 1983.

28. KWON, O. and FLETCHER, R. - Prediction of subsonic separation bubbles on airfoils by viscous-inviscid interaction, Second Symposium on Numerical and Physical Aspects of Aerodynamic Flows, Calif. State Univ., Long Beach, CA, 1983.
29. CEBECI, T. and SCHIMKE, S. - The calculation of separation bubbles in interactive turbulent boundary layers, J. Fluid Mech., Vol. 131, pp. 305-317, 1983.
30. VATSA, V. and CARTER, J. - Analysis of airfoil leading edge separation bubbles, AIAA Paper 83-0300, 1983.
31. DAVIS, R. and WERLE, M. - Numerical methods for interacting boundary layers, Proc. 1976 Heat Transfer Fluid Mech. Institute, Stanford Univ. Press, 1976.
32. DAVIS, R. and WERLE, M. - Progress on Interacting boundary layer computations at high Reynolds number, First Symposium on Numerical and Physical Aspects of Aerodynamic Flows, Calif. State Univ., Long Beach, CA, 1981.
33. CARTER, J. - A new boundary-layer inviscid iteration technique for separated flow, AIAA Paper 79-1450, 1979.
34. LeBALLEUR, J. - Numerical flow calculation and viscous-inviscid interaction techniques, this volume.
35. WIGTON, L. and HOLT, M. - Viscous-Inviscid interaction in transonic flow, AIAA Paper 81-1003, 1982.
36. VELDMAN, A. - New, quasi-simultaneous method to calculate interacting boundary layers, AIAA J., Vol. 19, No. 1, pp. 79-85, 1981.
37. TAULBEE, D. and ROBERTSON, J. - Turbulent separation analysis ahead of a step, J. of Basic Engineering, Vol. 94, pp. 544-550, 1972.
38. FLETCHER, R. - Calculation of separated flows by viscous-inviscid interaction, this volume.
39. GARVINE, R. - Upstream influence in viscous interaction problems, Physics of Fluids, Vol. 11, pp. 1413-1423, 1968.
40. AMARANTE, J. and CHENG, I. - On the viscous-inviscid flow interactions in the vicinity of a laminar separation bubble, AIAA Paper 79-1478, 1979.
41. CEBECI, T. and STEWARTSON, K. - On the calculation of separation bubbles, J. Fluid Mech., Vol. 133, pp. 287-296, 1983.
42. GOHSE, S. and KLINE, S. - The computation of optimum pressure recovery in two dimensional diffusers, J. of Fluids Engineering, Vol. 100, pp. 419-426, 1978.
43. MOSES, H., JONES, R., and O'BRIEN, W. - Simultaneous solution of the boundary layer and freestream with separated flow, AIAA J., Vol. 16, No. 1, pp. 61-66, 1978.
44. BLOTTNER, F. - Investigation of some finite-difference techniques for solving the boundary layer equations, Comp. Meth. Appl. Mech. Eng., Vol. 6, pp. 1-30, 1975.
45. KELLER, H. - Numerical methods in boundary layer theory, Ann. Rev. Fluid Mech., Vol. 10, pp. 417-433, 1978.
46. MURPHY, J. - An efficient solution procedure for the incompressible Navier Stokes equations, AIAA J., Vol. 15, No. 9, pp. 1307-1314, 1977.

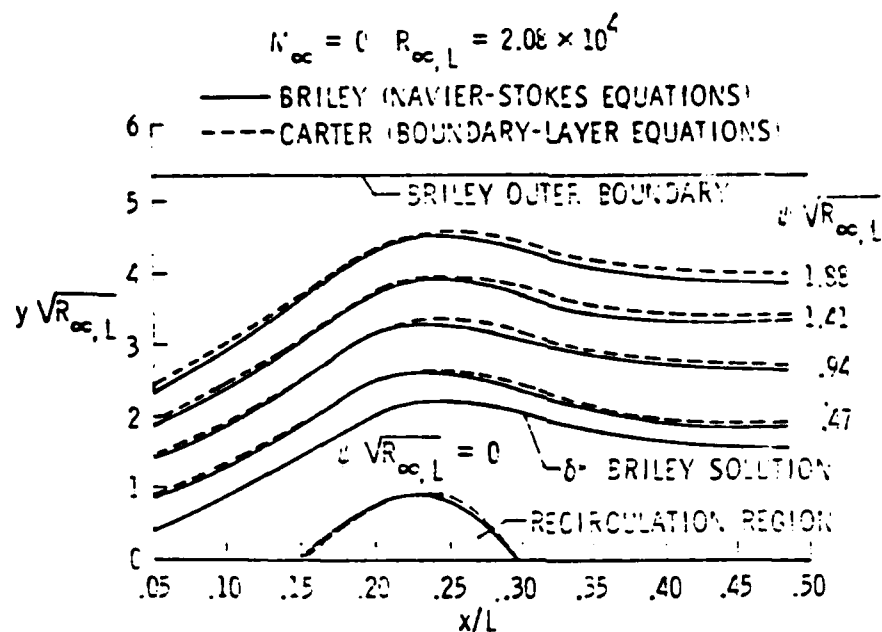


Figure (1) Streamlines from Briley's and Carter's Solution

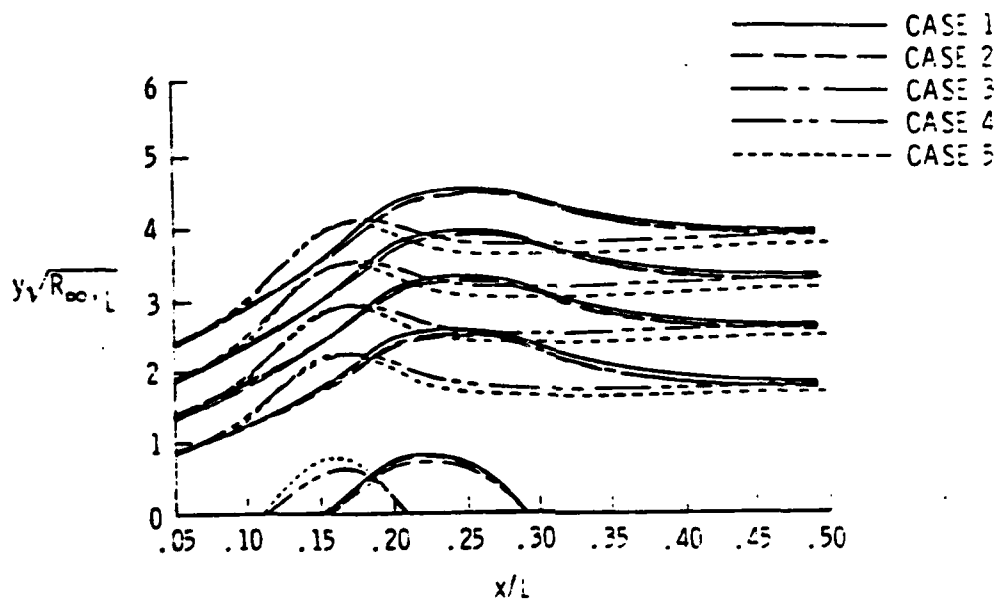


Figure (2) Streamlines from present boundary layer calculations

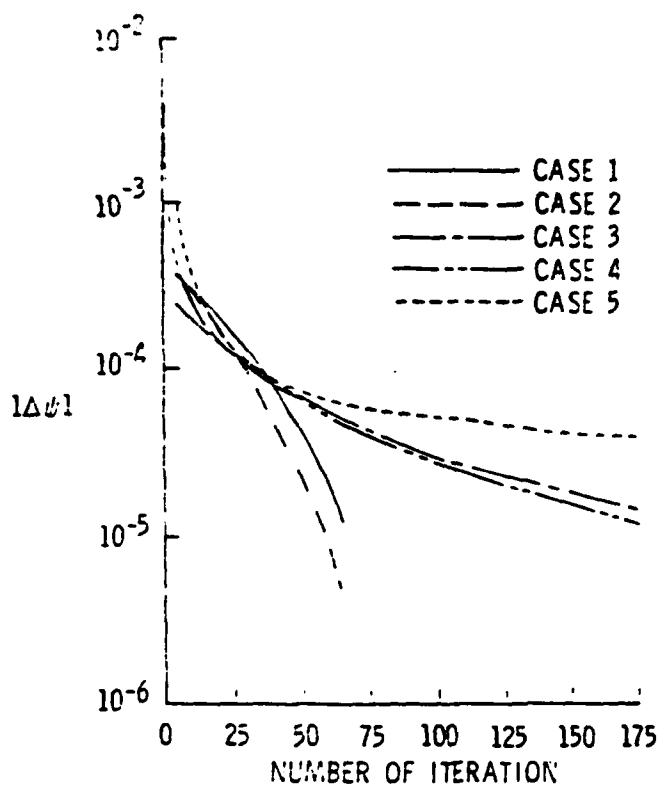


Figure (3) Rates of convergence of present boundary layer calculations

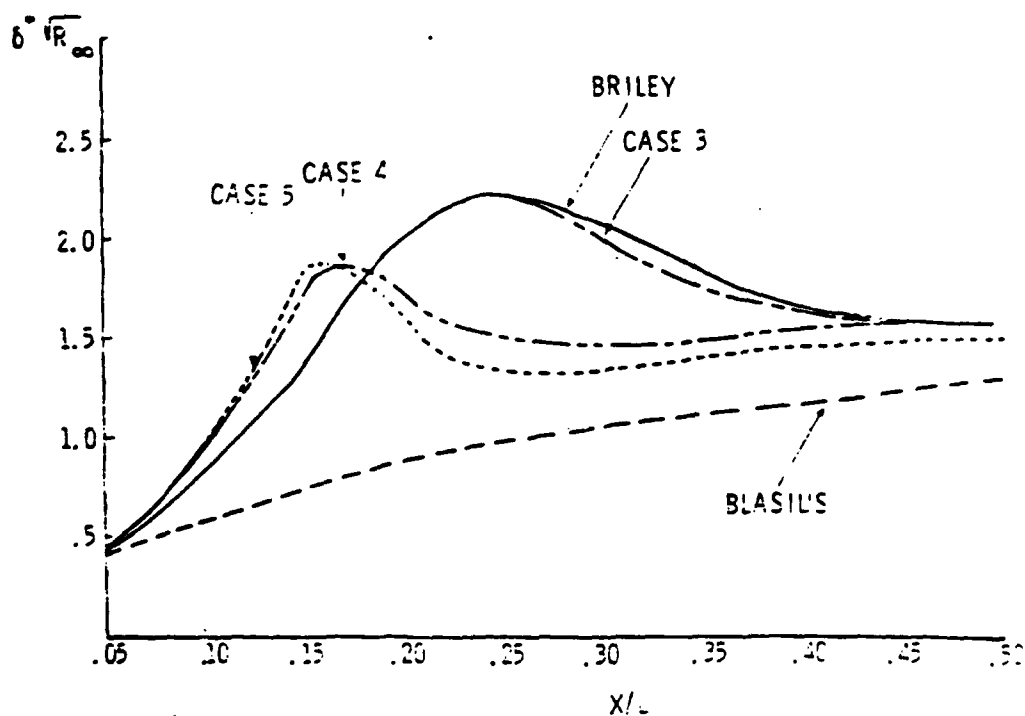


Figure (4) Displacement thickness distribution of present boundary layer calculations

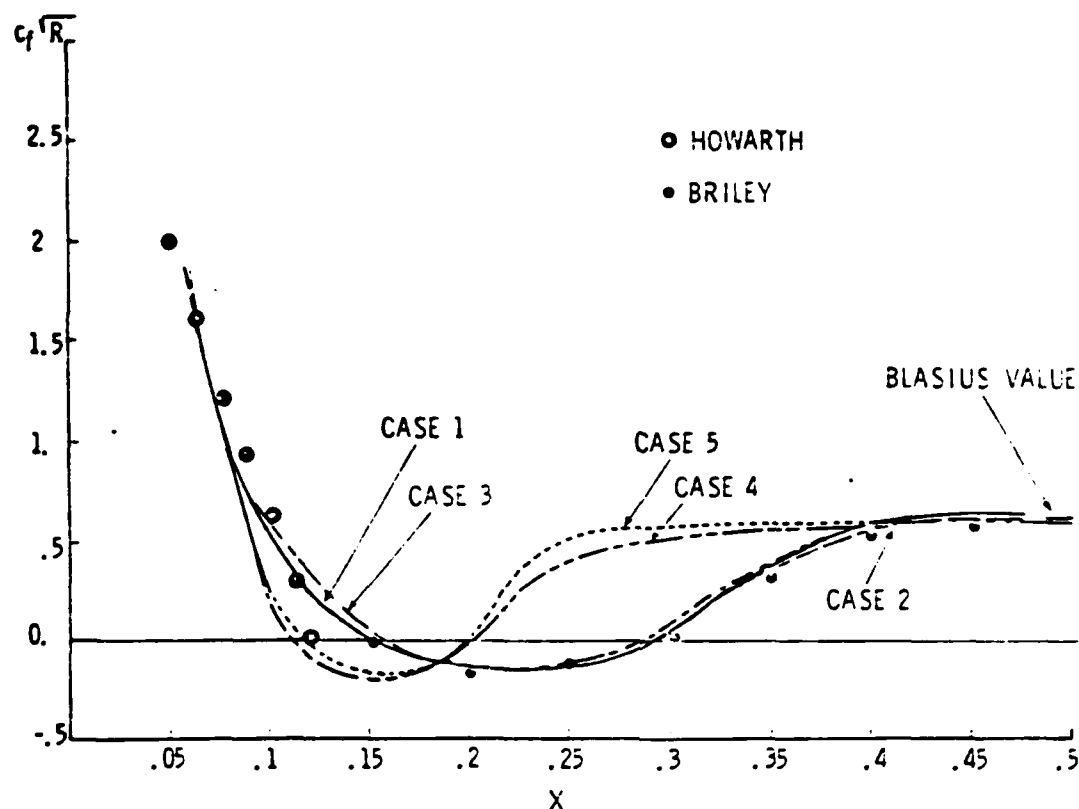


Figure (5) Wall Shear distribution of present boundary layer calculations

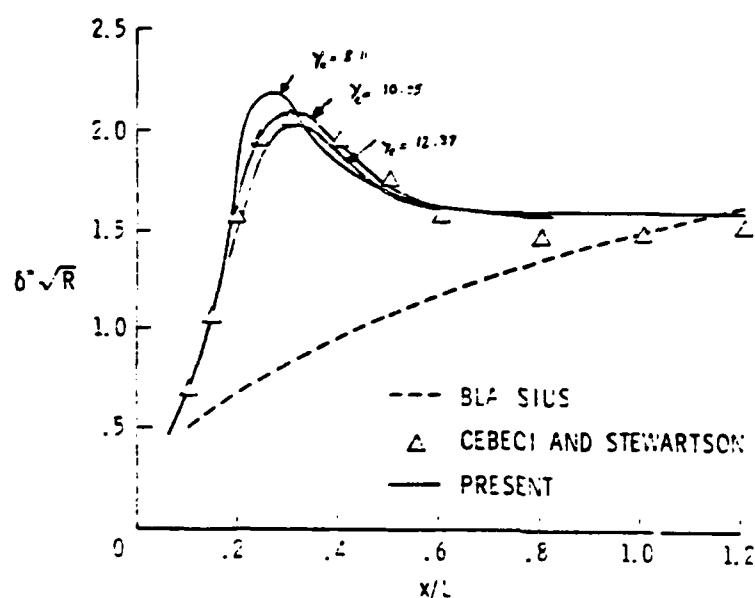


Figure (6) Displacement thickness distribution of present viscous inviscid interactive calculations

END

FILMED

2-84

DTIC